A Full-Band Monte Carlo Transport Simulator for Wide Bandgap Materials in Power Electronics

by

Chi-Yin Cheng

A Dissertation Presented in Partial Fulfillment
of the Requirements for the Degree
Doctor of Philosophy

Approved April 2020 by the
Graduate Supervisory Committee:

Dragica Vasileska, Co-Chair
Stephen M. Goodnick, Co-Chair
Yuji Zhao
Fernando Ponce

ARIZONA STATE UNIVERSITY

May 2020

ABSTRACT

4H-SiC has been widely used in many applications. All of these benefit from its extremely high critical electric field and good electron mobility. For example, 4H-SiC possesses a critical field ten times higher than that of Si, which allows high-voltage blocking layers composed of 4H-SiC to be approximately a tenth the thickness of a comparable Si device. This, in turn, reduces the device on-resistance and power losses while maintaining the same high blocking capability.

Unfortunately, commercial TCAD tools like Sentaurus and Silvaco Atlas are based on the effective mass approximation, while most 4H-SiC devices are not operated under low electric field, so the parabolic-like band approximation does not hold anymore. Hence, to get more accurate and reliable simulation results, full-band analysis is needed. The first step in the development of a full-band device simulator is the calculation of the band structure. In this work, the empirical pseudopotential method (EPM) is adopted. The next task in the sequence is the calculation of the scattering rates. Acoustic, non-polar optical phonon, polar optical phonon and Coulomb scattering are considered. Coulomb scattering is treated in real space using the particle-particle-particle-mesh (P^3M) approach. The third task is coupling the bulk full-band solver with a 3D Poisson equation solver to generate a full-band device simulator.

For proof-of-concept of the methodology adopted here, a 3D resistor is simulated first. From the resistor simulations, the low-field electron mobility dependence upon Coulomb scattering in 4H-SiC devices is extracted. The simulated mobility results agree very well with available experimental data. Next, a 3D VDMOS is simulated. The nature

of the physical processes occurring in both steady-state and transient conditions are revealed for the two generations of 3D VDMOS devices being considered in the study.

Due to its comprehensive nature, the developed tool serves as a basis for future investigation of 4H-SiC power devices.

DEDICATION

Dedicated to my parents,

Cheng-Neng Cheng,

Shu-Yuan Yu,

my brothers,

Chi-Yuan Cheng,

Chi-Wen Cheng,

and my fiancée,

Ning Zhang.

ACKNOWLEDGMENTS

First of all I would like to give my greatest expression to my advisor Dr. Dragica Vasileska for guiding and supporting me through my PhD career. She shows great patience and consideration not just academically but also mentally. She is like a benevolent mom and always encouraging me.

Second, I want to thank Dr. Stephen Goodnick who supports me both academically and financially. Without his aid, I could not finish my PhD career. I could not say more thanks to him.

Third, I would like to thank Dr. Fernando Ponce and Dr. Yuji Zhao for taking time to serve on my committee. In other project, they also provide lots of valuable advises and experience so I can learn more.

Also, I want to thank my roommates, Nai-Yuan Liu, Cheng-Ying Tsai and Wen-Hsi Huang. They are not just good roommates, but also good classmates to discuss with and help me a lot.

At last, I want to say that it is my pleasure to work with my research group members: Yi, Da, Gokul, Robin, Pradyumna, Abdul, Naveen, Izak, Harshad…etc. Without them, I would not have such an excellent journey toward my PhD degree.

TABLE OF CONTENTS

Page

CHAPTER Page

Page

LIST OF TABLES

LIST OF FIGURES

Figure Page

Figure Page

Figure Page

Figure Page

Figure Page

Figure Page

Figure Page

CHAPTER 1

INTRODUCTION

1.1 Foreword

In recent years, the demand for high-power electronic devices has increased because green energy production has become an important factor worldwide. Amongst the candidates for future power devices, wide bandgap materials like silicon carbide (SiC) and gallium nitride (GaN) are the most promising ones. SiC, especially 4H-SiC, is an attractive semiconductor for power electronic device applications due to its excellent intrinsic properties [1][2], specifically because of its high breakdown electric field in combination with high electron mobility. 4H-SiC possesses a critical field ten times higher than that of Si, which allows high-voltage blocking layers composed of 4H-SiC to be approximately a tenth of the thickness of a comparable Si device, thus reducing the device's on-resistance and power losses while maintaining the same high blocking capability [3].

The applications of 4H-SiC-based devices include power transmission, control systems and power supplies. In the power supply applications, it is crucial to reduce the power consumption and increase the conversion efficiency. Switches and rectifiers are extremely important devices in power electronic systems. With SiC devices, the power losses coming from the switches and rectifiers can be significantly reduced because of its low on-resistance and reverse recovery current. Therefore, SiC has become a very good candidate for future power electronic devices and systems.

SiC exhibits promising material characteristics. However, device performance strongly depends on the raw material quality. At present, the high density of crystallographic defects in commercially available SiC wafers limits the size and the yield of SiC devices. Note also that the price of SiC wafers is still high and not yet comparable with the price of Si wafers. This hinders the development of SiC electronics, which is a feasible alternative solution for energy device applications. Modeling and simulation can decrease the cost of fabrication of SiC devices by providing guidance on the optimal device design based on physical principles, thus reducing the time to market and the production cost of these devices. The goal of this thesis is, therefore, to develop a simulation tool that can provide such optimal device design via computer experiments.

1.2 Overview of SiC material

The basic crystal structure of SiC contains one silicon atom that is surrounded by four carbon atoms and one carbon atom that is surrounded by four silicon atoms, as shown in Figure 1.1. The bond length between a carbon atom and a silicon atom is 1.89Å and the bond length between a silicon atom and a silicon atom is 3.08Å. The bandgap of SiC is between that of silicon (1.12eV) and diamond (5.45eV). SiC exists in over 170 polytypes [4]. The most common ones are the cubic 3C, the hexagonal 4H and 6H, and the rhombohedral 15R structures. These polytypes are differentiated by the stacking sequence of the bi-atom layers of the SiC structure, and they have different physical characteristics. Figure 1.2 shows some common polytypes: 3C, 4H and 6H. Amongst them, 3C is the only cubic polytype for SiC.

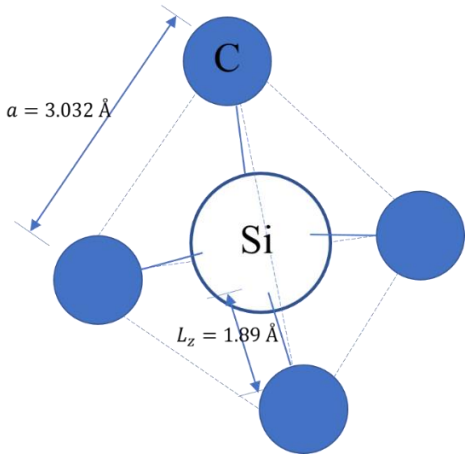

Figure 1.1 Structure of a SiC unit cell.

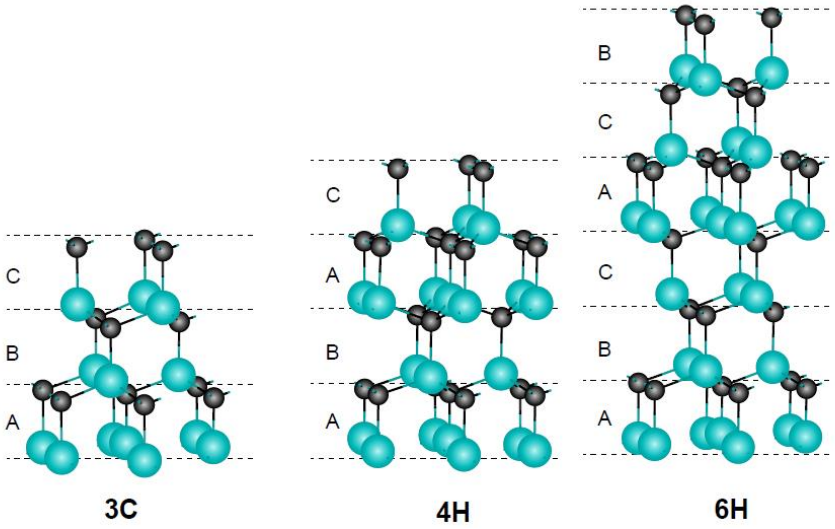

Figure 1.2 Some common polytypes: 3C, 4H and 6H crystal layer stacks [5].

Table 1.1 Properties of SiC in different polytypes.

	Si	3C-SiC	4H-SiC	6H-SiC
Bandgap E_g(eV)	1.12	2.4	3.2	3
Intrinsic Density $n_i(cm^{-3})$	1.5×10^{10}	6.9	8.2×10^{-9}	3×10^{-6}
Thermal Conductivity λ (W/cm-K)	1.5	5	5	5
Critical Electric Field E_c (V/cm)	3×10^5	3×10^6	3×10^6	4×10^6
Electron Mobility μ_n (cm^2/V-s)	1350	1000	950	500
Electron Saturation Velocity V_{sat} (cm/s)	1×10^7	2.5×10^7	2×10^7	2×10^7

Table 1.1 summarizes important material properties. Compared to Si, SiC has (a) wide bandgap, (b) high critical electric field, (c) high thermal conductivity, and (d) high saturation velocity, which make SiC an excellent candidate for high power applications. Among various polytypes of SiC, 4H-SiC is found as the most suitable for high power devices based on the evaluation by the Baliga's figure of merit for power device= $\frac{BV^2}{R_{on,sp}}$ and, therefore, 4H-SiC is chosen as the substrate material in this work.

1.3 Simulation Development of SiC

A good understanding of the transport properties of SiC is needed, and by using simulation, one can investigate its potential at low cost. Accurate simulators have been developed and reported in the literature for studying both material properties and the operation of devices made of those materials. Monte Carlo analysis has been extensively used for the investigation of the transport properties of isotropic materials, such as Si and GaAs. For example, Fischetti and co-workers [6] modeled the microscopic behavior and the impact of electrons of short devices made of Si and GaAs using full-band Monte Carlo simulation. In this work, Coulomb scattering was treated as an additional scattering

mechanism in the Monte Carlo transport kernel. As for SiC, transport models for 2H- and 3C- polytypes were presented earlier than 4H- and 6H-SiC. Tsukioka [7] proposed an ensemble Monte Carlo high-field electron transport model for 3C-SiC. The model was based on the non-parabolic band approximation. Recall that 3C-SiC is the only polytype which is cubic and isotropic so there is only one effective mass value to account for. The first ensemble Monte Carlo simulation of hole transport in bulk 3C-SiC was presented by Belloti *et al.* [8]. Later, Nilsson [9], [10] presented full-band Monte Carlo electron transport calculations for 3C- and 6H-SiC.

In recent years, 4H-SiC has drawn more attention than 3C- and 6H-SiC due to its more favorable material properties. A theoretical model that takes into account the anisotropy in the electron Hall mobility of 4H-SiC was first reported by Iwata [11]. This theoretical model was based on an analytical expression for the conductivity tensor and used the concept of effective masses. However, the model failed to describe the high field transport properties of the 4H-SiC. To address this shortcoming, Joshi and coworkers [12] applied effective masses for electrons in 4H-SiC that were derived from experimental data, in their Monte Carlo transport model to explore the temperature and field-dependent transport properties of this material system. Yet, the doping levels used in these calculations were low, hence, the doping dependence of the mobility remained unclear. Later on, Nilsson and his coworkers [13] used a two-band multiple-minima model for the Monte Carlo calculation of transport properties of 4H-SiC. The analytical band structure used in this work was better and included the anisotropy of the energy bands. In 2003, Hjelm [14] made the first full-band ensemble Monte Carlo simulator for 4H-SiC to study

the high-field transport properties of this material system. For impurity scattering modeling , these authors adopted Ridley's [15] analytical model and included this scattering mechanism in the k-space portion of the Monte Carlo transport kernel. Note that this approach is less accurate than the real-space molecular dynamics treatment of the Coulomb interaction used in the present work. Later, Kovalchuk *et al*. [16] reported that the use of the Conwell-Weisskopf model instead of the Brooks-Herring model for impurity/Coulomb scattering gives better agreement with the experimental data.

Other approaches to model the electron transport in 4H-SiC were also investigated. For example, Akturk [17] and Woźny [18] utilized numerically calculated conduction and valence band density-of-states (DOS) obtained from density functional theory (DFT) in their transport models. This approach is faster and easier when compared to a full-band Monte Carlo simulation, but also not that precise. The matrix elements for most phonon scattering processes depend upon the momentum transfer in the scattering process and the total scattering rate is not directly proportional to the final density of states function. For Coulomb scattering, both groups adopted either Brooks-Herring or Conwell Weisskopf models that fail for heavily doped materials.

The real-space molecular dynamics treatment of the Coulomb interaction includes simultaneously electron-electron and electron-impurity Coulomb scattering, which is dynamically screened, and naturally accounts for multiple scattering events from the same charged center. Besides this, at high doping densities it treats the simultaneous scattering from multiple impurity centers exactly to all orders within the classical approximation. It

is also important to note that the incorporation of the electron-electron interactions is very important in high power devices due to the very high carrier densities. The incorporation of the electron-electron interactions as a scattering process in the k-space portion of the Monte Carlo transport kernel requires calculation of the distribution function (see, e.g. Fischetti *et al.* [19]), which is very time consuming. Also, treatment of the dynamical screening of the Coulomb interaction is very difficult using the k-space approach [20]. The real-space molecular dynamics approach reduces significantly the shortcomings of the k-space approach. Therefore, a preferable approach by Gross *et al.* [21] is adopted in this work.

Note that modern commercial Technology for Computer-Aided Design (TCAD) tools like Synopsys Sentaurus [22], Silvaco Atlas and Silvaco VictoryDevice [23] use the drift-diffusion and hydrodynamic models for carrier transport. The drift-diffusion model is based on the relaxation time approximation which is simple but fails for small devices and high-energy simulations. The hydrodynamic model can calculate carrier heating but the problem there is the proper choice of the energy relaxation times that are both material and device dependent quantities. Nonetheless, both methods are inadequate for ultra-small devices operated under high electric fields. Hence, the Monte Carlo method, that in the long-time limit solves the Boltzmann transport equation, is a method of choice when drift-diffusion and hydrodynamic models fail.

Since most of the 4H-SiC devices are operated under high electric fields, the non-parabolic band approximation does not hold and the effective mass model for the

transport calculation fails. In this research work, the real space treatment of Coulomb scattering via the molecular dynamics approach, which as noted earlier, includes the fullelectron-electron and electron-ion interactions, is coupled with a full-band ensemble Monte Carlo simulation framework and used in the calculation of the low- and high-field anisotropic electron transport properties of 4H-SiC. It is then extended and used in the simulation of a vertical double-diffused metal-oxide-semiconductor field-effect transistor structure (VDMOS).

This thesis is organized as follows. CHAPTER 2 describes the empirical pseudopotential method (EPM). CHAPTER 3 discusses the phonon scattering mechanisms used and the scattering rates calculation. CHAPTER 4 introduces the particle-particle-particle-mesh (P^3M) method and how it is applied into the real-space treatment of the Coulomb scattering. All the above is used in the development of the in-house full-band Monte Carlo (FBEMC) device simulator. To validate the FBEMC device simulator, a 3D resistor is simulated first, and the results of these simulations are discussed in CHAPTER 5 . CHAPTER 6 discusses the simulation results of a widely used power electronic device, the vertical double-diffused metal-oxide-semiconductor field-effect transistor (VDMOS), by the means of the FBEMC device simulator. Lastly, CHAPTER 7 summarizes this research work and proposes ways of extending its capability and potential for future research.

CHAPTER 2

EMPIRICAL PSEUDOPOTENTIAL METHOD

2.1 Methods of Calculating Band Structure

The calculation of the band structure is the first and the critical step in the development of a full-band Monte Carlo transport simulator. Various properties, like density of states and mobility, can be calculated with the electronic properties derived from the band structure. There are several models one can use to obtain the band structure, which can be separated into: (a) first principle, and (b) semi-empirical approaches. First principle calculations are necessary for the calculation of the band structure of novel materials. One example is the Density Functional Theory (DFT). DFT calculates the properties of materials by effectively solving the many-body Schrödinger equation, and it does not need the use of empirical fitting parameters. This method is commonly used at the atomic level. Although the ability of modern hardware has improved significantly in recent years, the DFT calculations can only be done on systems comprising of less than thousands of atoms. Hence, for a device which features large geometry, the first principle method is still not a possible option.

The second category is the semi-empirical methods. To reproduce the known band-structure of materials, semi-empirical methods calibrated to first-principles band structure are used. These include the empirical pseudopotential method (EPM) [24], [25], the full-zone k.p method [26], [27] and the semi-empirical tight-binding (TB) method [28], [29]. They use empirical parameters to fit experimental data and/or first principle calculations.

The EPM provides an effective way to get the band structure since one can adjust parameters to fit measurements. Although the whole band structure is difficult to be mapped experimentally, one can measure the most obvious parameter, the optical band gaps, from the experiments. One may find the closest set of parameters to fit the band gaps by varying them. The problem that occurs is finding the correct parameters set to get a satisfying fit of the experimental results. This is especially challenging for materials with a large unit cell like SiC, since many parameters are needed for the calculation. To overcome this problem, the most common approach is to use semi-empirical method that uses the atomic pseudopotentials of Si and C and assumes that they can be applied to the SiC material system. Junginger and Haeringen were the first ones to use this approach in 1970 to explore the properties of SiC [30]. In 2001, Pennington and Goldsman modified the pseudopotentials of Si and C to get the EPM form factors considering the nonlocal screening effects [31]. Zubkova studied the temperature dependence of the band structure [32]. Ng [33] abandoned the attempts to derive the form factors from atomic potentials but treated them as completely adjustable parameters and applied genetic algorithms to fit the optical gaps. The genetic algorithm is a powerful tool that can easily be applied on any material of interest. The work of Ng is used here in the development of the band structure calculation module.

2.2 Introduction to the Empirical Pseudopotential Method

The main advantage of using pseudopotentials is that only valence electrons, which are weakly bounded and nearly free, should be considered. Since the core electrons are tightly bound to their nuclei and localized around their sites, these electrons do not

contribute to bonding or conduction. The pseudopotential theory assumes that the total wave function can be divided into an oscillatory part and a smooth part, the so-called pseudo wave function. The oscillatory part of the wavefunction needs a large number of plane waves to represent it properly. To avoid this complication, the true potential of the ions is replaced by a potential valid for the valence electrons, $V(r)$, which is proportional inversely to the radius r, just like the Coulomb potential in free space (see Figure 2.1). This pseudopotential allows one to approximate the valence electron wave functions with only a small number of plane waves, which makes the calculation easier.

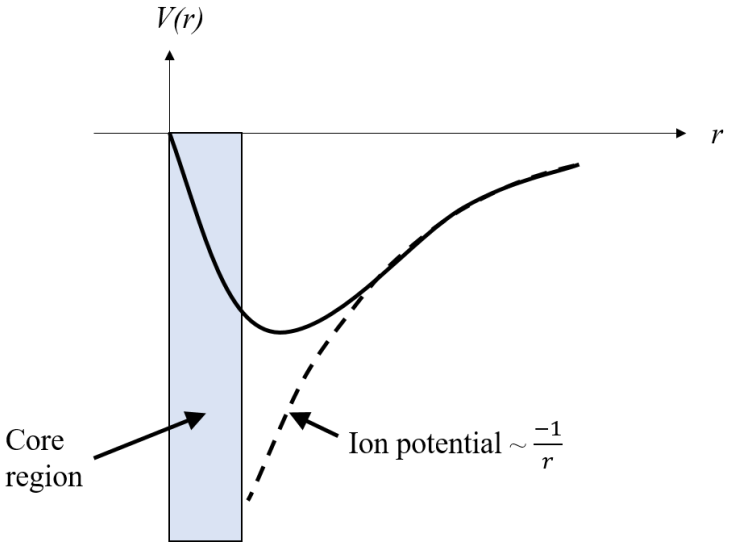

Figure 2.1 Pseudopotential in real space.

The one-electron Schrödinger equation is solved next and after some manipulations it leads to the pseudo-wave equation

$$\left(\frac{p^2}{2m} + V(r)\right)\phi_k(r) = E_k\phi_k(r) \tag{2.1}$$

where $\phi_k(r)$ represents the pseudo wave function, $V(r)$ is the pseudopotential and E_k is

the eigenvalue. At the meantime, $\phi_k(r)$ can be expanded into a summation of plane waves by

$$\phi_k(r) = \frac{e^{ik\cdot r}}{\sqrt{\Omega}} \sum_{\boldsymbol{G}} \boldsymbol{\alpha_G} e^{i\boldsymbol{G}\cdot r} \tag{2.2}$$

Here, α_G is the expansion coefficient, $\Omega = \boldsymbol{a_1} \cdot \boldsymbol{a_2} \times \boldsymbol{a_3}$ is the volume of the unit cell and $\boldsymbol{G}$ is a general reciprocal lattice vector which is given as

$$\boldsymbol{G} = n_1\boldsymbol{b}_1 + n_2\boldsymbol{b}_2 + n_3\boldsymbol{b}_3 \tag{2.3}$$

Here, $\boldsymbol{b}_i$ are the reciprocal primitive vectors and n_i are integers. In addition, $V(r)$ can be expanded as

$$V(r) = \sum_{\boldsymbol{G'-G}} V(\boldsymbol{G'} - \boldsymbol{G}) e^{i(\boldsymbol{G'-G})\cdot r} \tag{2.4}$$

By inserting Eq. (2.2) and Eq. (2.4) into Eq. (2.1) one arrives at

$$det \left| \left[\frac{\hbar^2 (k + \boldsymbol{G})^2}{2m} - E_{\boldsymbol{k}} \right] \delta_{\boldsymbol{G},\boldsymbol{G'}} + V_{\boldsymbol{G},\boldsymbol{G'}} \right| = 0 \tag{2.5}$$

One finds that the first terms in the determinant are the diagonal elements of the matrix *H* and the second term represents the off-diagonal elements of *H*. The off-diagonal elements $V_{\boldsymbol{G},\boldsymbol{G'}}$ are expressed as

$$V_{\boldsymbol{G},\boldsymbol{G'}} = \frac{1}{\Omega} \int V(\boldsymbol{r}) e^{i(\boldsymbol{G'-G})\cdot r} d\boldsymbol{r} \tag{2.6}$$

and are called form factors of pseudopotential. In this description we assume that there is only one atom in the unit cell. If there is more than one atom, for example if we have two atoms, the expressions have to be modified accordingly. Then Eq. (2.4) becomes

$$V(\boldsymbol{r}) = \sum_{\boldsymbol{G'-G}} \left(V_1(\boldsymbol{G'} - \boldsymbol{G}) e^{i(\boldsymbol{G'-G})\cdot\left(r + \frac{\boldsymbol{r_b}}{2}\right)} + V_2(\boldsymbol{G'} - \boldsymbol{G}) e^{i(\boldsymbol{G'-G})\cdot\left(r - \frac{\boldsymbol{r_b}}{2}\right)} \right) \tag{2.7}$$

$$= V_{10}(\boldsymbol{r})e^{i(\boldsymbol{G'}-\boldsymbol{G})\cdot\left(\frac{\boldsymbol{r_b}}{\boldsymbol{2}}\right)} + V_{20}(\boldsymbol{r})e^{i(\boldsymbol{G'}-\boldsymbol{G})\cdot\left(-\frac{\boldsymbol{r_b}}{\boldsymbol{2}}\right)} \tag{2.8}$$

Here V_1 and V_2 represent the atomic-like potentials centered at $\pm\frac{r_b}{2}$. One can extend Eq. (2.4) to any number of atoms case

$$V(r) = \sum_{\boldsymbol{G}} S_{\boldsymbol{G}} V_{\boldsymbol{G}} e^{i\boldsymbol{G}\cdot r} \tag{2.9}$$

where V_G is the pseudo potential form factor and S_G is called the structure factor which is defined as

$$S_G = \frac{1}{N}\sum_{j}^{N} e^{-iG\cdot r_j} \tag{2.10}$$

where r_j is the relative position of the respective atom in the primitive unit cell and N denotes the number of atoms in the primitive unit cell.

2.3 Structures of SiC

SiC can be categorized into two groups, α-SiC or β-SiC. α-SiC features hexagonal structure and usually forms at temperatures greater than 1700℃. On the other hand, β-SiC has zinc blende structure and forms at temperatures below 1700℃. Furthermore, the 3C polytype is the only one belonging to β-SiC. The crystal structures of α-SiC are composed of hexagonal close-packed layers. As shown in

Figure 2.2, there are three possible lattice locations for the crystal layers. Because the crystal tends to be stable for lower energy, if we set the first layer to be A position, then there are only two possible locations left, B and C, for the layer on the top of A. By piling up the layers in different sequences, various crystal structures can be obtained. Sequence in ABAB is a hexagonal close-packed crystal (hcp); in ABCABC it becomes a

face-centered cubic crystal (fcc), and there are infinite possible structures in any further combinations. 4H-SiC, which is the topic in this thesis, features the stacking sequence in ABCBABCB if we consider one Si atom and one C atom forming the basis. The relative coordinates of atoms are shown in Figure 2.3. Figure 2.3(a) depicts the positions along c-axis and Figure 2.3(b) illustrates the positions for the A, B, and C planes.

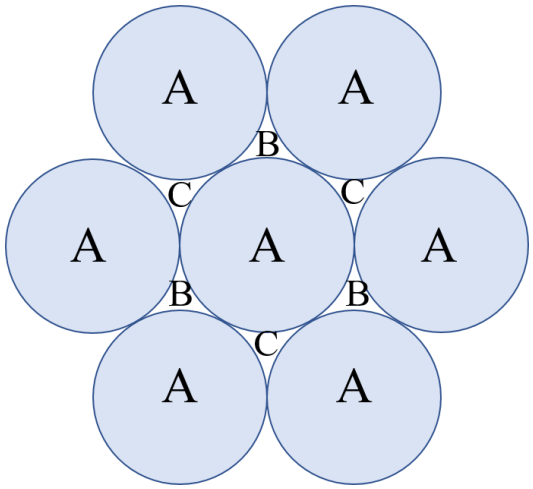

Figure 2.2 Hexagonal close-packed layer which shows three possible lattice locations.

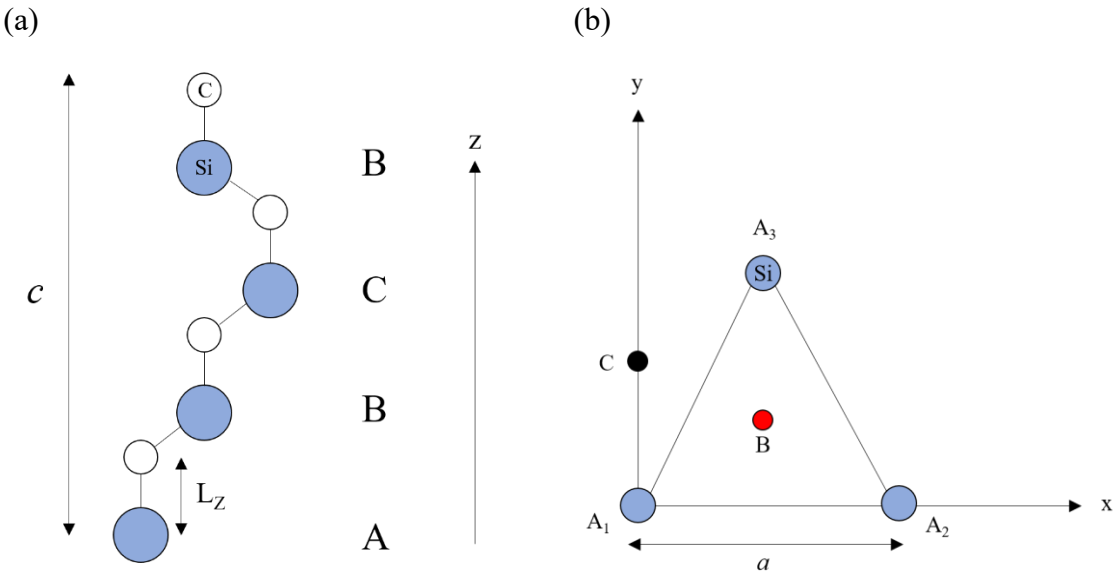

Figure 2.3 Cross-sectional views of 4H-SiC structure. (a) Stacking sequence of 4H-SiC. (b) Coordinates for A, B and C layer lattice locations projected on the *xy*-plane.

2.4 EPM Implementation for 4H-SiC

The real space translation vectors of 4H-SiC can be easily calculated from Figure 2.3. If one takes A_1 as the origin, then A_2, A_3 will be $a\hat{\boldsymbol{x}}$ and $\frac{a}{2}\hat{\boldsymbol{x}} + \frac{a\sqrt{3}}{2}\hat{\boldsymbol{y}}$, respectively. In addition, since the layers repeated every four layers, the translating vector is in the z direction with a lattice constant c. The three translation vectors are

$$\boldsymbol{a_1} = a\hat{\boldsymbol{x}}$$

$$\boldsymbol{a_2} = \frac{a}{2}\hat{\boldsymbol{x}} + \frac{a\sqrt{3}}{2}\hat{\boldsymbol{y}}$$

$$\boldsymbol{a_3} = c\hat{\boldsymbol{z}} \tag{2.11}$$

The corresponding reciprocal lattice vectors are calculated as

$$\boldsymbol{b}_1 = 2\pi \frac{\boldsymbol{a}_2 \times \boldsymbol{a}_3}{\boldsymbol{a}_1 \cdot \boldsymbol{a}_2 \times \boldsymbol{a}_3} = \frac{2\pi}{a}\hat{\boldsymbol{x}} - \frac{2\pi}{a\sqrt{3}}\hat{\boldsymbol{y}}$$

$$\boldsymbol{b}_2 = 2\pi \frac{\boldsymbol{a}_3 \times \boldsymbol{a}_1}{\boldsymbol{a}_1 \cdot \boldsymbol{a}_2 \times \boldsymbol{a}_3} = \frac{4\pi}{a\sqrt{3}}\hat{\boldsymbol{y}}$$

$$\boldsymbol{b}_3 = 2\pi \frac{\boldsymbol{a}_1 \times \boldsymbol{a}_2}{\boldsymbol{a}_1 \cdot \boldsymbol{a}_2 \times \boldsymbol{a}_3} = \frac{2\pi}{c}\hat{\boldsymbol{z}} \tag{2.12}$$

Since 4H-SiC has the ABCB stacking sequence, one needs to consider B and C locations as well. From Figure 2.3 one can find the coordinate of the B in real space is $\frac{a}{2}\hat{\boldsymbol{x}} + \frac{a}{2\sqrt{3}}\hat{\boldsymbol{y}} + \frac{c}{4}\hat{\boldsymbol{z}}$ and the coordinate of C is $\frac{a}{\sqrt{3}}\hat{\boldsymbol{y}} + \frac{c}{2}\hat{\boldsymbol{z}}$. For simplification, if one defines

$$\boldsymbol{v} = \frac{c}{4}\hat{\boldsymbol{z}}$$

$$\boldsymbol{h}_B = \frac{a}{2}\hat{\boldsymbol{x}} + \frac{a}{2\sqrt{3}}\hat{\boldsymbol{y}}$$

$$\boldsymbol{h}_C = \frac{a}{\sqrt{3}}\hat{\boldsymbol{y}} \tag{2.13}$$

then one can express the location of the first B as $\boldsymbol{h_B}+\boldsymbol{v}$, second B as $\boldsymbol{h_B}+3\boldsymbol{v}$ and the location of C as $\boldsymbol{h_C}+2\boldsymbol{v}$. Besides, we set $\boldsymbol{s} = \frac{L_Z}{2}\hat{\boldsymbol{z}}$. Since each lattice point comprises Si and C atom with a bonding length L_Z as shown in Figure 2.3(a), by combining Eq. (2.8), Eq. (2.9) and Eq. (2.10), the off-diagonal elements of the Hamiltonian matrix *H* become

$$V_{\boldsymbol{G},\boldsymbol{G}'} = \frac{1}{\Omega}\int S_G \cdot \left(V_{10}(\boldsymbol{r})e^{i(\boldsymbol{G}'-\boldsymbol{G})\cdot\boldsymbol{s}} + V_{20}(\boldsymbol{r})e^{-i(\boldsymbol{G}'-\boldsymbol{G})\cdot\boldsymbol{s}}\right)e^{i(\boldsymbol{G}'-\boldsymbol{G})\cdot\boldsymbol{r}}$$

$$= S_G \times \frac{1}{\Omega}\int \left(V_{10}(\boldsymbol{r})e^{i(\boldsymbol{G}'-\boldsymbol{G})\cdot\boldsymbol{s}} + V_{20}(\boldsymbol{r})e^{-i(\boldsymbol{G}'-\boldsymbol{G})\cdot\boldsymbol{s}}\right)e^{i(\boldsymbol{G}'-\boldsymbol{G})\cdot\boldsymbol{r}}\, d\boldsymbol{r}$$

$$= S_G \times \frac{1}{\Omega}\int \Big[V_{10}(\boldsymbol{r})\big(\cos\big((\boldsymbol{G}'-\boldsymbol{G})\cdot\boldsymbol{s}\big) + i\sin\big((\boldsymbol{G}'-\boldsymbol{G})\cdot\boldsymbol{s}\big)\big)$$

$$+V_{20}(\boldsymbol{r})\big(\cos\big((\boldsymbol{G}'-\boldsymbol{G})\cdot\boldsymbol{s}\big) - i\sin\big((\boldsymbol{G}'-\boldsymbol{G})\cdot\boldsymbol{s}\big)\big)\Big]\cdot e^{i(\boldsymbol{G}'-\boldsymbol{G})\cdot\boldsymbol{r}}\, d\boldsymbol{r}$$

$$= S_G \times \frac{1}{\Omega} \int \left[(V_{10}(\boldsymbol{r}) + V_{20}(\boldsymbol{r})) \cos\left((\boldsymbol{G'} - \boldsymbol{G}) \cdot \boldsymbol{s}\right) \right.$$

$$\left. + i(V_{10}(\boldsymbol{r}) - V_{20}(\boldsymbol{r})) \sin\left((\boldsymbol{G'} - \boldsymbol{G}) \cdot \boldsymbol{s}\right) \right] e^{i(\boldsymbol{G'} - \boldsymbol{G}) \cdot \boldsymbol{r}} \, d\boldsymbol{r} \tag{2.14}$$

For simplification, one defines

$$V_S = \frac{1}{\Omega} \int \left(V_{10}(\boldsymbol{r}) + V_{20}(\boldsymbol{r})\right) e^{i(\boldsymbol{G'} - \boldsymbol{G}) \cdot \boldsymbol{r}} \, d\boldsymbol{r}$$

$$V_A = \frac{1}{\Omega} \int \left(V_{10}(\boldsymbol{r}) - V_{20}(\boldsymbol{r})\right) e^{i(\boldsymbol{G'} - \boldsymbol{G}) \cdot \boldsymbol{r}} \, d\boldsymbol{r} \tag{2.15}$$

then Eq. (2.14) becomes

$$V_{\boldsymbol{G},\boldsymbol{G'}} = S_G \times \left[V_S \cos\left((\boldsymbol{G'} - \boldsymbol{G}) \cdot \boldsymbol{s}\right) + i V_A \sin\left((\boldsymbol{G'} - \boldsymbol{G}) \cdot \boldsymbol{s}\right) \right] \tag{2.16}$$

and expand the contribution of ABCB layers, the modified S_G in Eq.(2.16), one obtains

$$S_G = \left(\sum_{j=1}^{4} e^{-i(\boldsymbol{G'} - \boldsymbol{G}) \cdot \boldsymbol{r}_j} \right)$$

$$= \left[1 + e^{-i(\boldsymbol{G'} - \boldsymbol{G}) \cdot (\boldsymbol{h}_B + \boldsymbol{v})} + e^{-i(\boldsymbol{G'} - \boldsymbol{G}) \cdot (\boldsymbol{h}_C + 2\boldsymbol{v})} + e^{-i(\boldsymbol{G'} - \boldsymbol{G}) \cdot (\boldsymbol{h}_B + 3\boldsymbol{v})} \right] \tag{2.17}$$

When all matrix elements are calculated, the next step is to solve the eigenvalue equation $H\phi = E\phi$. The EPM alternates the V_S and V_A terms to fit the experimental electronic band gap. To make the fitting much faster and much more precise, Ng applied genetic algorithm to find the best parameter set [33]. The values of V_S and V_A to re-build the band structure are listed in Table 2.1. The lattice constants $a = 3.032$ Å and $c = 9.928$ Å, and bond length $L_z = 1.866$ Å are used. In addition, 205 eV cut-off energy is adopted that requires use of 527 plane waves. The first Brillouin zone in reciprocal space of 4H-SiC is hexagonal and the high symmetry points are shown in Figure 2.4 [34]. The solution of the eigenvalue problem leads to a band structure shown in Figure 2.5. The indirect band gap

is 3.2568 eV which is between Γ point and M point. It is quite close to the commonly adopted value of 3.26 eV.

For the full-band Monte Carlo (FBEMC) calculations, one needs the full band structure, not just the values of the band structure along high symmetry points. Hence, the irreducible 1st Brillouin zone is discretized into 21000 $\boldsymbol{k}$-points and all 527 energy levels are calculated. The energy levels of the first 4 bands are shown in Figure 2.6. In addition, the $\boldsymbol{\nabla_k E}$ distribution is also needed. The gradient, $\nabla_k E(\boldsymbol{k_c}, \boldsymbol{n})$ by definition is calculated using

$$\nabla_k E(\boldsymbol{k_c}, \boldsymbol{n}) = \frac{\partial E(\boldsymbol{k_c}, \boldsymbol{n})}{\partial k_x} e_x + \frac{\partial E(\boldsymbol{k_c}, \boldsymbol{n})}{\partial k_y} e_y + \frac{\partial E(\boldsymbol{k_c}, \boldsymbol{n})}{\partial k_z} e_z. \tag{2.18}$$

$\boldsymbol{n}$ indicates $\boldsymbol{n}$th band's energy. e_x, e_y, e_z are the unit vectors in the k_x, k_y, k_z direction, respectively. To calculate the terms given in Eq. (3.18), the central difference scheme is used, according to which

$$\frac{\partial E(\boldsymbol{k_c}, \boldsymbol{n})}{\partial k_m} \approx \frac{1}{2\Delta} [E(\boldsymbol{k_c} + \Delta e_m, \boldsymbol{n}) - E(\boldsymbol{k_c} - \Delta e_m, \boldsymbol{n})] \tag{2.19}$$

where m=x, y, z and Δ is the difference parameter, which is set to a value 0.001. Both ***E-k*** and $\boldsymbol{\nabla_k E}$ distributions are then stored and ready for use.

Table 2.1 EPM form factors for 4H-SiC in Rydbergs, where k_x is scaled by $a/2\pi$, k_y is scaled by $a\sqrt{3}/2\pi$, and k_z is scaled by $c/2\pi$ [33].

G (k_x, k_y, k_z)	V_S	V_A	G (k_x, k_y, k_z)	V_S	V_A
(0,2,0) (1,1,0)	-0.186		(0,2,5) (1,1,5)	-0.034	-0.058
(0,2,1) (1,1,1)	-0.140	-0.196	(2,0,0) (1,3,0)	0.085	
(0,0,4)	0.103	-0.031	(0,2,6) (1,1,6)	0.041	-0.124
(0,2,2) (1,1,2)	-0.111	-0.034	(0,4,0) (2,2,0)	0.004	
(0,2,3) (1,1,3)	-0.022	-0.007	(0,4,1) (2,2,1)	0.007	0.003
(0,2,4) (1,1,4)	-0.107	-0.094			

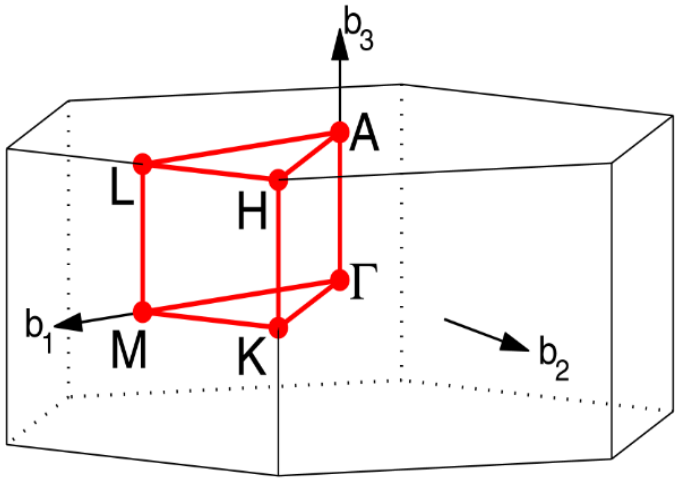

Figure 2.4 First Brillouin zone of a hexagonal close-packed crystal structure. Also shown here are the high symmetry points [34].

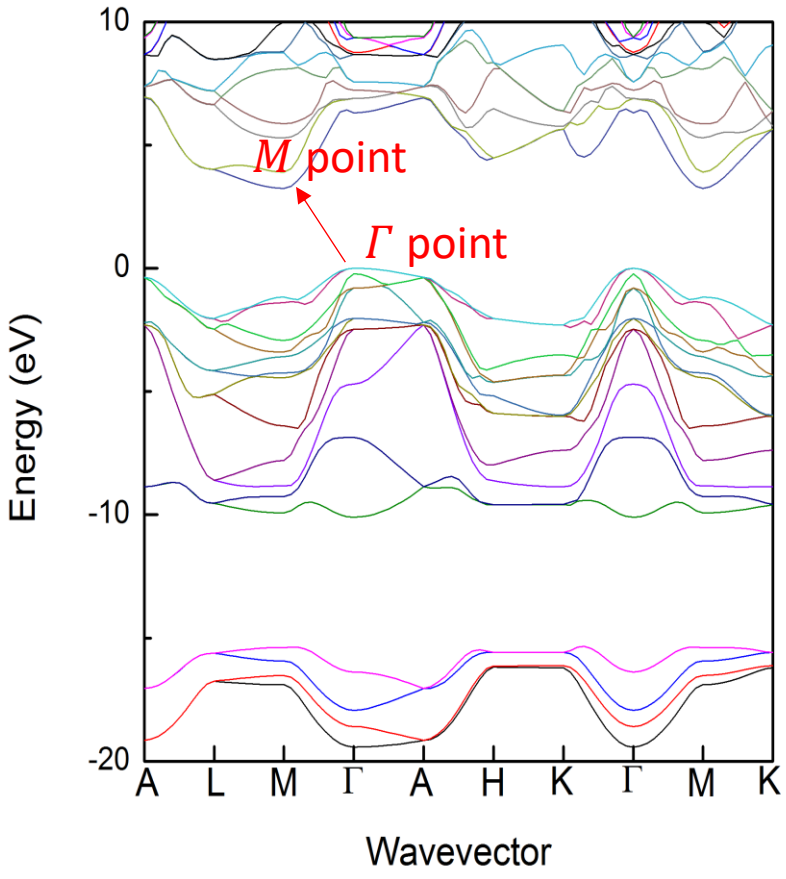

Figure 2.5 Energy band structure of 4H-SiC calculated by using the EPM with parameter sets obtained by G. Ng *et al.* [33].

(a)

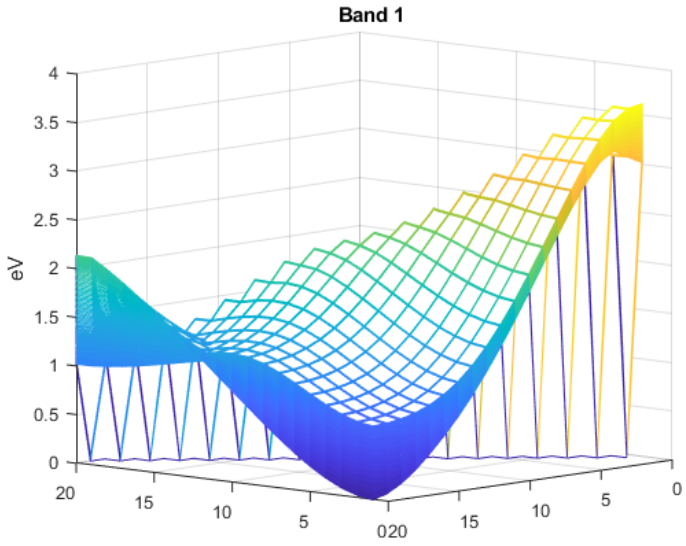
Band 1
eV
4
3.5
3
2.5
2
1.5
1
0.5
0
20
15
10
5
020
15
10
5
0

(b)

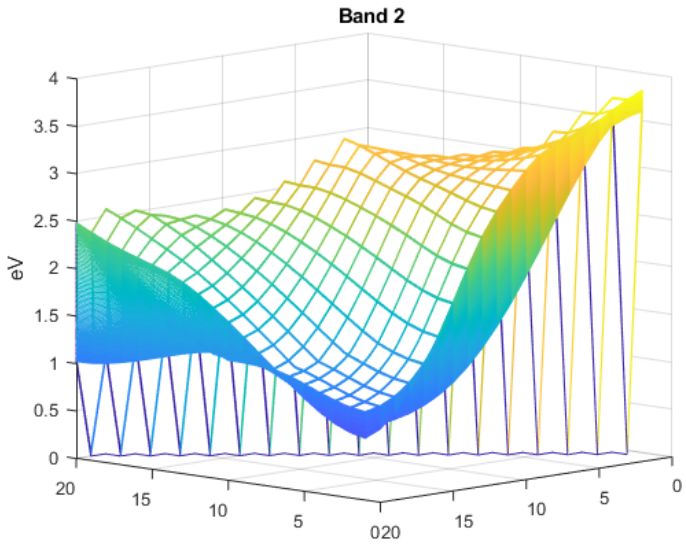
Band 2
eV
4
3.5
3
2.5
2
1.5
1
0.5
0
20
15
10
5
020
15
10
5
0

(c)

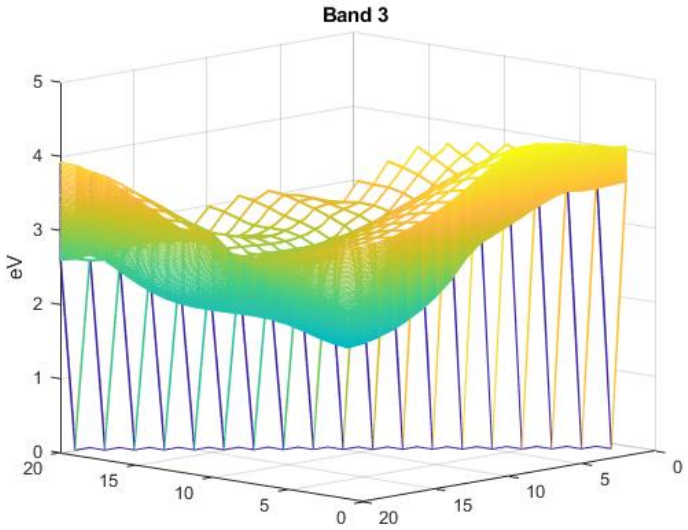

(d)

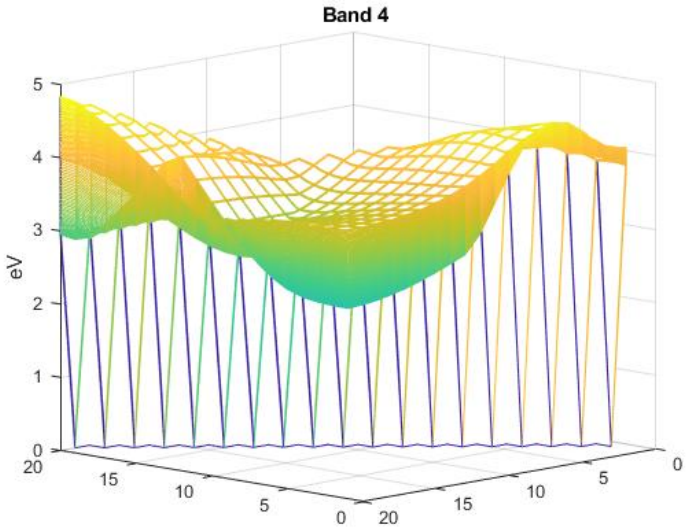

Figure 2.6 First four band energies in irreducible 1st Brillouin zone.

(a) Band 1, (b) Band 2, (c) Band 3, (d) Band 4.

CHAPTER 3

SCATTERING MECHANISMS

The next step in the development of a full-band Monte Carlo device simulator, that in the long-time limit solves the Boltzmann Transport Equation (BTE), is the choice of the scattering mechanisms. The dominant scattering mechanisms in 4H-SiC material system are acoustic phonon, non-polar optical phonon, polar optical phonon and impurity scattering. Hjelm [14] presented a set of parameters describing the phonon scattering mechanisms in 4H-SiC. The first three mechanisms were pre-calculated with the band structure obtained from the last chapter and their values were saved to reduce run-time execution. As for impurity scattering, for the typical doping level in 4H-SiC applications, both the Brooks-Herring and Conwell-Weiskopf models are not quite valid because in a particle-based device simulation framework one solves the Poisson equation, thus accounting for the long range and some part of the short-range interaction depending upon the mesh size. To avoid such complication of double-counting the Coulomb force, both electron-electron and electron-ion interactions are calculated in real space using particle-particle-particle-mesh (P^3M) method that is discussed in the next chapter.

3.1 Acoustic Phonon Scattering

The probability of acoustic phonon scattering from $\boldsymbol{k}$ to $\boldsymbol{k'}$ in reciprocal space is given as

$$P_A(\boldsymbol{k},\boldsymbol{k}') = \frac{\pi}{\rho V \omega_q}\begin{bmatrix} N_q \\ N_q+1 \end{bmatrix} I^2_{j,j'}(\boldsymbol{k},\boldsymbol{k}')\boldsymbol{q}^{\boldsymbol{2}}(\boldsymbol{k},\boldsymbol{k}')D_A^2\delta\big(E(\boldsymbol{k}')-E(\boldsymbol{k})\mp\hbar\omega_q\big) \quad (3.1)$$

The upper and lower part indicate absorption and emission, respectively. ρ is the density of the crystal, V the normalization volume, ω_q the phonon angular frequency and N_q the number of phonons which is expressed as

$$N_q = \frac{1}{e^{\frac{\hbar\omega_q}{k_B T}} - 1} \,. \tag{3.2}$$

$\boldsymbol{q}(\boldsymbol{k}, \boldsymbol{k}')$ is the phonon wave vector and D_A is the acoustic deformation potential. In Eq. (3.1) and (3.2) the phonon energy has the form

$$\hbar\omega_q = \begin{cases} \hbar\omega_{max}\left[c_3\left(\frac{|\boldsymbol{q}(\boldsymbol{k},\boldsymbol{k}')|}{k_{max}}\right)^3 + c_2\left(\frac{|\boldsymbol{q}(\boldsymbol{k},\boldsymbol{k}')|}{k_{max}}\right)^2 + c_1\left(\frac{|\boldsymbol{q}(\boldsymbol{k},\boldsymbol{k}')|}{k_{max}}\right)\right], |\boldsymbol{q}(\boldsymbol{k},\boldsymbol{k}')| < k_{max} \\ \hbar\omega_{max}, \quad |\boldsymbol{q}(\boldsymbol{k},\boldsymbol{k}')| \geq k_{max}. \end{cases} \tag{3.3}$$

Here $\hbar\omega_{max} = 0.0672$ eV, $k_{max} = 0.577350\ \frac{2\pi}{a_{SiC}}$, $c_1 = 1.6129$, $c_2 = -0.172291$, and $c_3 = -0.441035$. $I_{j,j'}(\boldsymbol{k}, \boldsymbol{k}')$ in Eq. (3.1) is the overlap integral over the unit cell defined as

$$I_{j,j'}(\boldsymbol{k}, \boldsymbol{k}') = \int_{cell} u^*_{j',k'}(r) u_{j,k}(r) d^3r. \tag{3.4}$$

$u_{j,k}(r)$ is the periodic part of the Bloch function from initial state $\boldsymbol{k}$ at *j*th band and $u_{j',k'}(r)$ is at final state $\boldsymbol{k'}$ at *j'*th band. For parabolic band approximation this overlap integral approximately equals to 1. However, since in our case the parabolic or non-parabolic band approximation is not valid, the scattering rate will be overestimated if the integral is taken to be 1. Therefore, this overlap integral must be calculated numerically.

3.2 Non-Polar Optical Phonon Scattering

The probability of non-polar optical phonon scattering from $\boldsymbol{k}$ to $\boldsymbol{k'}$ in reciprocal space is given as

$$P_{NPO}(\boldsymbol{k},\boldsymbol{k'}) = \frac{\pi}{\rho V \omega_q}\begin{bmatrix} N_q \\ N_q+1 \end{bmatrix} I^2_{j,j'}(\boldsymbol{k},\boldsymbol{k'})(D_tK)^2\delta\big(E(\boldsymbol{k'}) - E(\boldsymbol{k}) \mp \hbar\omega_q\big). \quad (3.5)$$

The upper and lower part indicate absorption and emission, respectively. ρ is the density of the crystal, V the normalization volume, ω_q the phonon angular frequency and N_q the number of phonons which is calculated using Eq. (3.2). $I_{j,j'}(\boldsymbol{k},\boldsymbol{k'})$ is the overlap integral over the unit cell. D_tK is the non-polar optical deformation potential. For non-polar optical scattering, the phonon energy $\hbar\omega_q$ is assumed to have a constant value of 85 meV at room temperature and this mechanism is wavevector independent.

3.3 Polar Optical Phonon Scattering

The probability of polar optical phonon scattering from ***k*** to ***k'*** in reciprocal space can be given as

$$P_{PO}(\boldsymbol{k},\boldsymbol{k'}) = \frac{\pi e^2 \omega_q}{V}\begin{bmatrix} N_q \\ N_q+1 \end{bmatrix} \frac{I^2_{j,j'}(\boldsymbol{k},\boldsymbol{k'})}{q^2(\boldsymbol{k},\boldsymbol{k'})}\left(\frac{1}{\epsilon_{high}} - \frac{1}{\epsilon_{low}}\right)\delta\big(E(\boldsymbol{k'}) - E(\boldsymbol{k}) \mp \hbar\omega_q\big). \quad (3.6)$$

The upper and lower part indicate absorption and emission, respectively. e is the electron charge, V the normalization volume, ω_q the phonon angular frequency and N_q the number of phonons which is calculated using Eq. (3.2). $I_{j,j'}(\boldsymbol{k},\boldsymbol{k'})$ is the overlap integral over the unit cell. ϵ_{high} and ϵ_{low} are the high- and low-frequency dielectric constants. For polar optical scattering, the phonon energy $\hbar\omega_q$ is also assumed to have a constant value of 120 meV at room temperature. As we will see, this mechanism is wave vector dependent.

3.4 Coulomb Scattering

The Brooks-Herring approach of impurity scattering from $\boldsymbol{k}$ to $\boldsymbol{k'}$ in reciprocal space is given as [35]

$$P_I(\boldsymbol{k},\boldsymbol{k}') = \frac{2\pi N_I e^4}{\hbar\epsilon_s^2\epsilon_0^2 \mathrm{V}} \frac{\delta\big(E(\boldsymbol{k}') - E(\boldsymbol{k})\big)}{\left[4\left(\frac{k}{\hbar}\right)^2 sin^2(\frac{\alpha}{2}) + \frac{1}{L_D^2}\right]^2} \tag{3.7}$$

where N_I the density of impurities, ϵ the dielectric constant, e the electron charge, V the normalization volume, α the angle between $\boldsymbol{k}$ and $\boldsymbol{k'}$ and L_D the Debye length

$$L_D = \sqrt{\frac{\epsilon_s\epsilon_0 k_B T}{e^2 n}} \tag{3.8}$$

This model cannot describe properly the carrier behavior for heavy doping case. In the case of very high doping, the electrons are easily scattered by multiple impurities at the same time rather than just from a single impurity. To calculate the Coulomb scattering mechanism properly, particle-particle-particle-mesh (P^3M) method in real space is adopted, which will be discussed in the next chapter.

3.5 Calculation of Scattering Rates

The calculation of scattering rates starts from discretization of the irreducible 1st Brillouin zone. In this case, the irreducible 1st Brillouin zone is discretized into 21000 $\boldsymbol{k}$-points and only the first 4 conduction bands are considered. Thus, one has 21000×4 initial states and 21000×4 final states. All widths of delta function are set to 4 meV to get reasonable outcomes. Material parameters for calculating scattering rates are listed in Table 1.1. Figure 3.1 shows the scattering rate for acoustic phonon vs. electron energy,

Figure 3.2 shows the rate for non-polar optical phonon and Figure 3.3 the rate for polar optical phonon. In these plots, each point indicates a scattering rate of a unique pair of initial and final $\boldsymbol{k}$-vectors. Only the plots from 1st band to 1st band are shown here but the same method is applied for other possible initial-final band combinations. It is demonstrated that scattering rates vary even at the same electron energy.

For convenience, all possible intra-band and inter-band mechanisms including acoustic, non-polar optical and polar optical scattering rates calculated are summed in $\boldsymbol{k}$-dependence instead of energy-dependence, which are shown in Figure 3.1 to Figure 3.3. Then, these cumulative scattering tables with their maximum values are normalized so that the rates for all mechanisms are between 0 and 1. The cumulative scattering tables from 1st band to 1st band shown in Figure 3.4 are stored and, thus, ready for future use.

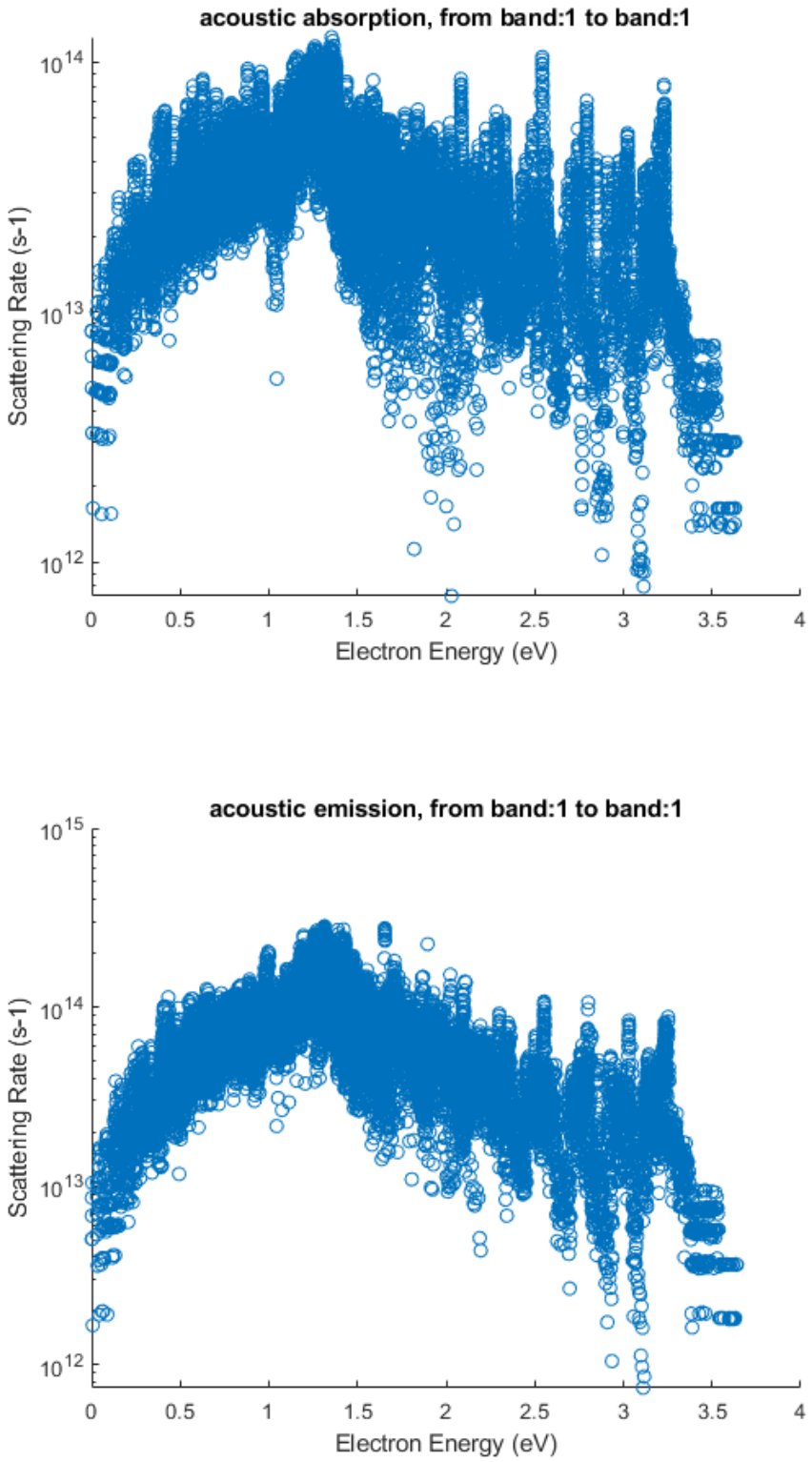

Figure 3.1 Scattering rate of acoustic phonon. (a) Absorption (b) Emission.

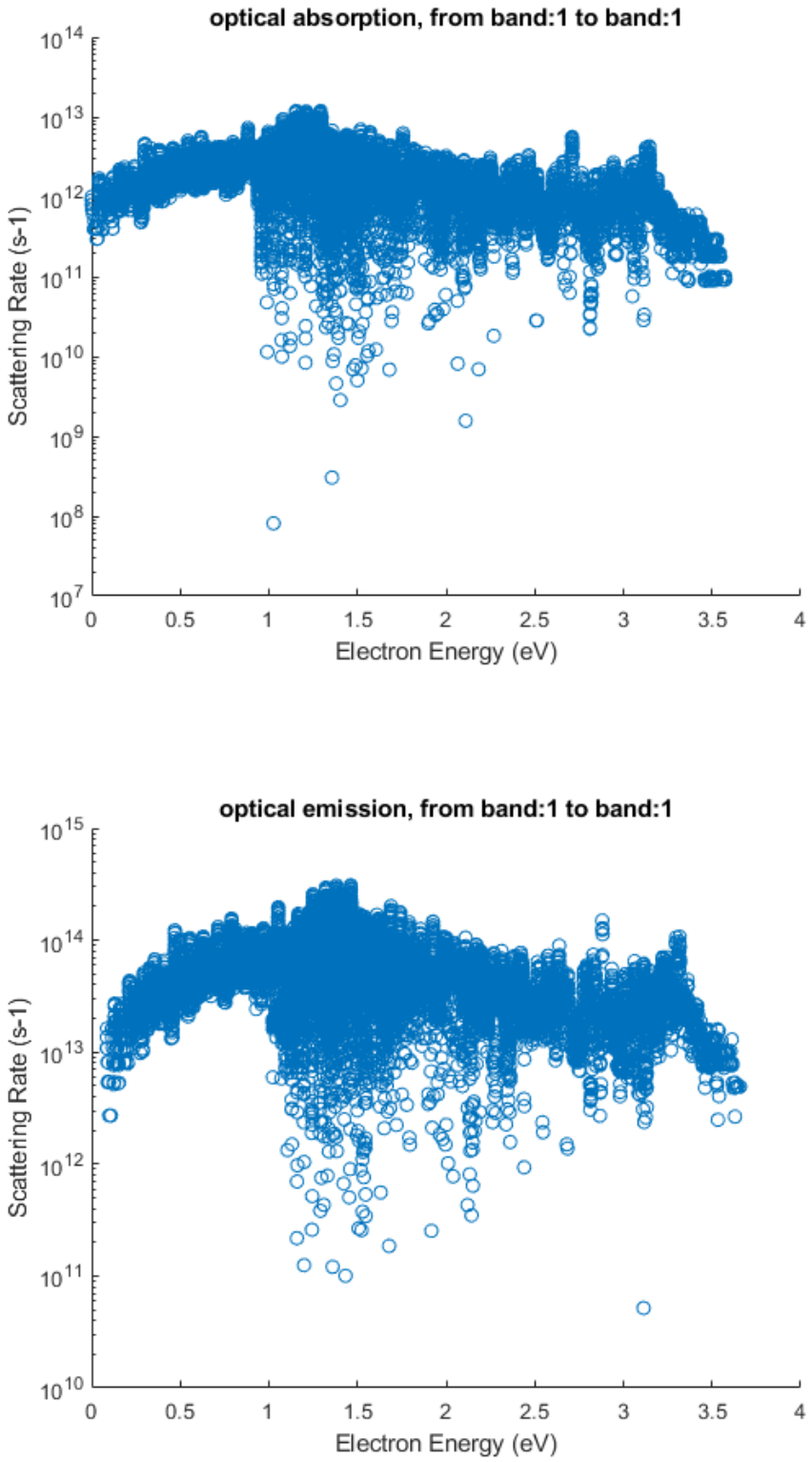

Figure 3.2 Scattering rate of optical phonon. (a) Absorption (b) Emission.

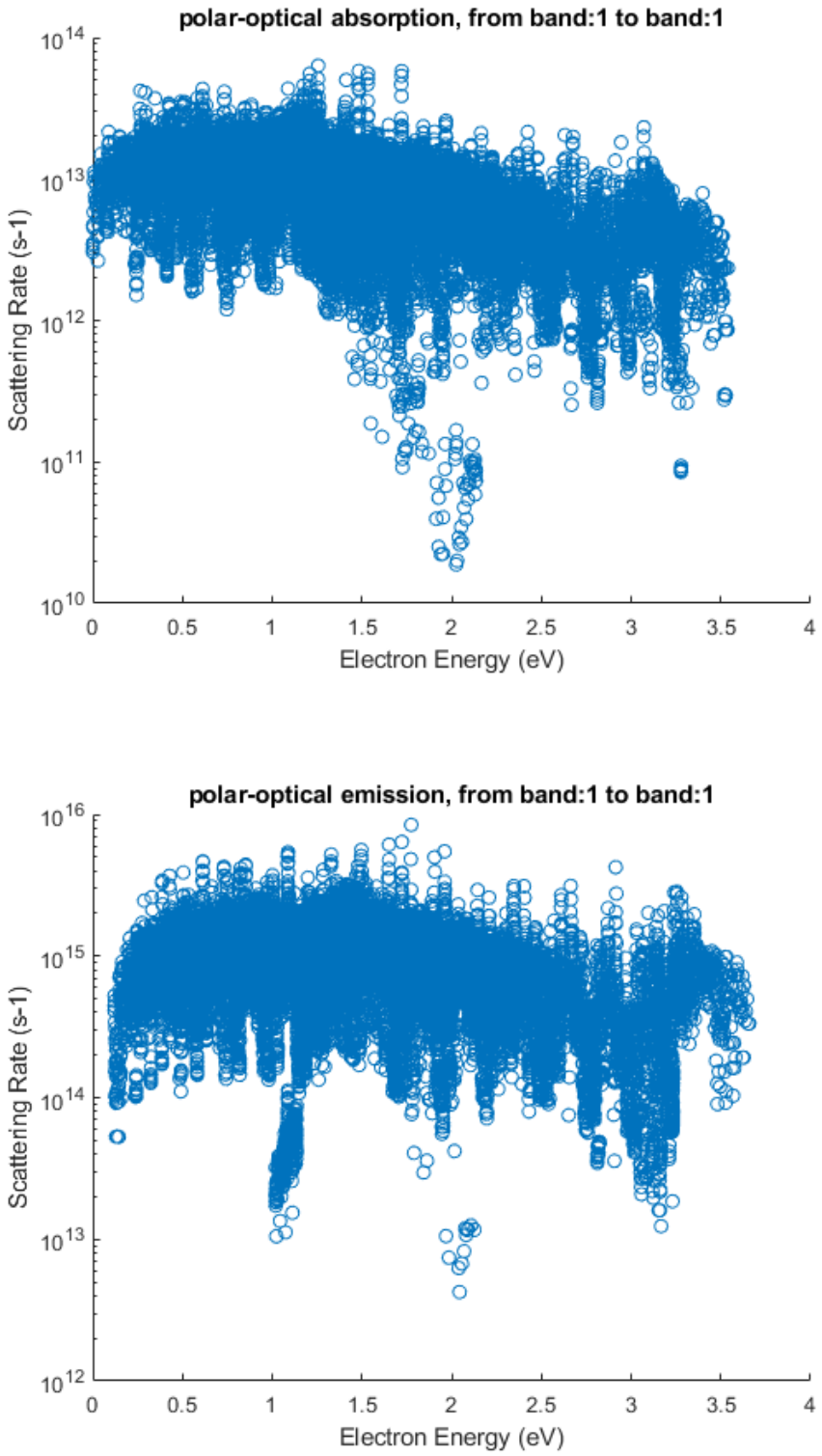

Figure 3.3 Scattering rate of polar optical phonon. (a) Absorption (b) Emission.

Table 3.1 Parameters for the calculation of the scattering rates.

Parameter	**Value**
Acoustic Scattering	
Density ρ (kg/m^3)	3200
Acoustic deformation potential D_A (eV)	19
Non-Polar Optical Scattering	
Non-polar optical deformation potential $D_t K$ (eV/cm)	1.2×10^9
Non-polar optical phonon temperature (K)	989
Polar Optical Scattering	
Polar optical phonon temperature (K)	1393
Low-frequency relative permittivity ϵ_{low}	9.7
High-frequency relative permittivity ϵ_{high}	6.5

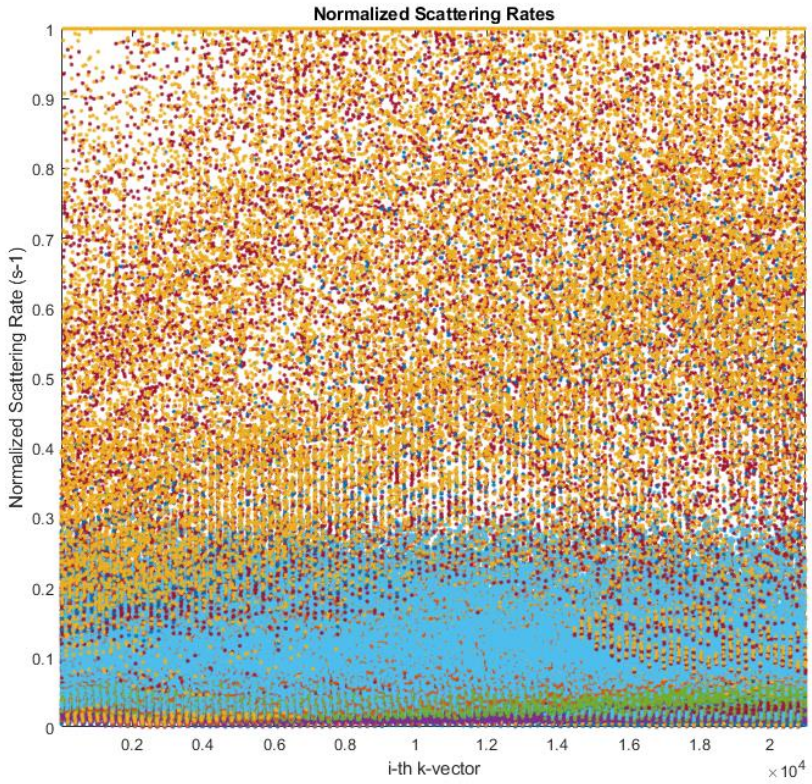

Figure 3.4 The normalized cumulative scattering rate table for the 1st band in the ***k***-dependence. Each column represents the scattering rates for a specific ***k***-vector.

CHAPTER 4

COULOMB SCATTERING

4.1 Introduction of the P^3M method

There are two ways to incorporate the short-range Coulomb interaction in bulk and particle-based device simulations. The first approach treats Coulomb scattering as an additional scattering mechanism in k-space. There are several shortcomings to this approach. First, it is only valid for binary collisions; it ignores scattering from multiple impurities at the same time under heavy doping conditions. Second, electron-plasmon interactions are typically ignored and have to be accounted for as an additional scattering process. For the importance of the electron-plasmon interactions, see the work of Fischetti *et al.* [19] and Wordelman *et al.* [36]. Third, it is difficult to calculate Debye screening length in the case of an inhomogeneous electron gas. Furthermore, this scattering approach model assumes that the scattering is instantaneous, and, as such, cannot describe the interactions correctly in real space and time domain. To solve most of the above-mentioned difficulties, a real-space molecular dynamics (MD) approach is preferable and is, therefore, adopted in this work, via the particle-particle-particle-mesh method.

The particle-particle-particle-mesh method (P^3M) is based on the particle-mesh (PM) method, where charges are assigned to a grid, and the potential is solved based on these charges. The forces solved are applied to each particle according to where it is. PM has been widely used in many-body systems in many fields, not just the nanoelectronics,

e.g., the computational astrophysics. The PM method can successfully describe the behavior of the system most of the time. However, it fails in the short-range force consideration. The nature of it limits the spatial resolution. Considering a very short distance between an impurity and an electron, the mesh force experienced by this electron is almost zero because the charge of the impurity is partially assigned to nearby grids and the force electron experienced is smoothed. On the other hand, in the real Coulomb force calculation the force should approach infinity. To make PM calculation accurate, one needs infinitely small mesh which is impractical and computationally costly.

4.2 Real-space Coulomb Scattering Treatment

To reiterate, real-space Coulomb integration is more accurate than the k-space treatment for several reasons: (1) The non-uniformity in doping will not be a problem; (2) Multiple scattering from different impurities are automatically included; (3) The screening is automatically included, which is very difficult to treat analytically, especially in the case of dynamical screening. One popular method for implementing a real-space Coulomb interaction is the particle-particle-particle-mesh (P^3M). The concept of the P^3M method is to decompose the interparticle force into two parts: the short-range portion, which is calculated directly from the summation of Coulomb forces between particles; and the mesh part (called also the Hartree potential), which is calculated through a particle-mesh coupling.

The total force experienced by a particle *i* can be expressed as

$$F_i = \sum_{j \neq i} F_{ij}^{SR} + \sum_{j \neq i} F_{ij}^{Mesh} \tag{4.1}$$

F_{ij}^{SR} is the short-range force of particle *j* on particle *i*; F_{ij}^{Mesh} is the mesh force of particle *j* on particle *i*. To avoid double counting of the mesh force in the short-range region, a reference force is taken from the exact Coulomb force. The exact short-range Coulomb force one needs to incorporate can be defined as

$$F_{ij}^{SR} = F_{ij}^{Coulomb} - R_{ij} \tag{4.2}$$

where

$$F_{ij}^{Coulomb} = \frac{q_i q_j (\boldsymbol{r_i} - \boldsymbol{r_j})}{4\pi\epsilon |\boldsymbol{r_i} - \boldsymbol{r_j}|^3} \tag{4.3}$$

where q_i and q_j are the particle charges, r_i and r_j are the particle positions. The reference force should equal to the mesh force in the short-range region and equal to the Coulomb force for long-range region. For a uniform mesh, Hockney and Eastwood [37] proposed that one can describe the reference force transitioning smoothly from short range to long range by using a sphere with uniformly decreasing density profile *S(r)*.

$$S(r) = \begin{cases} \frac{48}{\pi r_{sr}^4}\left(\frac{r_{sr}}{2} - r\right), r \le \frac{r_{sr}}{2} \\ 0 \qquad\qquad\quad , r > \frac{r_{sr}}{2} \end{cases} \tag{4.4}$$

In addition, Wordelman and co-workers [36] modified this approach for the non-uniform mesh case. The corresponding reference force $R_{ij}(r)$ can be obtained as

$$R_{ij}(r) = \frac{q_i q_j}{4\pi\epsilon} \times \begin{cases} \frac{1}{35 r_{sr}^2}(224\xi - 224\xi^3 + 70\xi^4 + 48\xi^5 - 21\xi^6) & , 0 \le r \le \frac{r_{sr}}{2} \\ \frac{1}{35 r_{sr}^2}\left(\frac{12}{\xi^2} - 224 + 896\xi - 840\xi^2 + 224\xi^3 + 70\xi^4 - 48\xi^5 + 7\xi^6\right) & , \frac{r_{sr}}{2} \le r \le r_{sr} \\ \frac{1}{r^2} & , r > r_{sr} \end{cases} \tag{4.5}$$

where

$$\xi = \frac{2r}{r_{sr}} \tag{4.6}$$

Figure 4.1 shows an example of the relation between the Coulomb force, the reference force and the short-range force. In this example, the maximum mesh size among three directions is 20 nm, and thus the r_{sr} is taken as 40 nm. It is obvious that the short-range force decay rapidly after a short distance. To check the impact of the mesh size on the short-range force, another mesh size which equals to 10 nm has been compared in Figure 4.2. The solid lines represent the short-range forces from Eq. (4.2). It is observed that within a short range of distance, the short-range force of two mesh sizes are almost the same. Although they split after 5 nm, the magnitudes on 10 nm are both relatively small to the applied electric field while simulating the device. Hence, one can assume that the short-range force is mesh size independent.

Another important note is that, if the distances between the particles are too small, one has to avoid an extremely high and unphysical electric fields that can lead to trapping of the particles (for oppositely charged donors and electrons in the contact region of the device). As shown in Figure 4.2, the solid lines are approaching infinity as the distance is reaching zero. Hence, the short-range force for radius below the cut-off range has to be modified [38]. As adopted in Ref. [38], a cut-off range of linearly decreasing model at distances shorter than 1 nm is used in this work. The example modified short-range forces are illustrated as dot lines in Figure 4.2. For each simulation, the corresponding modified short-range force is calculated based on the maximum mesh size at the initialization step of the simulator and stored as a lookup table for faster computation.

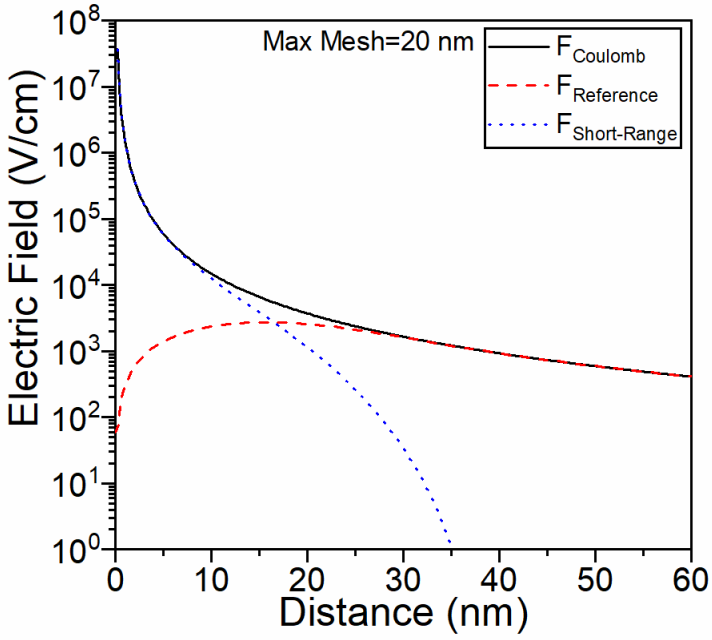

Figure 4.1 Force diagram for 4H-SiC with a uniform mesh. r_{sr} is set to the twice of the maximum mesh size in the x, y and z directions, which is 40nm in this example.

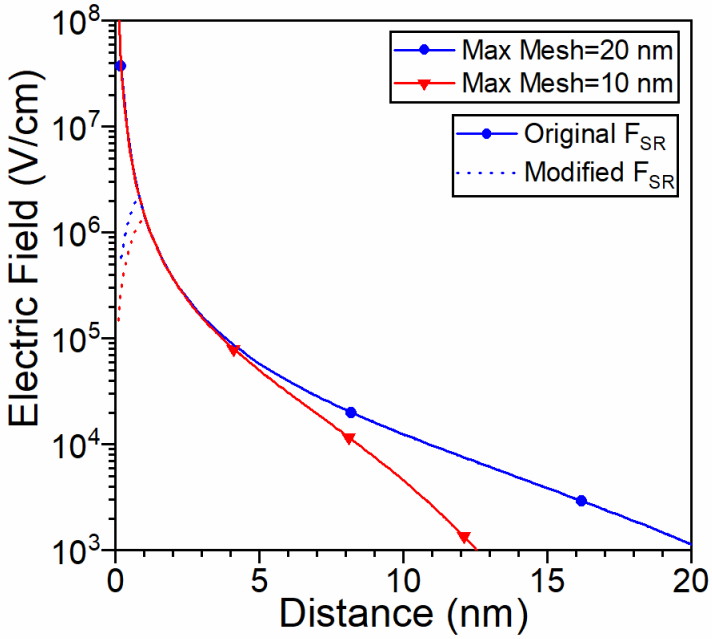

Figure 4.2 Force diagram for 4H-SiC with two different mesh size. (Solid lines) The original short-range forces. (Dot lines) The modified short-range forces.

CHAPTER 5

DEVICE SIMULATION – RESISTOR

5.1 Simulation Procedure

In this chapter, a 3D resistor is being simulated to study low-field transport properties of 4H-SiC. It consists of a 975 nm N-drift layer, on both sides of which are grown 12.5 nm N^+ layers. The doping concentration of the N^+ layer is set to $1 \times 10^{19}\ cm^{-3}$ to ensure a good ohmic contact. The nominal doping concentration of N-drift layer is varied from $1 \times 10^{16}\ cm^{-3}$ to $1 \times 10^{18}\ cm^{-3}$ to investigate the doping dependence of the electron mobility. In addition, since 4H-SiC is anisotropic, the device is assumed to be fabricated along multiple crystallographic directions to study the orientation dependence on the electron mobility and drift velocity. The so-called bias direction (from anode to cathode – as depicted in Figure 5.1) has a finer mesh than the other two directions. The mesh is assumed uniform in each direction to simplify the ensemble Monte Carlo simulation procedure (the particle-mesh coupling). The device structure being simulated is shown in Figure 5.1. The flowchart of the simulation procedure is shown in Figure 5.2.

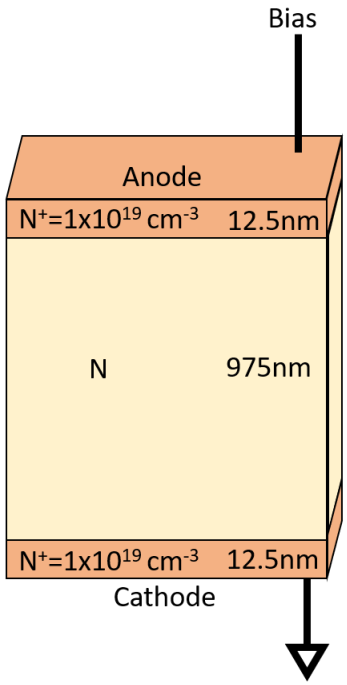

Figure 5.1 Simulated device structure.

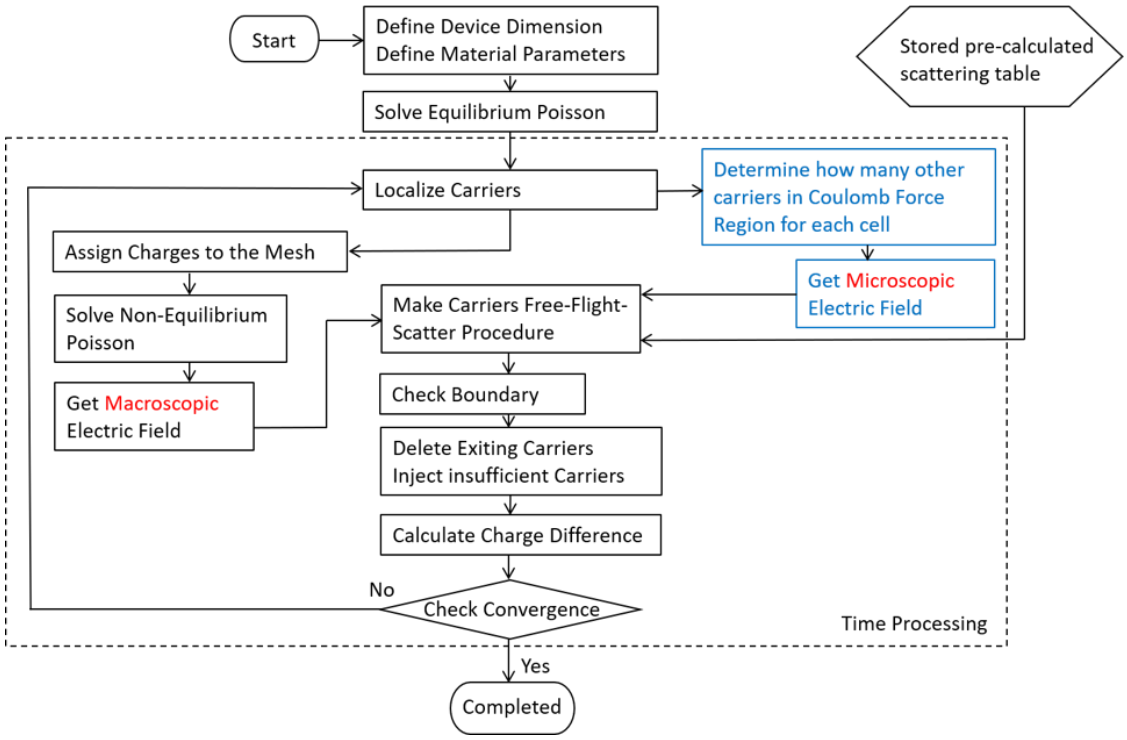

Figure 5.2 Flowchart of the main program for an EMC-P^{3}M simulation.

5.1.1 Initialization

The simulation starts with the initialization of the device geometry and material parameters. An equilibrium Poisson's solver is used to provide a good initial guess for the device simulator. The electrical potential at the boundaries of both electrodes is fixed (Dirichlet boundary conditions) during the solution of the non-equilibrium Poisson's solver. Once the initial guess for the solution is calculated, the simulation is moved from continuous to discrete electron charge representation. For each mesh cube, the number of electrons inside the cube is determined by the product of the electron concentration and the mesh volume. Since the product for each mesh is very small in dense grids, it is very important to validate the impact of the distribution variance. Particles are randomly distributed in each mesh cube. A random energy, a momentum and an initial free-flight time are assigned based on the Maxwell-Boltzmann distribution function. Note that the lowest energy of 4H-SiC is near the M-point. Hence, by symmetry considerations there will be 6 groups of the initial momenta, as illustrated in Figure 5.3.

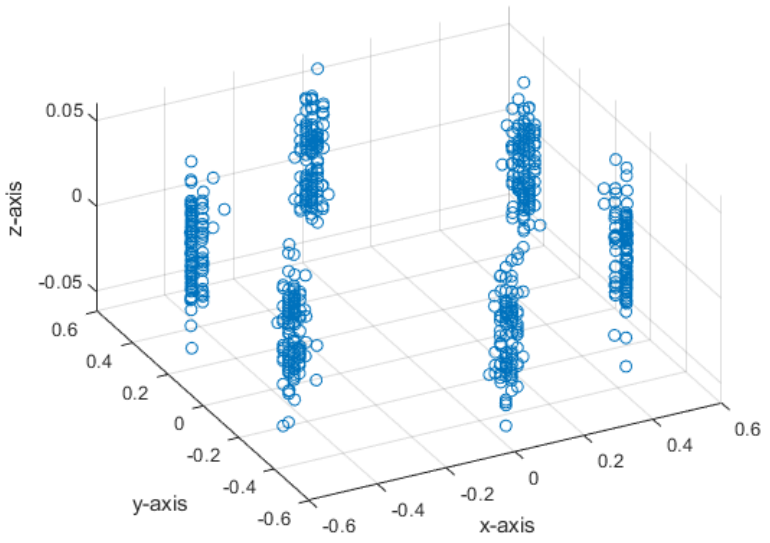

Figure 5.3 Distribution of electron momentum in k-space after initialization in unit of $2\pi/a$.

5.1.2 Implementation of P^3M In Device Simulation

Once the locations of particles are determined, a concept called "box" to calculate the short-range Coulomb force in P^3M method, is adopted. The "box" here is a pseudo mesh and the size of it can be decided by user arbitrarily as shown in Figure 5.4. To simplify the calculation, the width of the box is set to twice of the mesh size in our simulator. Only the interactions of the particles in the boxes around the present box will be considered, because the short-range Coulomb force decays drastically with distance. Thus, the calculation time is dramatically decreased. The corresponding short-range forces can be fetched from the stored look-up data described in CHAPTER 4 , which is called microscopic electric field. The macroscopic electric field is obtained from the 3D Poisson equation solution at the end of the previous time-step. The total electric field

acting on the particle is then the summation of these two components of the electric field.

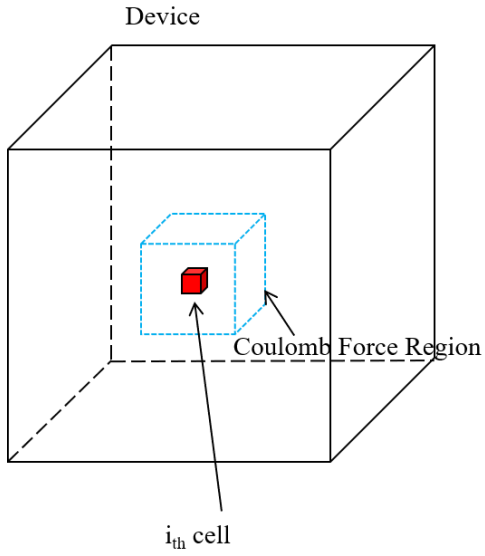

Figure 5.4 Concept of applying P^{3}M in device. For each cell, we only have to consider particles in nearby cells.

5.1.3 Operation of Drift Process

Electrons have different free-flight time Δt_{ff} generated randomly before they are scattered. The synchronous ensemble scheme must be used to perform the transient simulation. Figure 5.5 shows the schematic diagram of it [39]. A fixed time-step, Δt, is introduced to all electrons to synchronize the motions in the system. Every red dot in the figure represents a random, instantaneous scattering event. The scattering may or may not happen during one time-step, depending on the free-flight time Δt_{ff}. This scheme is necessary since it is almost impossible to track all real-time movements of the particles. Over each time-step, the motion of each electrons is simulated independently rather being affected by the other particles. This scheme provides one "frozen snapshot" of the

electric field at a given time. During each time-step Δt, the snapshots are calculated at the beginning and will be used through the end of this time-step. Δt has to be set to a very small value so that the scheme is physically valid as the path traversed by the electron during one time-step should be less than one mesh spacing to avoid unphysical plasma oscillations. Because the free-flight time Δt_{ff} can be longer or shorter than the fixed time-step Δt, the drift time t_{drift} is introduced, which is determined using

$$t_{drift} = \begin{cases} \Delta t, & t_{drift} \geq \Delta t \\ \Delta t_{ff}, & t_{drift} < \Delta t \end{cases}. \tag{5.1}$$

If $t_{drift} \geq \Delta t$, the remainder of the t_{drift} will be used in the subsequent time steps. Once a drift process is called, the change of momentum for each electron is calculated using Newton's second law of motion

$$d\boldsymbol{k}_{total} = -\frac{q}{\hbar} F_{total} t_{drift}. \tag{5.2}$$

where $\boldsymbol{F}_{total}$ is the total electric field:

$$\boldsymbol{F_{total}} = \boldsymbol{F_{mesh(macro)}} + \boldsymbol{F_{SR(micro)}} \tag{5.3}$$

The momentum of each active electron in the ensemble is updated as

$$\boldsymbol{k}_{new} = \boldsymbol{k}_{old} + d\boldsymbol{k}. \tag{5.4}$$

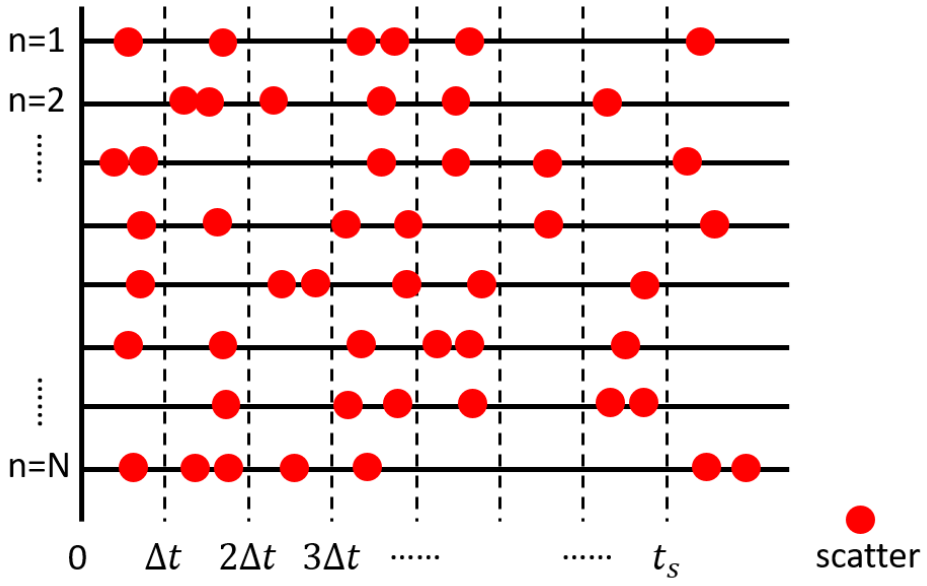

Figure 5.5 Schematic diagram of synchronous ensemble where a fixed time-step Δt is introduced. The red dots indicate random scattering events [39].

There is a very significant difference between the *E-**k*** dispersion relation calculated analytically and the use of a numerical full-band structure. In analytical models, the carriers are assumed to be sitting around the lowest energy state. However, in a full-band analysis, the momentum $\boldsymbol{k}$ is periodic along the Brillouin zone. This means if $\boldsymbol{k}_{new}$ is outside of the 1st Brillouin zone, the corresponding symmetric point has to be found out and mapped the $\boldsymbol{k}$-point back into the 1st Brillouin zone.

The motions in real space of electrons depend on the band structure. The velocity of an electron in real space at time t_s can be acquired by the *E-**k*** dispersion relation:

$$\boldsymbol{v}(t_s) = \frac{1}{\hbar}\nabla_{\boldsymbol{k}}E(\boldsymbol{k}(t_s)). \tag{5.5}$$

where $\nabla_{\boldsymbol{k}}E(\boldsymbol{k}(t))$ is pre-calculated and stored so that it can be quickly accessed. To minimize the sampling error, the drift velocity, v_{drift}, is taken as the average velocity from

the beginning and the end of the free-flight. Therefore, the real-space displacement of an electron is

$$d\boldsymbol{r} = \overline{v_{drift}} \times t_{drift} \tag{5.6}$$

and the location of each active electron is modified accordingly. The drift process takes place repeatedly after every scattering event until reaching the end of the time-step.

5.1.4 Determination of Scattering Events

The drift process is terminated by a scattering event. As mentioned in CHAPTER 3 , the normalized scattering tables have been pre-calculated. The algorithm used to determine which scattering process is chosen and the final state after scattering in this FBEMC simulator is the self-scattering technique (SST), which is shown as Figure 5.6. At the end of the free flight, a uniform random number between 0 and 1 is chosen and is used as a pointer to select one of the phonon scattering mechanisms. Like the example in Figure 5.6, the mechanism 2 has a cumulative scattering rate of Γ_2 and mechanism 3 has a cumulative scattering rate of Γ_3. If a random number between Γ_2 and Γ_3 is generated, the mechanism 3 will be selected. After that the energy and momentum of the electron is changed based on the chosen model. Another example here is that if the random number is larger than the cumulative scattering rate Γ_N of the last mechanism, then the self-scattering is chosen, which means no real scattering is going to happen.

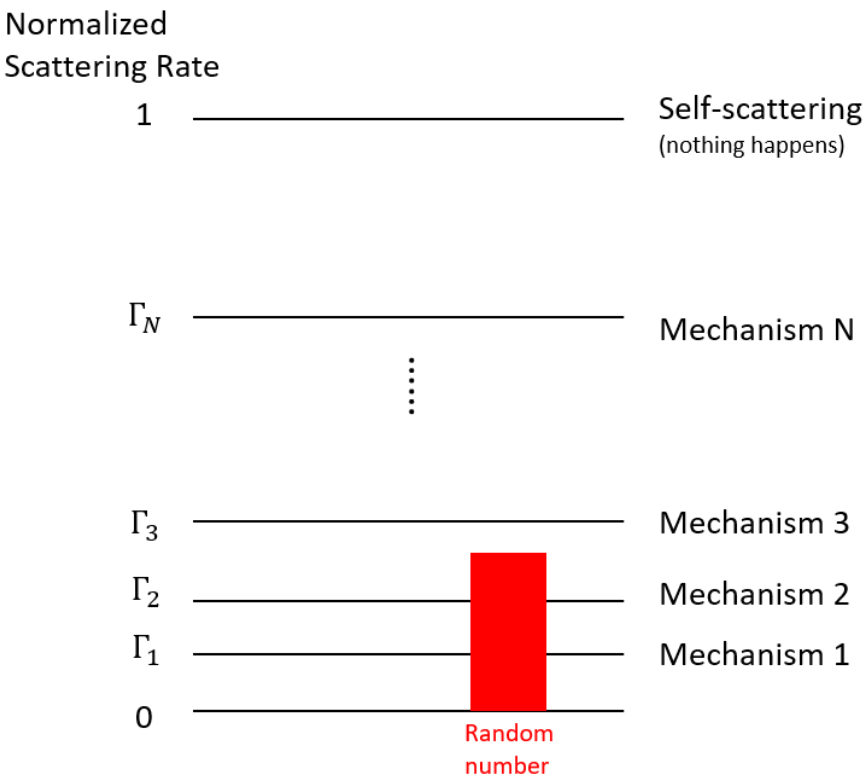

Figure 5.6 Schematic diagram of self-scattering technique. A random number is generated and used to select the scattering mechanism. For example, the mechanism 3 is selected in this case.

5.1.5 Checking contacts and boundaries

For simplicity, there are only ohmic contacts in this 3D resistor. As Figure 5.7 indicates, there are 3 possible situations to keep charge neutrality at the ohmic contacts. The first type is that electrons *naturally* (N_1) drift out the device through contact during time-step. Second one and third one are related to the fact that electrons at the contact mesh are *deleted* (N_2) or *injected* (N_3) respectively to keep charge neutrality. Hence, the exiting charge difference after each time-step is

$$dq = \mathrm{q}(N_1 + N_2 - N_3), \tag{5.7}$$

where N_1, N_2 and N_3 are the number of electrons of each type mentioned above. The number of cumulative exiting charges at the time $\mathrm{t} + \Delta\mathrm{t}$ equals to

$$Q(t + \Delta t) = Q(t) + dq. \tag{5.8}$$

Thus, the current can be calculated as the slope of the charges

$$I = \frac{dQ(t)}{dt} = \frac{dq}{\Delta t}. \tag{5.9}$$

There is also a possibility that the electron leaves the artificial boundary of the device during the drift process. If this happens, the position and momentum are reflected back, so the electron is kept inside the device domain.

Once the drift and the scattering processes are completed, at the observation times, the charges are coupled to the mesh through the nearest-element-center (NEC) method that eliminates the self-force. The Poisson equation is solved next based on the coupled charge density and the boundary conditions. The process is repeated again and again until the end of the simulation time. The overall simulation time must be long enough to ensure steady-state conditions, which can be determined by checking the number of particles going in and out through the electrodes.

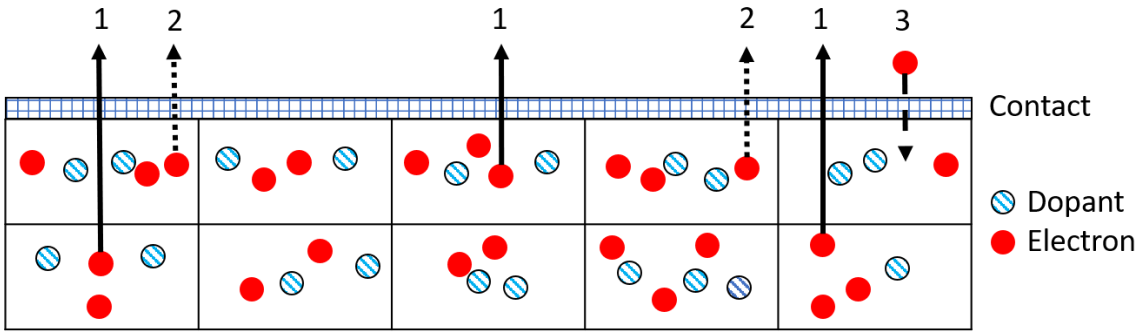

Figure 5.7 Possible situations to keep charge neutrality at the ohmic contacts.
(1) Electrons naturally drifts out during time-step, N_1. (2) Electrons are deleted, N_2.
(3) Electrons are injected, N_3.

5.2 Simulation Results

Key interest in the first part of this dissertation work is the understanding of the axis-dependence of the electron velocity and mobility. Here the results of applied bias along [0001] and $[11\bar{2}0]$ axes are demonstrated. The relating directions on atoms arrangement in real space are shown in Figure 5.8. An example of the projected electron distribution in steady state is shown in Figure 5.9. The elapsed time is 8 ps, the bias is 20V and $N_d = 1 \times 10^{17}\ cm^{-3}$. Figure 5.10 shows the cumulative number of electrons exiting anode and cathode. The number of electron exiting anode is positive; it is negative for exiting cathode, which means electrons are injecting into cathode. The slope, which is the current as well, is stable after a while and is an indication of conservation of current and convergence. To get reliable statistical data, only the electrons in the central drift region are considered; electrons at both electrodes are not considered. The electrons inside the same mesh cube are coupled to the mesh, and the quantities are averaged. Note that each curve corresponds to different dopant distribution in the 3D resistor.

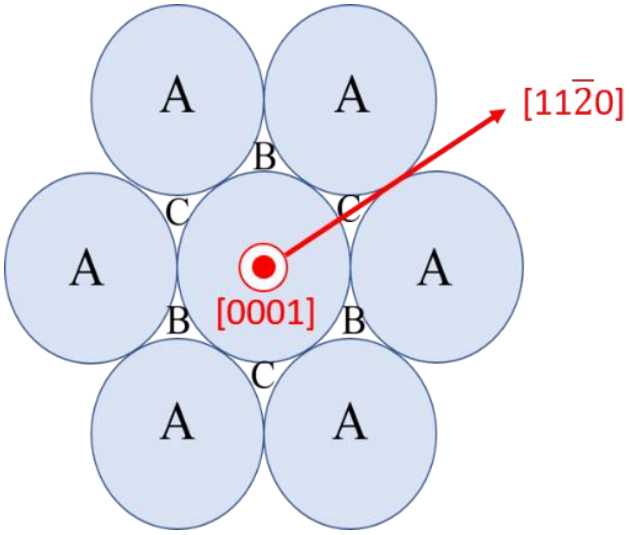

Figure 5.8 The directions along [0001] and [11-20] axes relating to the real space atoms arrangement.

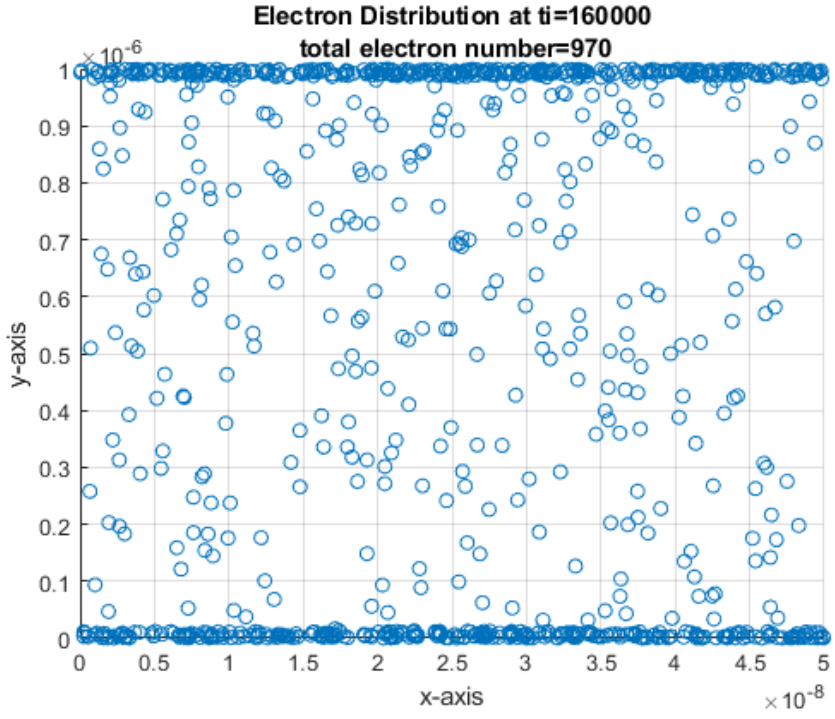

Figure 5.9 An example of projected electron distribution in steady state. The elapsed time is 8 ps, the bias is 20V and $N_d=1\times10^{17}$ cm^{-3}.

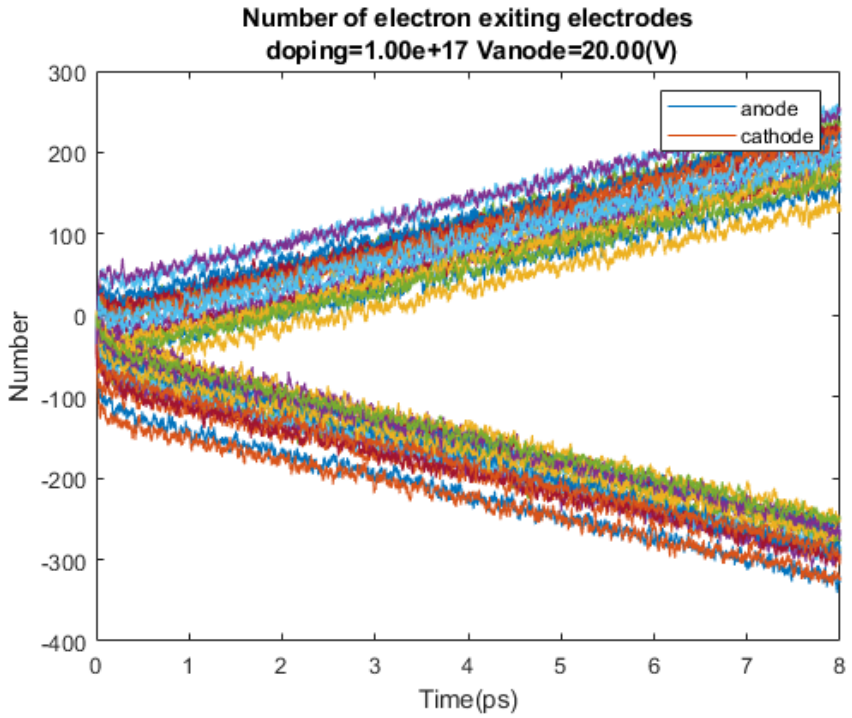

Figure 5.10 An example of cumulative number of electrons exiting anode and cathode. The number of electron exiting anode is positive; it is negative for exiting cathode, which means electrons are injecting into cathode.

5.2.1 Potential and electric field distribution

Figure 5.11 illustrates the potential and electric field profiles of three different doping concentrations under bias of 30 V along the [0001] direction. Each line in the plots represents one EMC simulation result and lines correspond to different random dopant distribution profiles. If one takes into consideration Figure 5.11(c) for example, the maximum and minimum of potential at depth=400 μm is 19.5 and 14 V, respectively. It is almost 39% difference which cannot be neglected. This trend is more pronounced at lower voltages. To collect more data for a range of electric field, the device is biased at four different voltages and the potential and electric field are plotted in Figure 5.12.

Figure 5.13 illustrates the averaged potential and averaged electric field profiles under four bias conditions along [0001] and [11$\bar{2}$0] directions of a resistor with doping density $N_d = 1 \times 10^{17}\ cm^{-3}$. Each line in the plots represents the average of 20 lines corresponding to 20 different random dopant distribution profiles. The potential of two crystalline directions are very close. If one check the electric field, both directions have almost same results at low bias. However, at 90V, the plots show great difference. This affirms the necessity of the full-band analysis under high electric field.

A fixed dopant distribution is also used to check if the variance comes from the Monte Carlo calculation process, or the dopant distribution. Figure 5.14 shows the profiles of 10 Monte Carlo runs for the exact same dopant distribution. The results are overlapping perfectly, indicating that the variance is attributed to the randomly distributed dopants. For designing a small-scale device, this issue becomes much more noticeable.

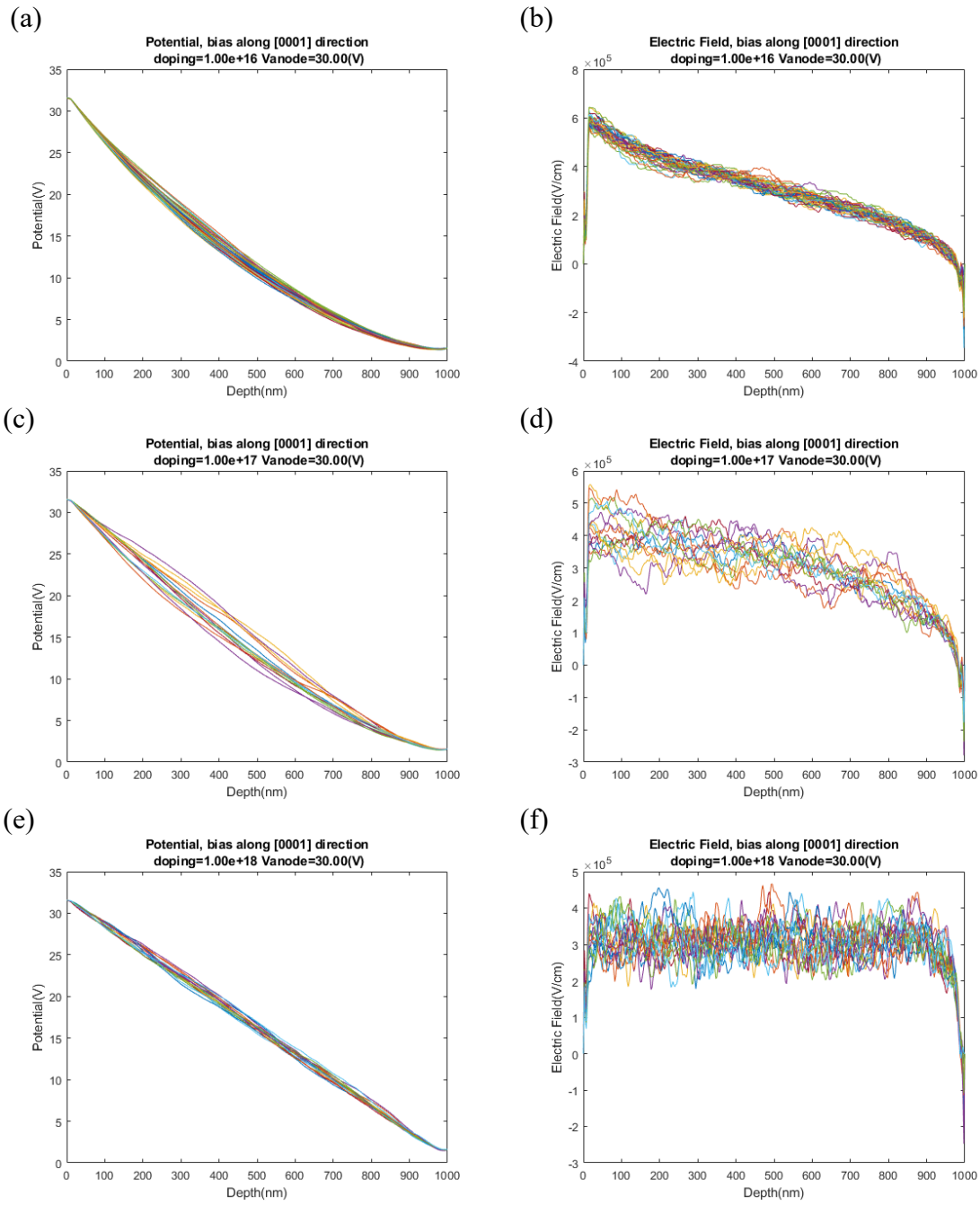

Figure 5.11 Potential and electric field profiles of three different doping concentrations under bias=30 V along [0001] direction (c-axis). (a) (b) $N_d=1\times10^{16}$ cm^{-3}, (c)(d) $N_d=1\times10^{17}$ cm^{-3}, (e)(f) $N_d=1\times10^{18}$ cm^{-3}.

(a)

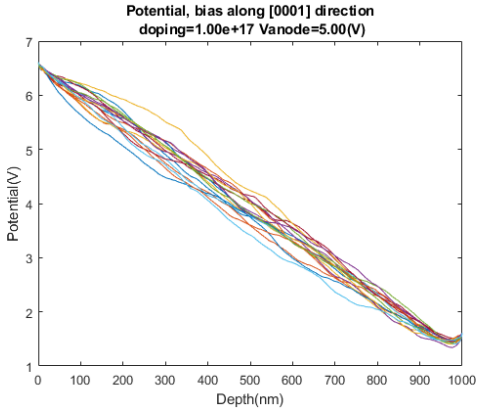
Potential, bias along [0001] direction
doping=1.00e+17 Vanode=5.00(V)
Potential(V)
Depth(nm)

(b)

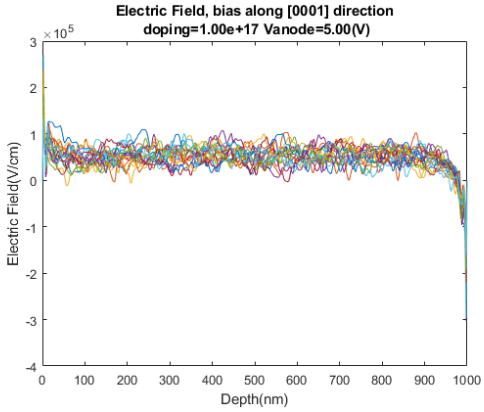
Electric Field, bias along [0001] direction
doping=1.00e+17 Vanode=5.00(V)
×10^5
Electric Field(V/cm)
Depth(nm)

(c)

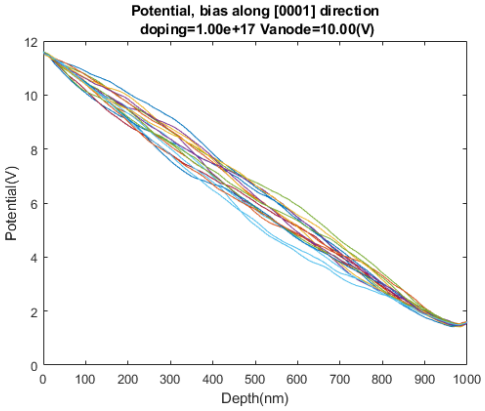
Potential, bias along [0001] direction
doping=1.00e+17 Vanode=10.00(V)
Potential(V)
Depth(nm)

(d)

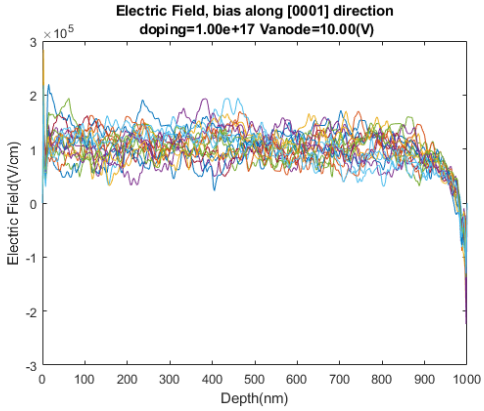
Electric Field, bias along [0001] direction
doping=1.00e+17 Vanode=10.00(V)
×10^5
Electric Field(V/cm)
Depth(nm)

(e)

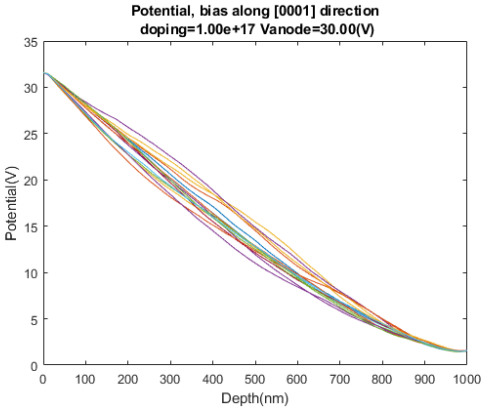
Potential, bias along [0001] direction
doping=1.00e+17 Vanode=30.00(V)
Potential(V)
Depth(nm)

(f)

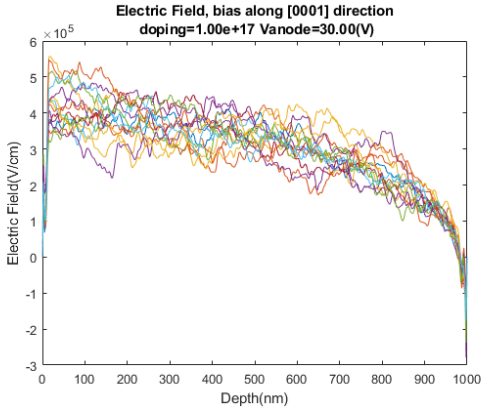
Electric Field, bias along [0001] direction
doping=1.00e+17 Vanode=30.00(V)
×10^5
Electric Field(V/cm)
Depth(nm)

(g)

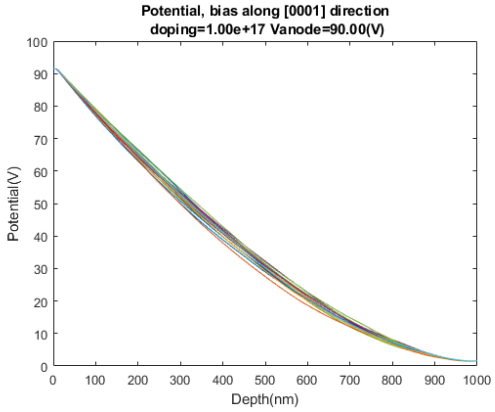

(h)

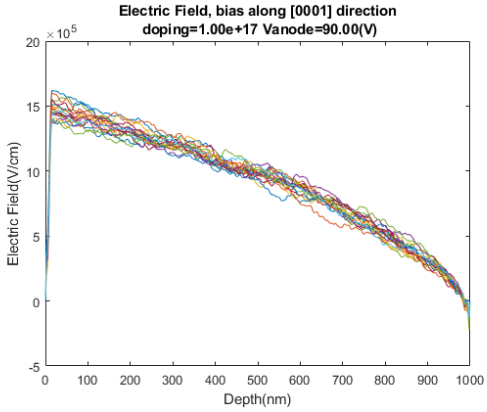

Figure 5.12 Potential and electric field profiles of four different bias along [0001] direction (c-axis) under N_d=1×10^{17} cm^{-3}. (a) (b)$V = 5\ V$, (c)(d) $V = 10\ V$, (e)(f) $V = 30\ V$, (g)(h)$V = 90\ V$.

(a)

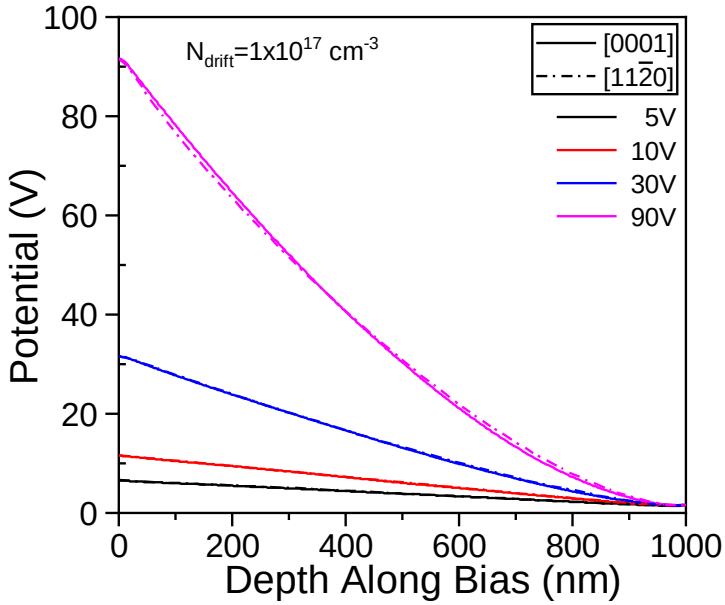

(b)

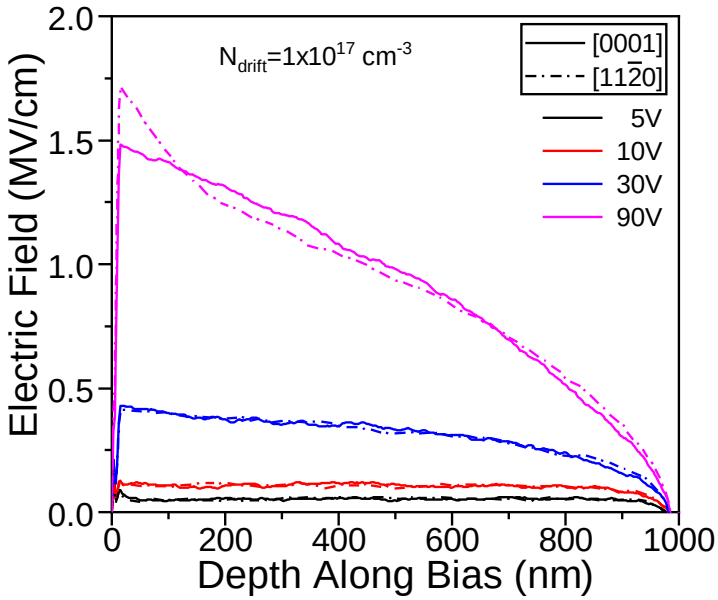

Figure 5.13 (a) The averaged potential and (b) averaged electric field profiles for a resistor with $N_d=1\times10^{17}$ cm^{-3} along [0001] (solid) and [11-20] (dashed) directions.

(a)

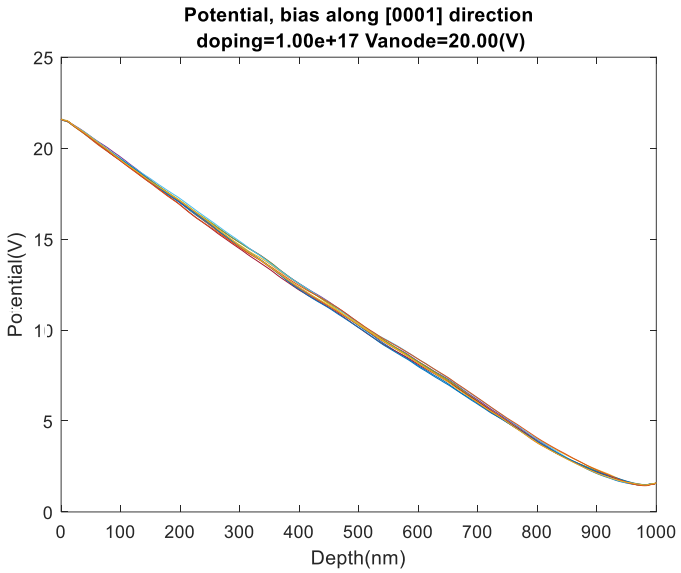

(b)

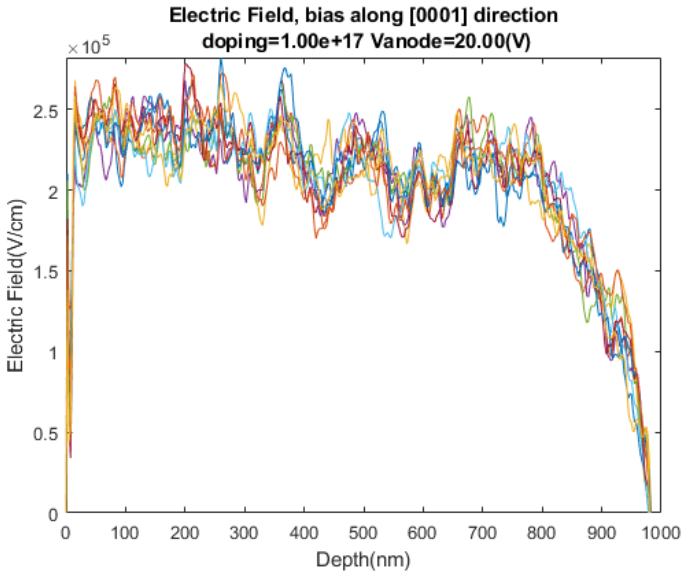

Figure 5.14 (a) Potential and (b) electric field profiles along [0001] direction (c-axis) under $N_d=1\times10^{17}$ cm^{-3}, bias=20 V. Results of 10 Monte Carlo runs for the exact same dopant distribution are overlapped.

5.2.2 Electrical properties

The current density for both [0001] and [11$\overline{2}$0] directions for the applied biases is summarized in Figure 5.15. Current density for both [0001] and [11$\overline{2}$0] directions as a function of the applied bias. Parameter in these figures is the doping of the N-region. For low doping concentration case like $N_d = 1 \times 10^{16}\ cm^{-3}$ or $N_d = 3 \times 10^{16}\ cm^{-3}$, the error might be amplified because of the limited number of particles in the calculation. The saturation of the current density is clearly observed in both crystallographic directions. This behavior meets our expectations in that the electron velocity is saturated under high electric fields. It is also observed that the current density ratio between each doping concentration is lower than the doping ratio. The current density ratio $R = \frac{J(N_d=1\times10^{18})}{J(N_d=3\times10^{17})} = 2.91$ when the applied bias equals 90 V. However, it drops down to about 2.38 when the applied bias equals 10 V. This is an indicator that Coulomb scattering does play an important role, especially at low voltages.

Figure 5.16 displays the current density ratio as a function of the applied voltage for different doping concentrations. It is defined as a ratio of the current density along the [0001] direction that is divided by the current density along the [11$\overline{2}$0] direction. Schaffer *et al.* [40] reported that the mobility parallel to the c-axis, $\mu_{||,c}$, is about 1.2 times higher when compared to the mobility perpendicular to c-axis, $\mu_{\perp,c}$, in 4H-SiC, but they didn't specify which direction was the one perpendicular to the c-axis. These ratios in our case range from 1.25 to 1.75. This behavior is comparable to the reported value. For smaller doping concentrations and lower voltages, the ratio is higher. This latter result illustrates the anisotropic property of 4H-SiC.

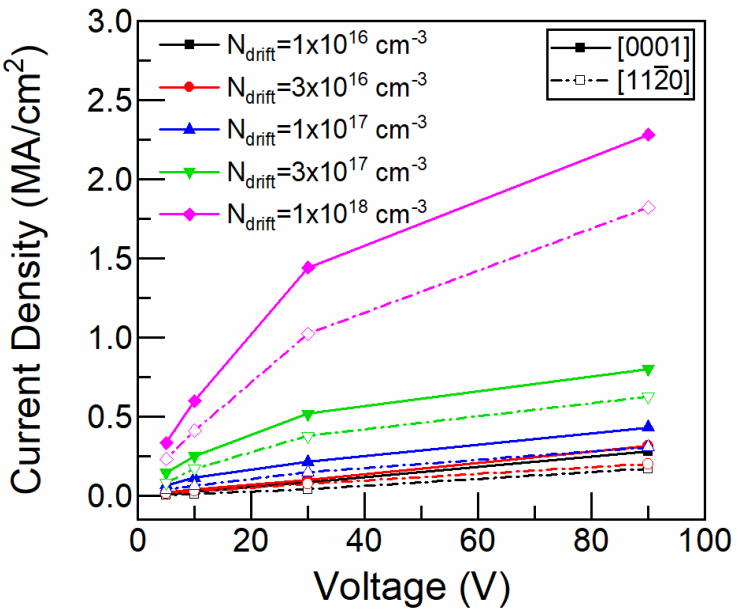

Figure 5.15 Current density for both [0001] and [11-20] directions as a function of the applied bias. Parameter in these figures is the doping of the N-region.

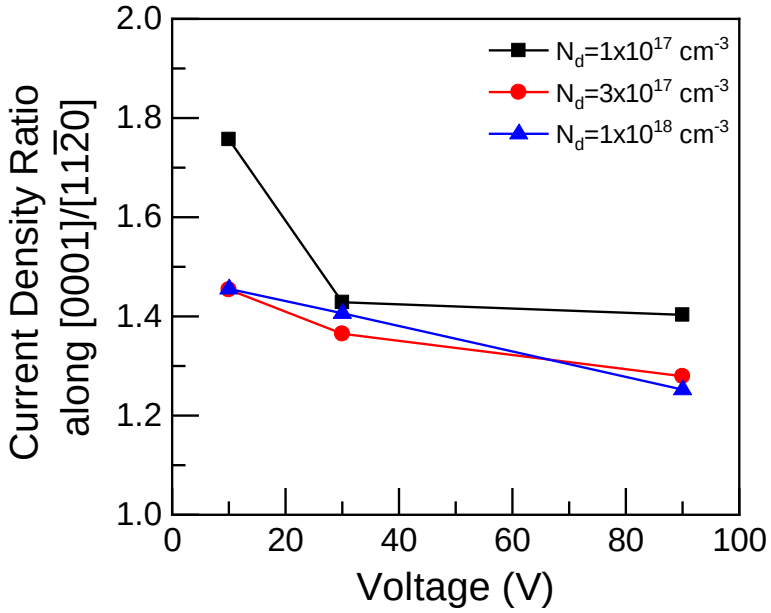

Figure 5.16 Current density ratio, which is defined as current density along the [0001] direction divided by current density along the [11-20] direction, as a function of the applied voltage for different doping concentrations.

5.2.3 Electron velocity and mobility distribution

So far, the focus of the work has been on macro-scale quantities. However, the advantage of using the Ensemble Monte Carlo (EMC) device simulator is that micro-scale quantities can also be analyzed and calculated. Figure 5.17 depicts scatter distributions of the electron velocity vs. electric field along the [0001] direction. The group-like distribution is because only four bias voltages are considered, due to limited computing resources. However, the trend can still be observed. Figure 5.17 strongly suggests that the electron velocity in the device is not just a fixed value, but a distribution. It includes high- and low-velocities for different resistors, which have different numbers and/or different distributions of the impurity atoms in the active region, even though they are characterized with same nominal or average doping density value. As expected, the electron velocity increases with the electric field in this range. If one divides the electron velocity by the local electric field, the electron mobility-electric field distribution is as shown in Figure 5.18.

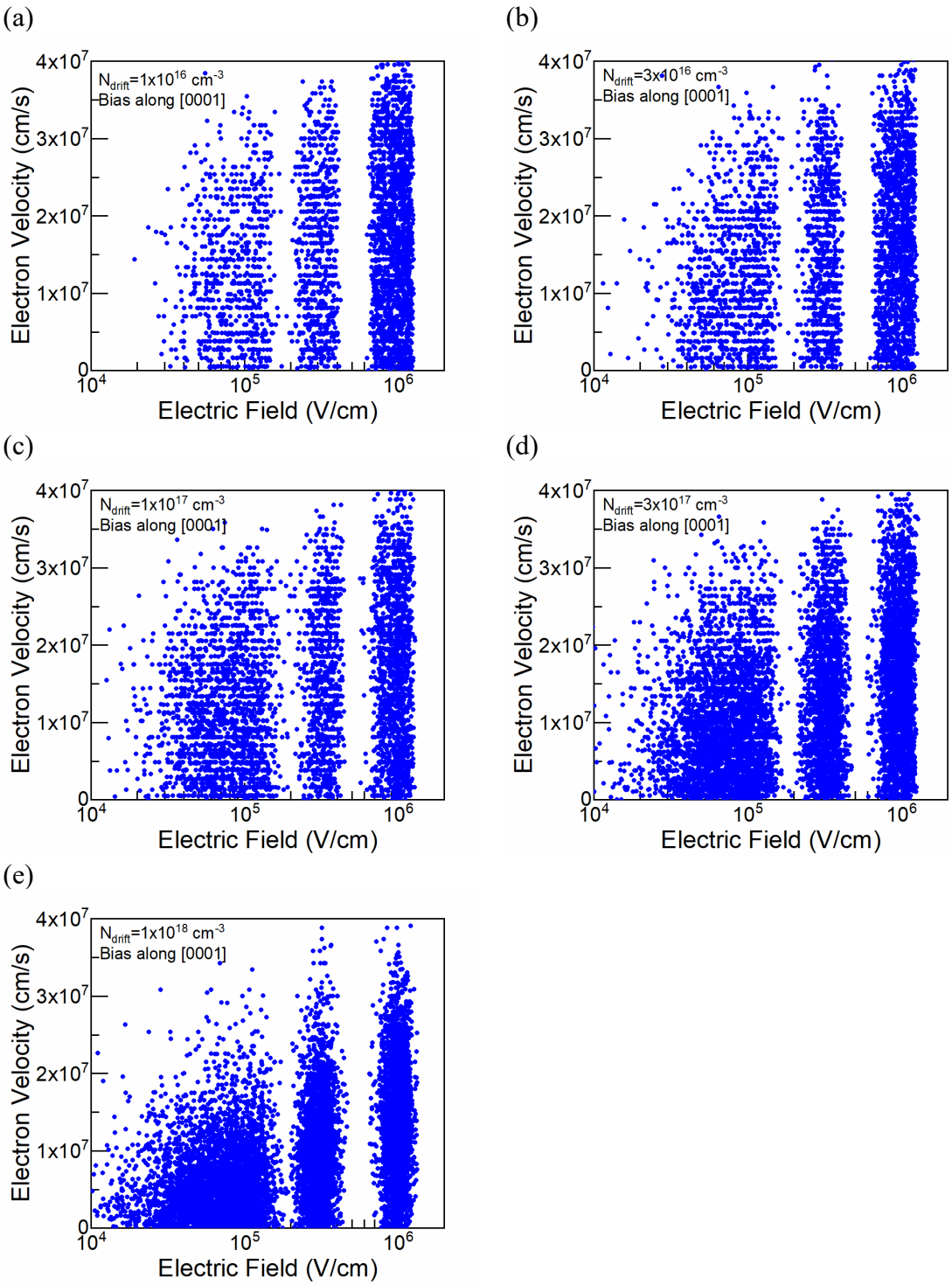

Figure 5.17 Scatter distributions of electron velocity vs. electric field of five different doping concentrations along [0001] direction. (a) $N_d=1\times10^{16}$ cm^{-3} (b) $N_d=3\times10^{16}$ cm^{-3} (c) $N_d=1\times10^{17}$ cm^{-3} (d) $N_d=3\times10^{17}$ cm^{-3} (e) $N_d=1\times10^{18}$ cm^{-3}.

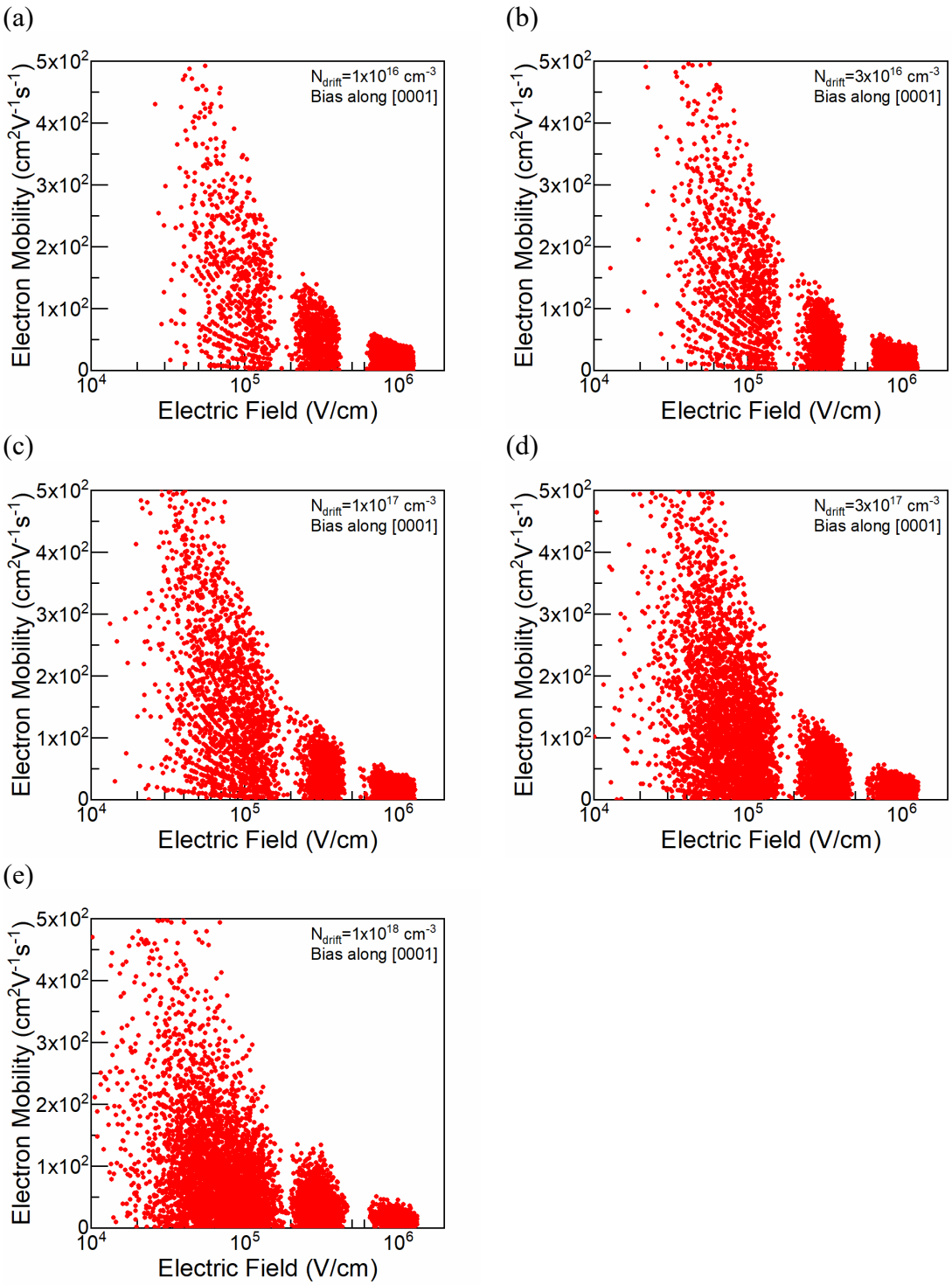

Figure 5.18 Scatter distributions of electron mobility vs. electric field of five different doping concentrations along [0001] direction. (a) $N_d=1\times10^{16}$ cm^{-3} (b) $N_d=3\times10^{16}$ cm^{-3} (c) $N_d=1\times10^{17}$ cm^{-3} (d) $N_d=3\times10^{17}$ cm^{-3} (e) $N_d=1\times10^{18}$ cm^{-3}.

To compare simulation results presented in Figure 5.17 and Figure 5.18 with experimental data and analytical expression, the electric field range is discretized into several bins and the quantities in each bin are averaged with weighting. The average electric field and the average electron velocity are defined as

$$\overline{F_i} = \frac{1}{k}\sum_{j=1}^{k} F_j \tag{5.10}$$

$$\overline{v_i} = \frac{\sum_{j=1}^{k} v_j F_j}{\sum_{j=1}^{k} F_j} \tag{5.11}$$

where i is the index of the bin and k is the total sample number in the i_{th} bin. These results are compared with the experimental data of Khan and Cooper [41], who measured the high-field electron transport in 4H and 6H-SiC and provided an empirical fit equation. For 4H-SiC the empirical fit relation reads:

$$v(F) = \frac{\mu_{low} F}{\left[1 + \left(\frac{\mu_{low} F}{v_s}\right)^{\alpha}\right]^{\frac{1}{\alpha}}} \tag{5.12}$$

where $\mu_{low} = 450\ cm^2/Vs$, $v_s = 2.2 \times 10^7\ cm/s$ and $\alpha = 1.2$. However, this equation is independent of doping concentration. To cover the doping dependence, a widely used expression by Caughey and Thomas [42] is used:

$$\mu_{low} = \mu_{min} + \frac{\mu_{max} - \mu_{min}}{\left[1 + \left(\frac{N_D + N_A}{N^{ref}}\right)^{\gamma}\right]} \tag{5.13}$$

where $\mu_{max} = 947\ cm^2/Vs$, $\mu_{min} = 0\ cm^2/Vs$, $N^{ref} = 1.94 \times 10^{17}\ cm^3$ and $\gamma = 0.61$ [43]. (Note that the values in (5.12) and (5.13) are for mobility perpendicular to [0001] direction, or along the c-axis.) Schaffer *et al.* [40] reported that the mobility parallel to c-axis, $\mu_{||,c}$, is about 1.2 times of the mobility perpendicular to c-axis, $\mu_{\perp,c}$, in 4H-SiC.

Furthermore, one must consider the two-level incomplete ionization in 4H-SiC, which is given by [43]

$$N_d{}^+ = \frac{\alpha_{ii} N_d}{\left[1 + 2exp\left(\frac{(E_{Fn} - E_c) + E_{d,cubic}}{kT_L}\right)\right]} + \frac{(1 - \alpha_{ii}) N_d}{\left[1 + 2exp\left(\frac{(E_{Fn} - E_c) + E_{d,hexagonal}}{kT_L}\right)\right]} \qquad (5.14)$$

α_{ii} is the ratio between cubic and hexagonal structure, $E_{d,cubic}$ and $E_{d,hexagonal}$ are the ionization energies for donors. For 4H-SiC, $\alpha_{ii} = 0.5$, $E_{d,cubic} = 0.09\ eV$ and $E_{d,hexagonal} = 0.05\ eV$. E_{Fn} is the Fermi level of electrons. Since in a device E_{Fn} varies with distance, this approximate ionization rate represented with Eq. (5.14) may not be accurate. However, the result given in Eq. (5.14) can still give us a general value. The corresponding ionized dopant concentration vs. doping concentration is plotted in Figure 5.19. The red dots indicate the doping concentration used for fitting. For example, to get the ionized dopant concentration of $N_d{}^+ = 1 \times 10^{16}\ cm^{-3}$, a doping concentration equal to $N_d = 1 \times 10^{16}\ cm^{-3}$ is enough. However, to get ionized dopant concentration of $N_d{}^+ = 3 \times 10^{17}\ cm^{-3}$, a doping concentration equal to $N_d = 6.35 \times 10^{17}\ cm^{-3}$ is needed. For $N_d{}^+ = 1 \times 10^{18}\ cm^{-3}$, Eq. (5.14) does not give a practical result, so $N_d = 4 \times 10^{18}\ cm^{-3}$ is used in this case.

Combining all these observations, one arrives at the results presented in Figure 5.20 and Figure 5.21 , which show the averaged distributions of electron mobility vs. electric field for five different doping concentrations along [0001] direction. The dots indicate the averaged sample points, whereas the triangles in Figure 5.20(c) and Figure 5.21(c) denote the experimental data from Ref. [41]. The dash line represents the calculations of Eqs. (5.12) and (5.13) only. When one additionally considers Eq. (5.14), these results are

presented with solid lines. From the data presented, it is evident that the averaged sample points fit the experimental data and the models very well. In addition, the ratio=1.5, which is the current density along [0001] direction divided by current density along $[11\bar{2}0]$ direction in [40], is also introduced into this fitting, as shown in Figure 5.22. The plots match the models, too. The only mismatch is in the low electric field region of ${N_d}^+ = 1 \times 10^{18}\ cm^{-3}$ curve. This may be a consequence of the constant Fermi level assumption in the incomplete ionization consideration.

Also, the phonon-limited electron drift velocity and mobility along [0001] direction are compared to the data extracted from the resistor and the experimental data, as shown in Figure 5.23 and Figure 5.24. The doping concentration of the experimental data is $N_d = 1.4 \times 10^{17}\ cm^{-3}$. From the results presented it is obvious that the inclusion of Coulomb scattering is needed to match the experimental data for both the electron drift velocity and the electron mobility.

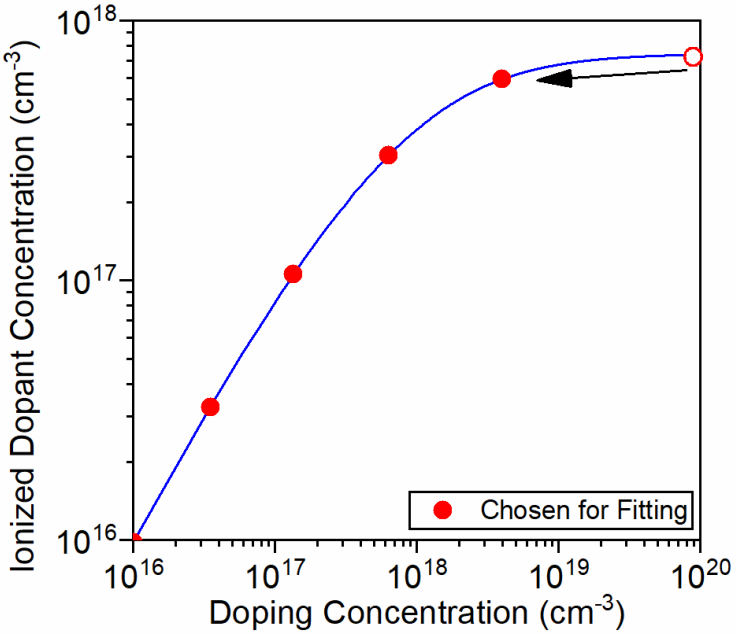

Figure 5.19 The ionized dopant concentration vs. the doping concentration with the two-level incomplete ionization introduced. The red dots indicate the doping concentration used for fitting.

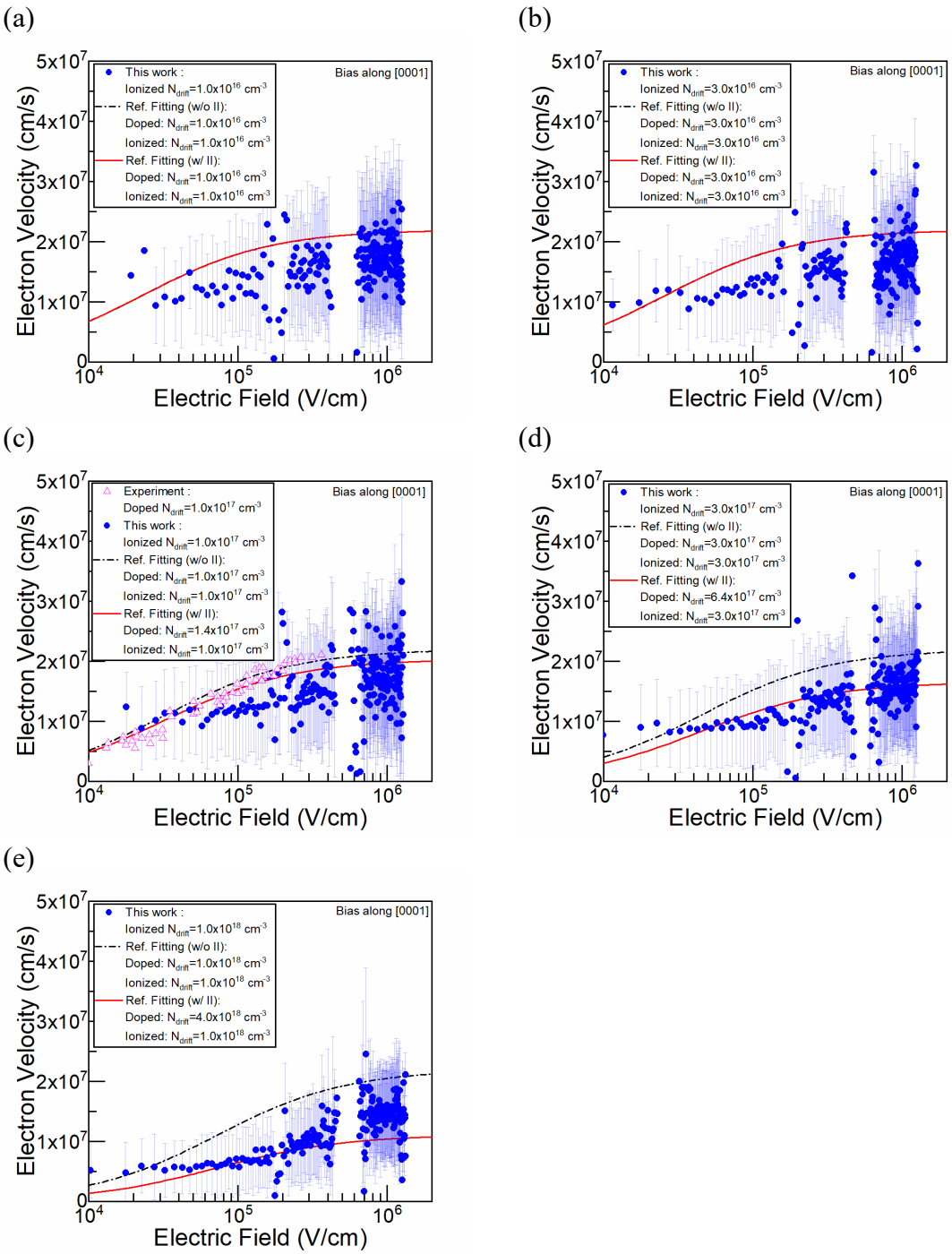

Figure 5.20 Electron velocity and averaged distributions of electron velocity vs. electric field for five different doping concentrations along [0001] direction in this work (dots). Triangles denote the experimental data from Ref. [41]. The dashed line indicates the model without considering the effect of incomplete ionization. The solid line represents the model with incomplete ionization. (a) N_d=1×10^{16} cm^{-3} (b) N_d=3×10^{16} cm^{-3} (c) N_d=1×10^{17} cm^{-3} (d) N_d=3×10^{17} cm^{-3} (e) N_d=1×10^{18} cm^{-3}.

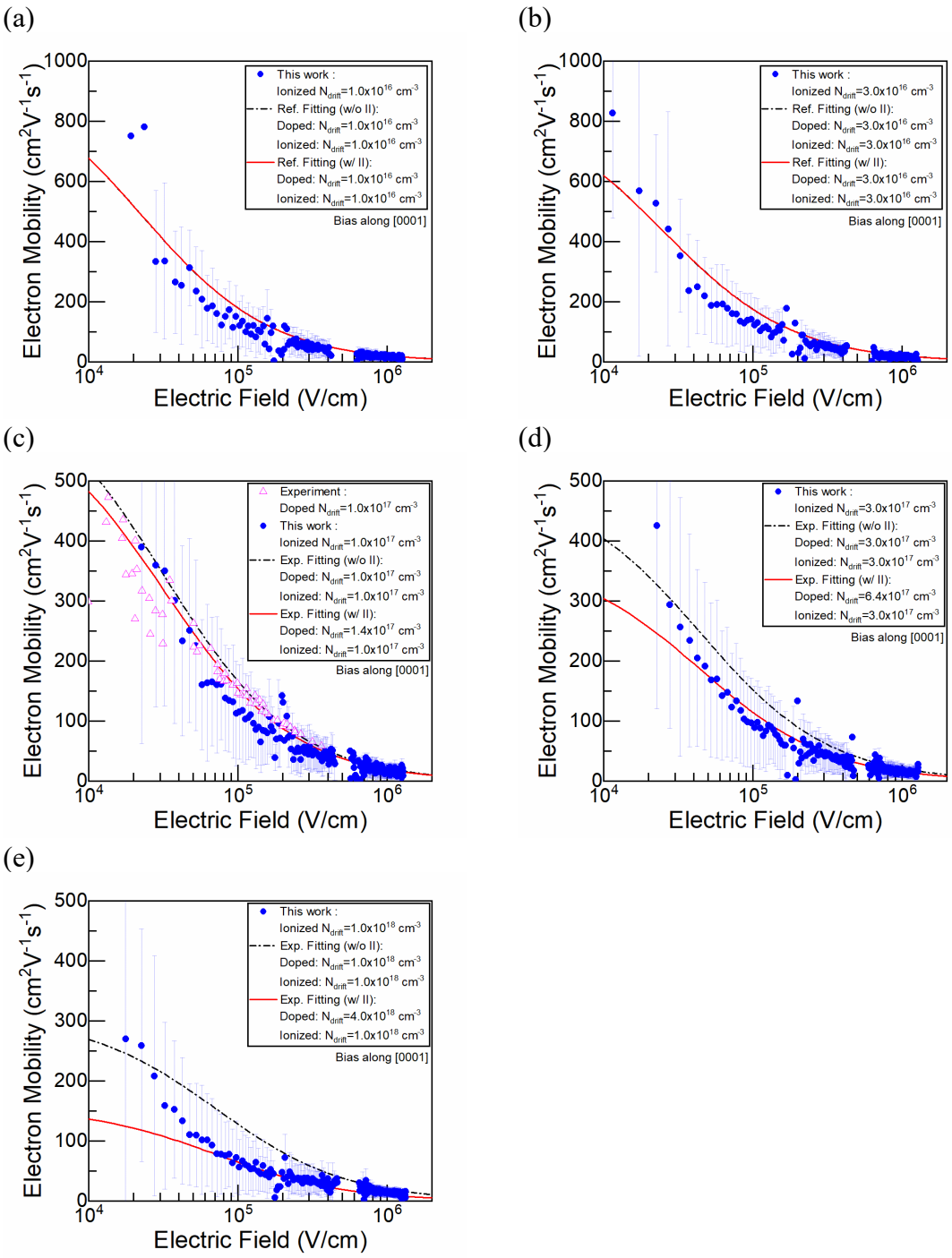

Figure 5.21 Electron mobility and averaged distributions of electron mobility vs. electric field for five different doping concentrations along [0001] direction in this work (dots). Triangles denote the experimental data from Ref. [41]. The dashed line indicates the model without considering the effect of incomplete ionization. The solid line represents the model with incomplete ionization(a) $N_d=1\times10^{16}$ cm^{-3} (b) $N_d=3\times10^{16}$ cm^{-3} (c) $N_d=1\times10^{17}$ cm^{-3} (d) $N_d=3\times10^{17}$ cm^{-3} (e) $N_d=1\times10^{18}$ cm^{-3}.

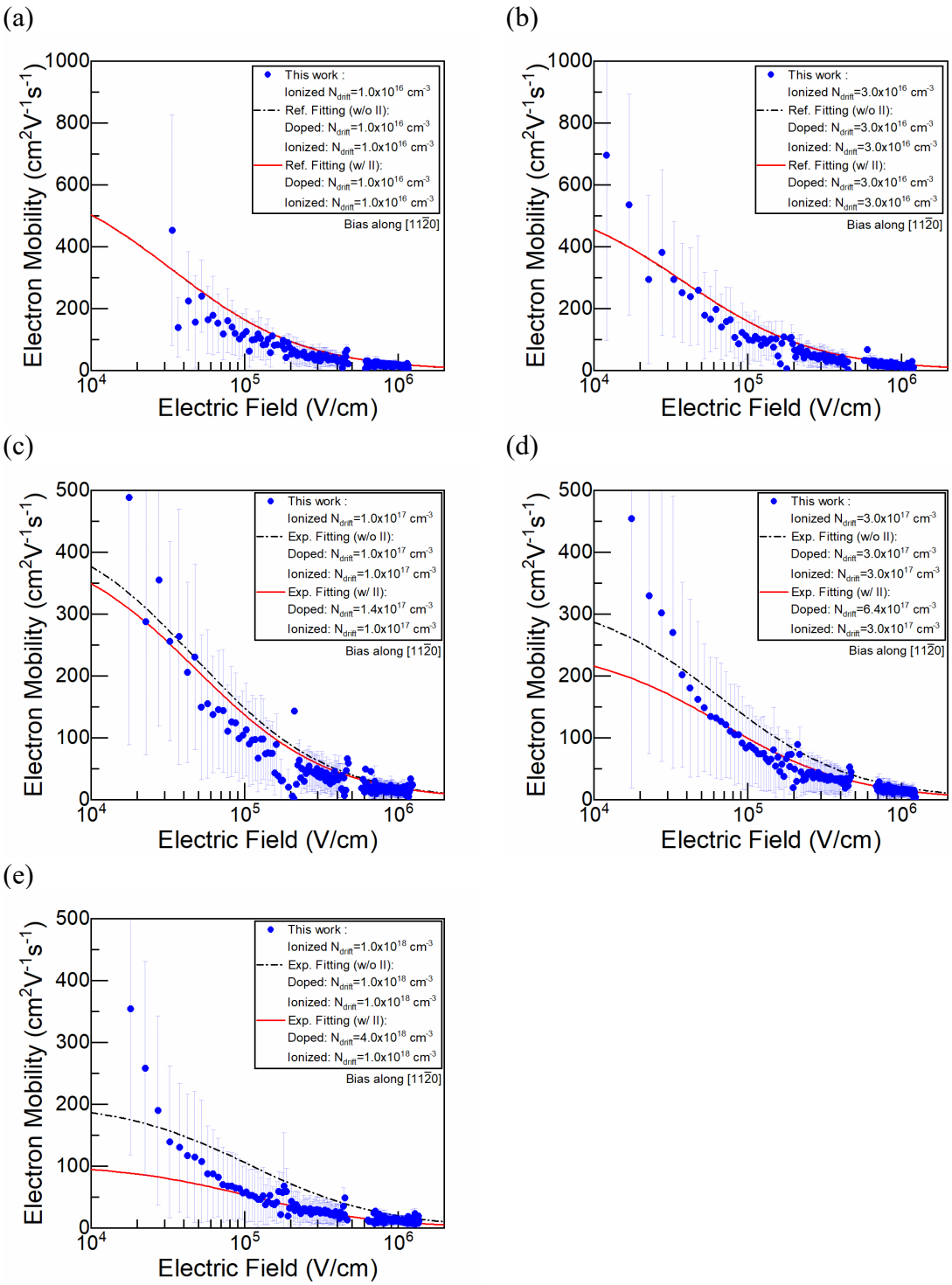

Figure 5.22 Electron mobility and averaged distributions of electron mobility vs. electric field for five different doping concentrations along [11-20] direction in this work (dots). The dashed line indicates the model without considering the effect of incomplete ionization. The solid line represents the model with incomplete ionization. (a) $N_d=1\times10^{16}$ cm^{-3} (b) $N_d=3\times10^{16}$ cm^{-3} (c) $N_d=1\times10^{17}$ cm^{-3} (d) $N_d=3\times10^{17}$ cm^{-3} (e) $N_d=1\times10^{18}$ cm^{-3}.

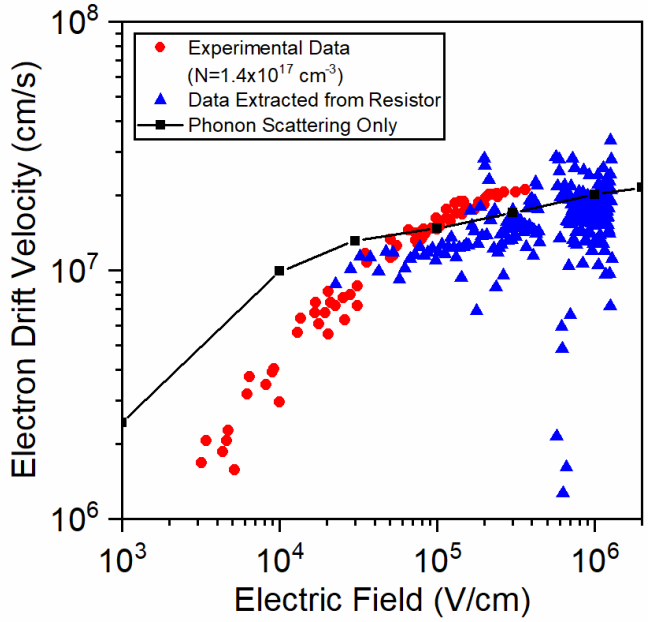

Figure 5.23 Comparison of the experimental electron drift velocity data, data extracted from resistor, and phonon-limited electron drift velocity.

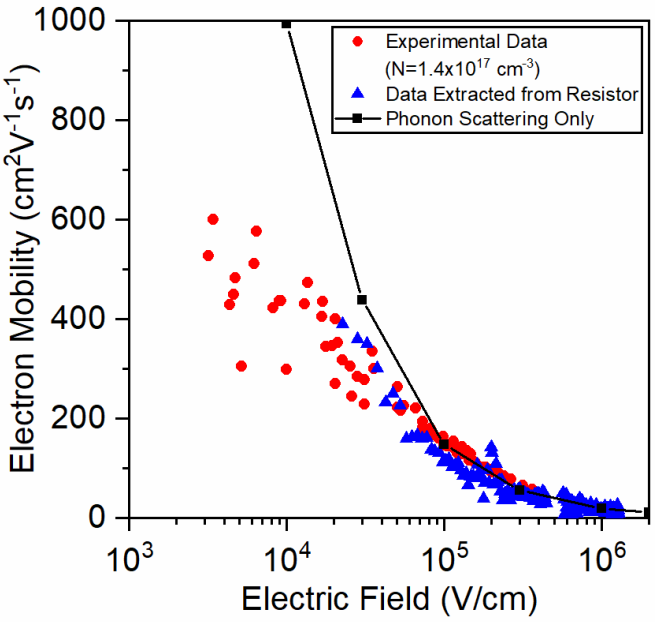

Figure 5.24 Comparison of experimental electron mobility data, data extracted from resistor, and phonon-limited mobility.

5.2.4 Average electron velocity and energy along the device

Figure 5.25 shows the profile of sample-averaged electron velocity along the device with bias along [0001] direction. In this case, the electron velocity is averaged over 20 samples to get a smoother plot. Figure 5.26 is the sample-averaged electron energy profile along the device. The electron energy at both sides of the device are excluded. The average energy in the drift region at bias=30 V is 2.04 kT (T=300 K).

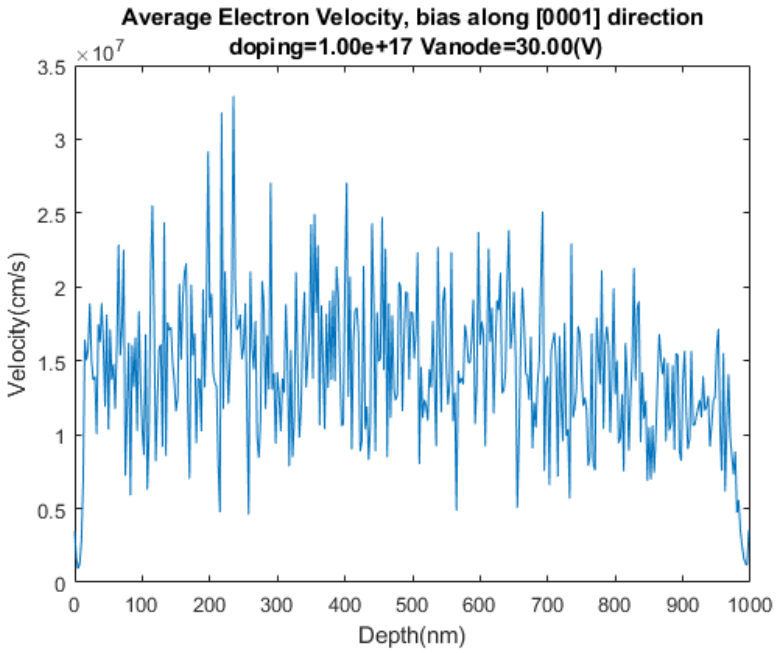

Figure 5.25 Sample-averaged electron velocity along the device of 20 samples.

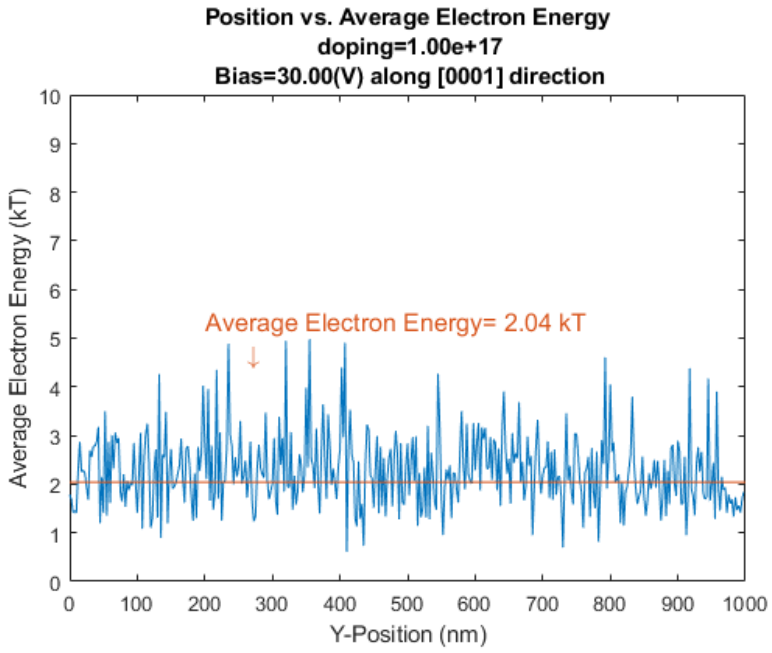

Figure 5.26 Sample-averaged electron energy along the device of 20 samples. The average electron energy in the drift region is about 2.04 kT at bias=30 V.

CHAPTER 6

DEVICE SIMULATION – VDMOS

6.1 Introduction of VDMOS

Metal–oxide–semiconductor field-effect transistor (MOSFET) is the most popular device in electronic systems, from minuscule integrated circuits (IC) to gigantic power generators. It often acts as a switch or an amplifier. The regular MOSFET features planar structure since it is easier to fabricate in the Si process. However, for the power electronic applications, users need a MOSFET which has a large current and a high breakdown voltage. It needs a very thick drift region to support the breakdown voltage, whereas, this also indicates a waste of usable wafer area. Thus, vertical devices are more preferable compared to the planar devices, because the thick drift region is perpendicular to the wafer face and costs no extra space on the wafer surface.

A special form of power MOSFET widely used is the vertical double-diffused MOSFET (VDMOS). It benefits from the vertical structure and the low-on resistance of DMOS. Figure 6.1 shows the typical structure of VDMOS. The epitaxial drift region is n-type to utilize high electron mobility. The p well is formed by diffusion or ion implantation process. The p base region acts as the stopper layer to prevent latch-up of the parasitic bipolar junction transistor (BJT). Next, the n^+ source is obtained by diffusion or ion implantation process, hence the name double-diffused. The channel is formed between the n^+ source and the n^- drift region beneath the oxide. The on-state current path is also indicated in Figure 6.1. When the gate is turned off, the channel is cut off. As a

result, the current cannot be conducted, and the device is turned off. The equivalent on-state resistances are also shown in Figure 6.1. R_{Source} and R_{Drain} are the source/drain resistance, including the resistance of the n^+ well, the contact resistance and the package resistance. $R_{Channel}$ is the channel resistance, which is determined by the gate voltage and the surface roughness scattering. R_{Access} is the access resistance, which represents the resistance of the region covered by the gate electrode. R_{JFET} is the resistance of the parasitic junction gate field-effect transistor (JFET), which contributes to the reduced effective area for the current flow because of the extension of the p well under biasing. R_{Drift} is the resistance of the drift layer. For high-voltage VDMOS, the doping is low and the drift layer is thick, resulting in high resistance. The on-state resistance R_{DSon} can then be treated as the summation of these equivalent resistances.

In this chapter, simulation results are presented for various types of 3D VDMOS devices. The in-house full-band Monte Carlo (FBEMC) device simulation tool is used for this analysis. In addition to the models described and used for obtaining the results presented in the previous chapter, surface roughness scattering at the Oxide/SiC interface must be considered as well. In the following simulations, it is assumed that the electrons have 50% chance of specular reflection and 50% chance of diffusive reflection at the Oxide/SiC interface in the channel.

The default device structure of the VDMOS that has been simulated in this work has the following parameters. The width of the device (*into the paper*) is only 20 nm to reduce calculation time. The device consists of a thin (40 nm) n^+ substrate layer, on top of

which is grown 1.46 μm of n^- drift region. The doping of the n^- drift layer is $5 \times 10^{16}\ cm^{-3}$. The p well is composed of two parts. The p^- region provides low threshold voltage V_{th} and has doping of $1 \times 10^{17}\ cm^{-3}$; on the other hand, the p region acts as a stopper layer to prevent latch-up, and has higher doping of $5 \times 10^{17}\ cm^{-3}$. The channel length is 0.5 μm (if not mentioned elsewhere) and the oxide thickness t_{oxide} is 0.1 μm. In addition, the doping densities of the n^+ source and drain regions are set to $1 \times 10^{18}\ cm^{-3}$ to ensure good ohmic contacts. The work function of the gate contact is set to 4.3 eV. The source contact implemented here has two parts (sections). One section is used for grounding the p^- well; the other one is used for the current path on the top of the n^+ source region. Uniform meshing is used in the simulation of the VDMOS to simplify the calculation. Since this is not a symmetric structure, the x-axis (channel) is discretized into a finer size to have more accurate results.

Impact ionization is neglected in this thesis. Also, the subband-to-subband tunneling, or the band crossing [44]–[46] has not been included since the device is not operated under extremely high bias conditions in these simulations. These two effects will be implemented in future work where we will study the breakdown behavior, and where they will definitely play important roles.

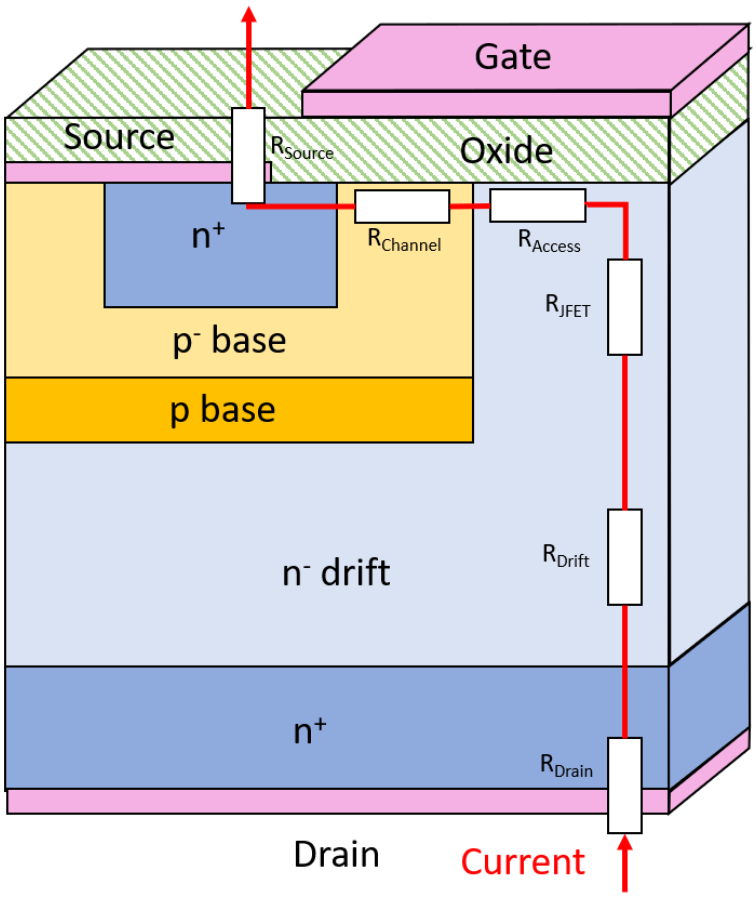

Figure 6.1 Typical structure of a vertical double-diffused MOSFET (VDMOS). The arrows indicate the current path under turn-on operation.

6.2 Electrical Profile Distributions

To validate the FBEMC device simulator, the electron density and the potential profile results of V_G=40 V and V_D=20 V are compared to the results from Silvaco Atlas as shown in Figure 6.2 and Figure 6.3, respectively. The profile results match well and are, thus, acceptable. Another set of results of higher V_D=300 V are also shown in Figure 6.4 and Figure 6.5. In this set, the results from the FBEMC simulator and Silvaco Atlas are different, which shows the discrepancy at high electric field, and thus, affirming the

necessity of full-band analysis at such condition. The cutline profiles of potential and electric field along the channel when V_G=20 V and V_G=40 V is applied on the gate electrode, are illustrated in Figure 6.6 and Figure 6.7, respectively. The cutline profiles of electron velocity are shown in Figure 6.8 and Figure 6.9. Figure 6.8 represents the velocity component parallel to the channel direction, denoted as $v_{channel}$, whereas Figure 6.9 depicts the magnitude of the velocity. The cutline profiles of the electron energy are shown in Figure 6.10. The data shown in Figure 6.8, Figure 6.9 and Figure 6.10 are smoothed by using the Savitzky-Golay filter [47]. By comparing the results shown in these figures, there are some noteworthy features to be discussed. (1) The channel velocity $v_{channel}$ for V_G=20 V is slightly larger than that for the case when V_G=40 V. It conforms with the presence of surface roughness scattering model, in which the surface roughness mobility is inversely proportional to the square of the transverse electric field [48]. (2) The magnitude of the velocity has different trend when compared to $v_{channel}$ in the channel region. The velocity $v_{channel}$ is higher at the end of channel at the drain side. On the other hand, the maximum of the magnitude of the velocity is at the source side. That is because the magnitude of the velocity also has the velocity component transverse to the channel direction. At the source side of the channel, the potential is nearly grounded and the transverse electric field is at its maximum, thus the magnitude of the velocity does not merely go with $v_{channel}$, which is positively correlated with the electric field shown in Figure 6.7. (3) The electron energy is correlated with the magnitude of velocity. Also, it is observed that the electron energy in the channel region is almost constant for V_G=40 V, which is attributed to the importance of surface roughness scattering.

(a) (b)

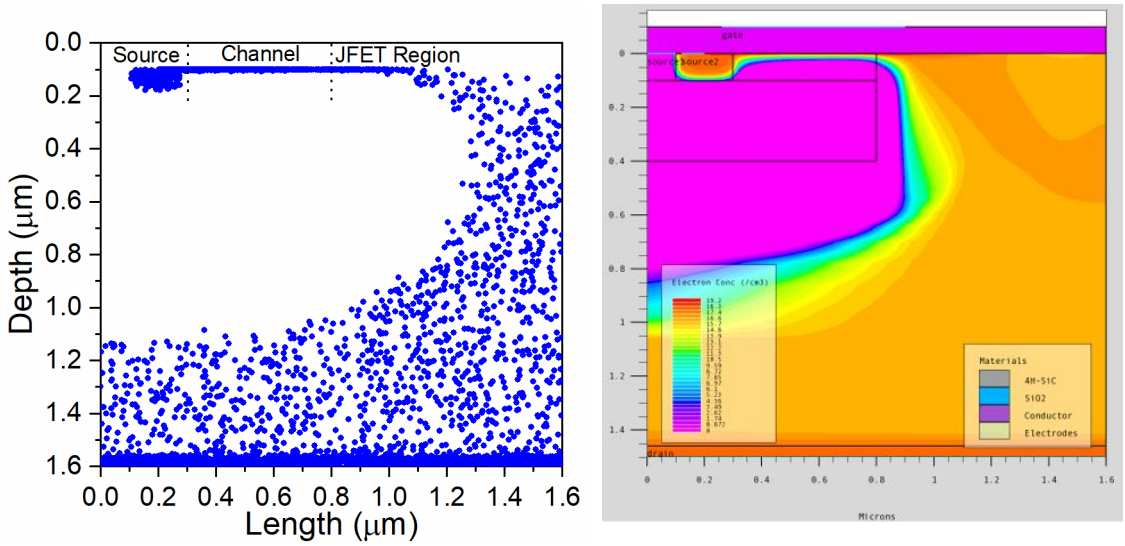

Figure 6.2 Electron distribution for V_G =40 V and V_D=20 V. (a) From the FBEMC device simulator (this work). (b) From Silvaco Atlas.

(a) (b)

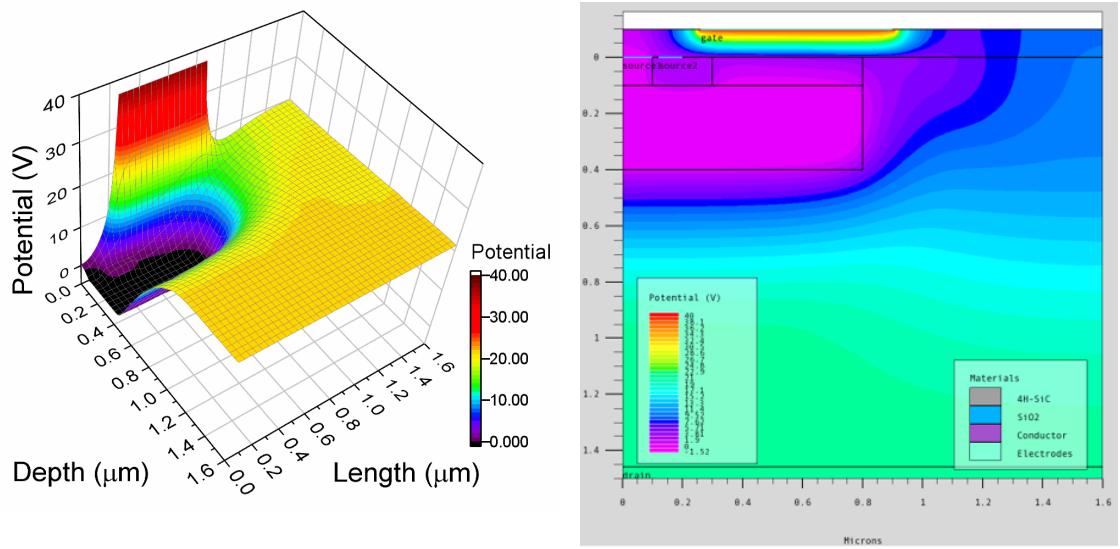

Figure 6.3 Potential distribution for V_G =40 V and V_D=20 V. (a) From the FBEMC device simulator (this work). (b) From Silvaco Atlas.

(a) (b)

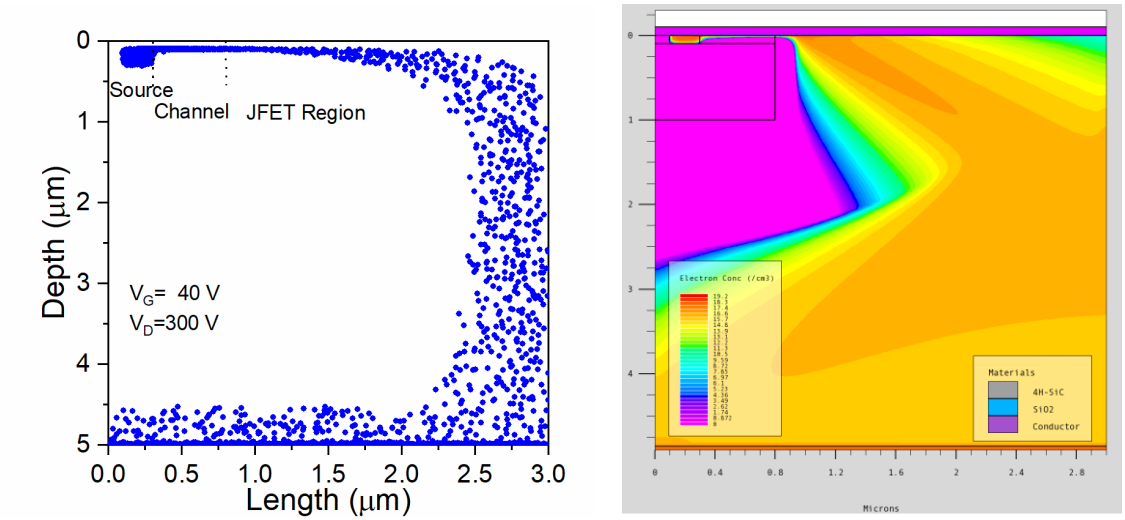

Figure 6.4 Electron distribution for V_G =40 V and V_D=300 V. (a) From the FBEMC device simulator (this work). (b) From Silvaco Atlas.

(a) (b)

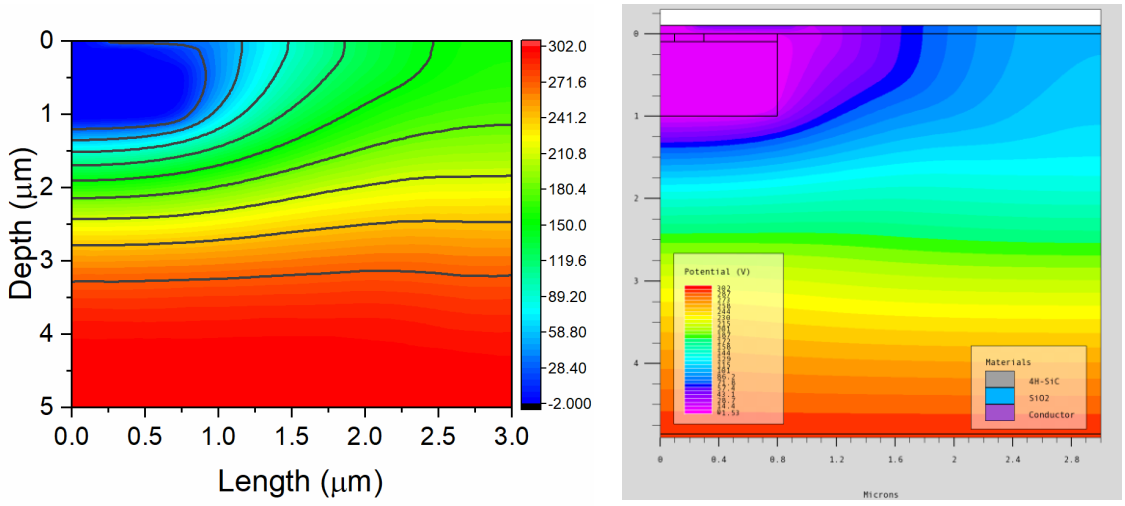

Figure 6.5 Potential distribution for V_G =40 V and V_D=300 V. (a) From the FBEMC device simulator (this work). (b) From Silvaco Atlas.

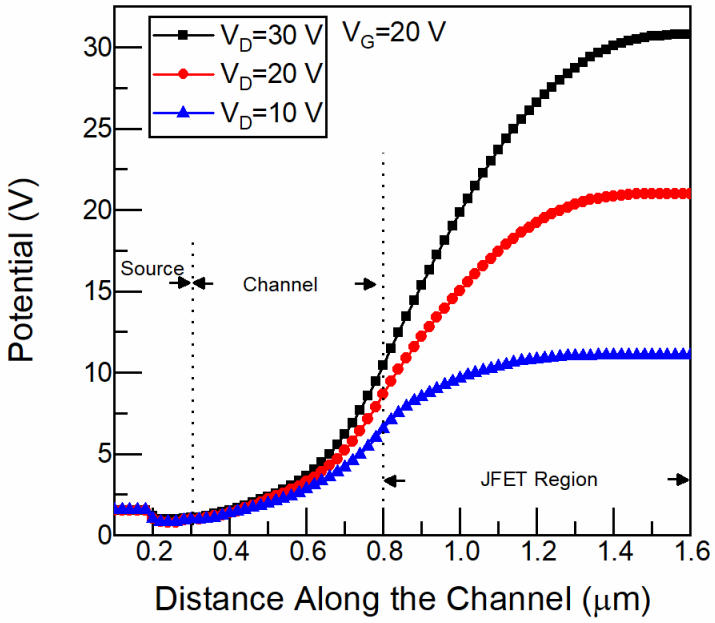

(a)

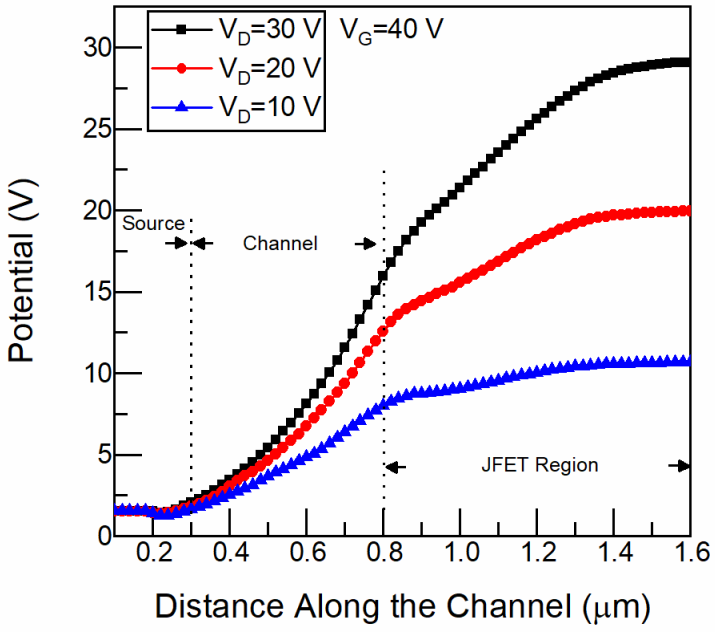

(b)

Figure 6.6 Cutline profiles of the potential along the channel: (a) V_G=20 V. (b) V_G=40 V.

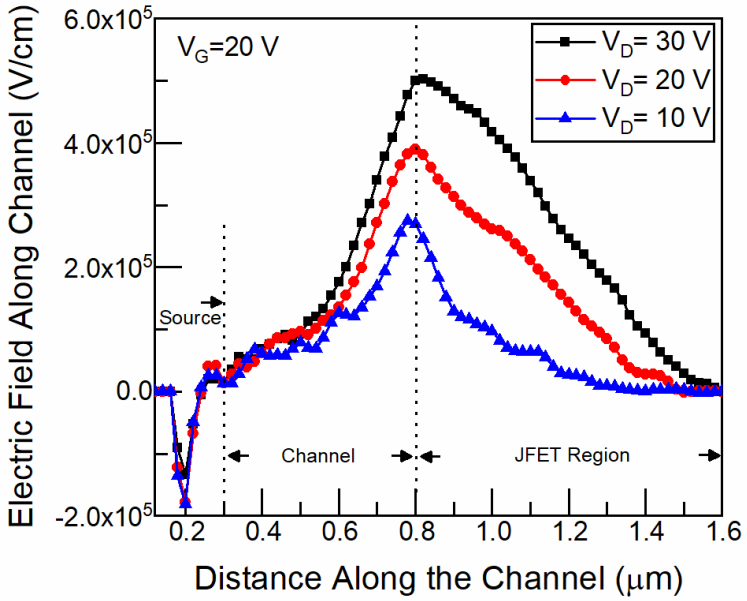

(a)

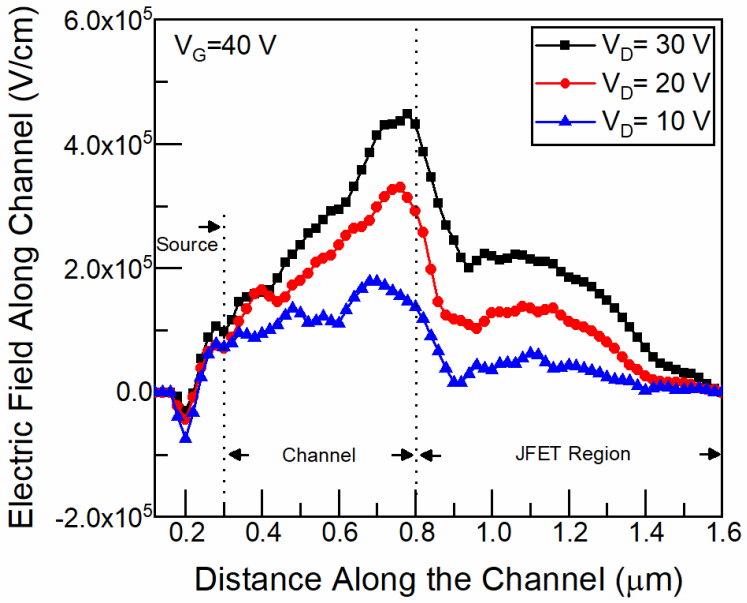

(b)

Figure 6.7 Cutline of the electric field along the channel: (a) V_G=20 V. (b) V_G=40 V.

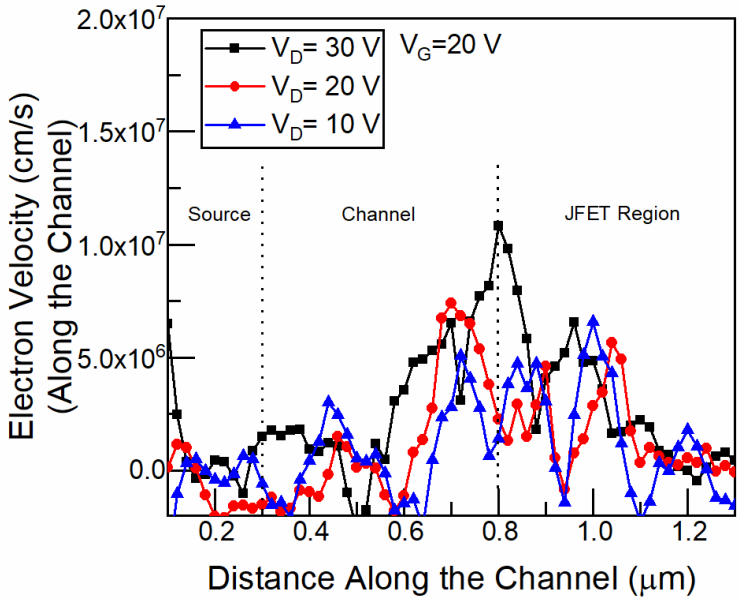

(a)

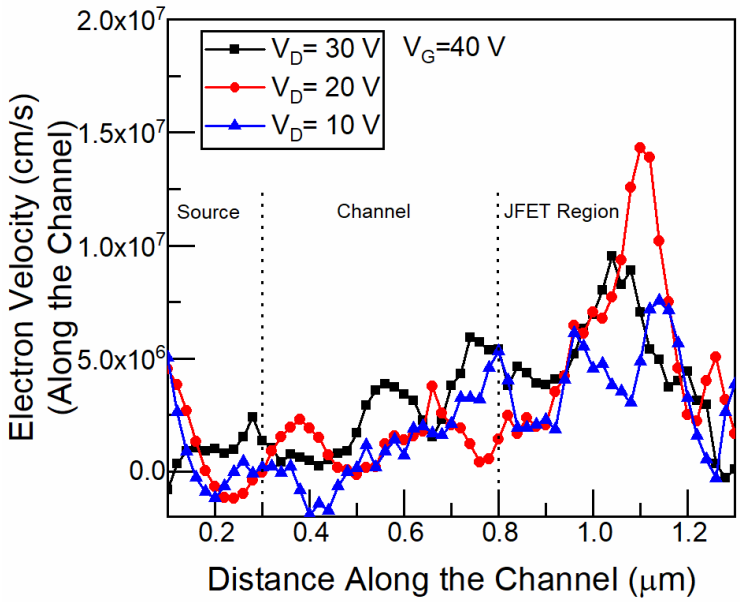

(b)

Figure 6.8 Cutline profiles of the electron velocity in the channel direction along the channel. (a) V_G=20 V. (b) V_G=40 V.

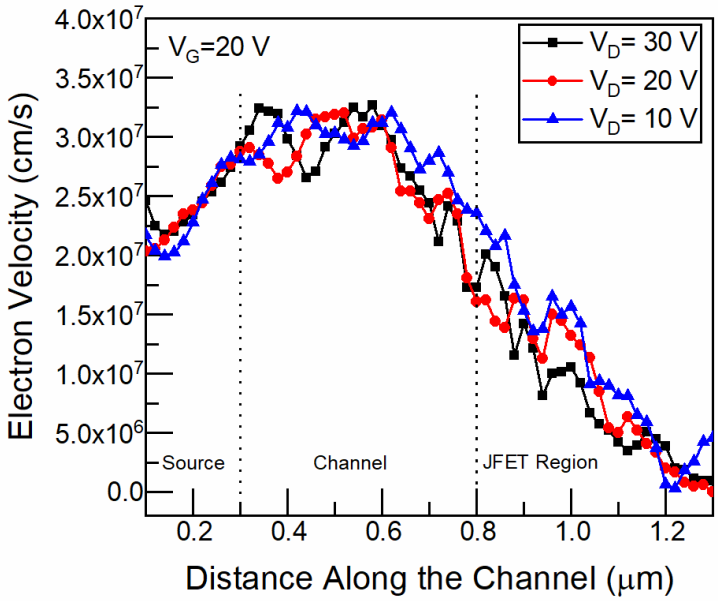

(a)

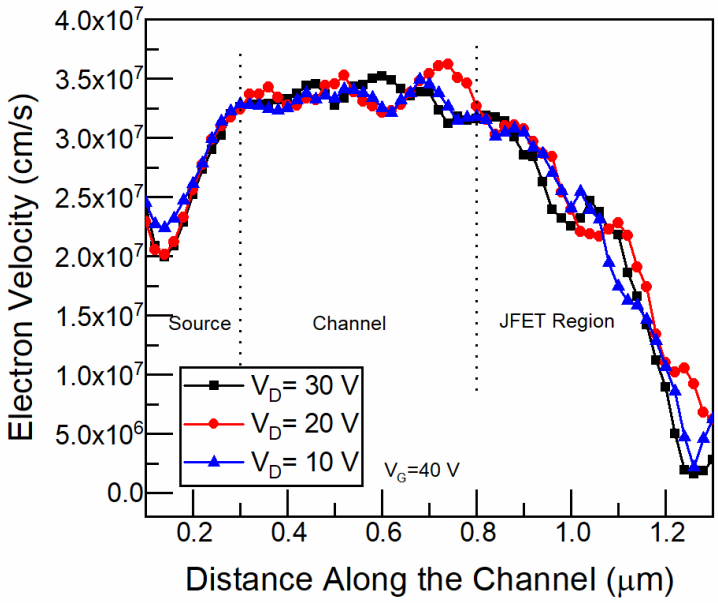

(b)

Figure 6.9 Cutline profiles of the magnitude of the electron velocity along the channel. (a) V_G=20 V. (b) V_G=40 V.

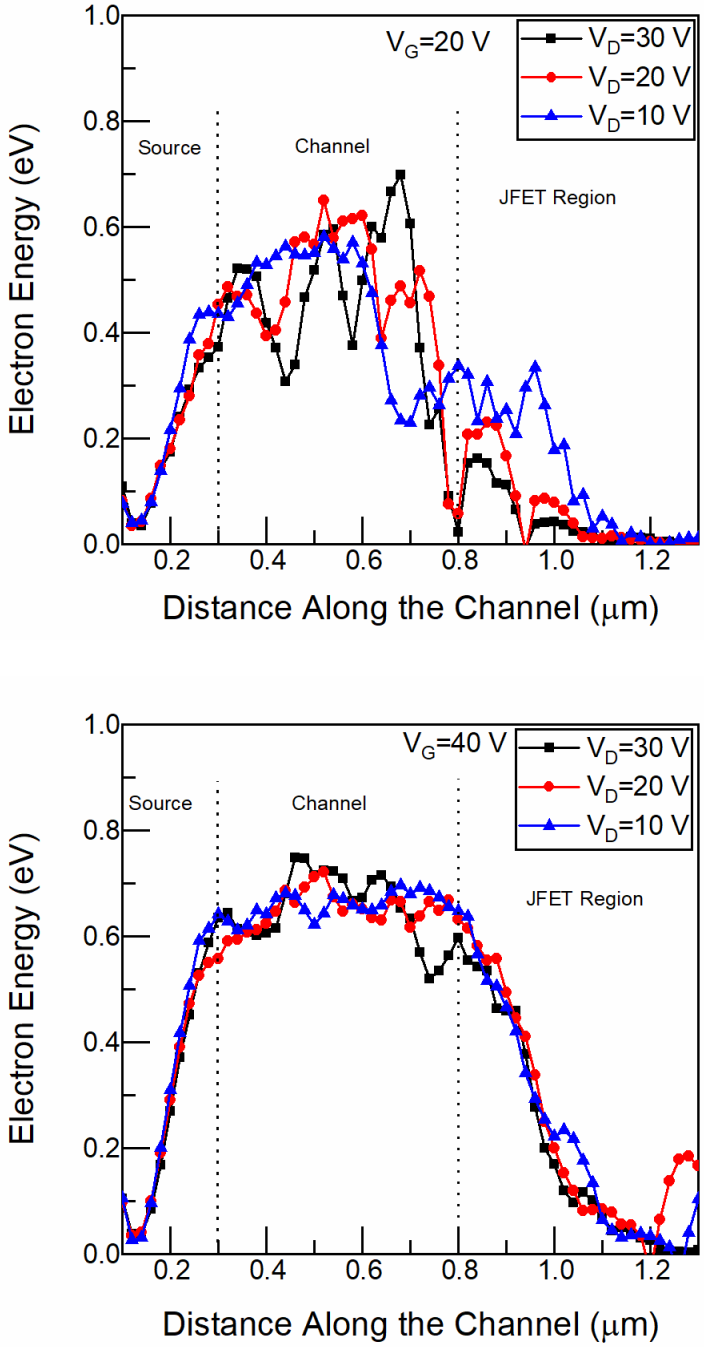

Figure 6.10 Cutline profiles of the electron energy along the channel. (a) V_G=20 V. (b) V_G=40 V.

6.3 I_D-V_G Transfer Characteristic

I_D-V_G transfer curve is an important characteristic when describing the operation of MOSFET device. To simulate the I_D-V_G curve, usually a small drain bias (< 0.1 V) is applied. Nevertheless, since this voltage level is too small to observe the outcomes in FBEMC device simulations, a voltage V_D=1 V is applied instead. The simulated device parameters are the same as those discussed in Section 6.2. Figure 6.11 shows the I_D-V_G transfer curve of the example VDMOS. Each point is taken as the average of five samples. The threshold voltage V_{th} in this example is about 12 V. It is observed that the drain current I_D gradually gets saturated as V_G > 20 V. This is a typical property of a VDMOS, which is attributed to the high resistivity of the thick and low-doping n^- drift layer, and the parasitic resistance of the JFET region.

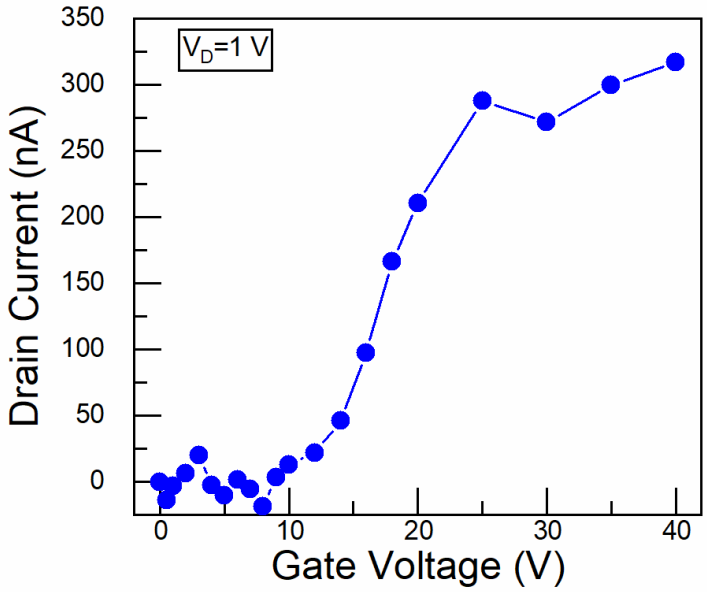

Figure 6.11 I_D-V_G transfer curve of the example VDMOS. V_D=1 V.

6.4 I_D-V_D Output Characteristic

Figure 6.12 depicts the output I_D-V_D characteristic under three gate voltages. The applied gate voltage is taken to be 20 V, 30 V and 40 V. The linear region of the VDMOS is not as obvious when compared to the regular planar MOSFET. In the regular planar MOSFET, the slope of the I_D-V_D curve in the linear region is proportional to V_G-V_{th}. However, this is not the case here because of the limitation of the high series resistances of the drift region and the JFET. Besides, due to the voltage drop across the resistances, the actual V_D needed to drive the top channel part is less than the drain voltage V_D applied on the electrode. The downward bending of the curves also indicates the presence of the high-resistance drift region. Furthermore, after carriers pass the channel, they have to change their direction of motion towards the drain. But, since the gate contact is opposite to the drain contact, the increased V_G results in reduced electron velocity when moving toward drain side and, therefore, leads to lower drain current.

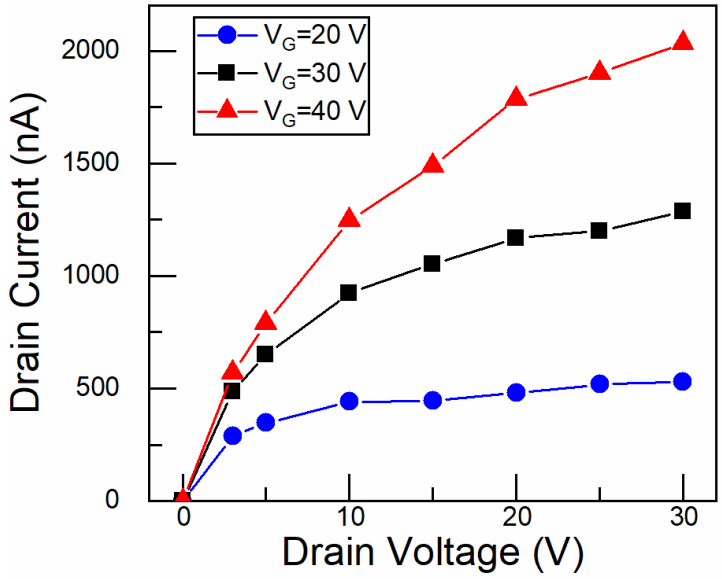

Figure 6.12 I_D-V_D output characteristics of the example VDMOS. The channel length is 0.5 μm.

6.5 Channel Length Dependence

Two channel lengths have been investigated in this study. One is the default one (0.5 μm) and the second channel length is taken to be 0.2 μm. The reason why the channel length is not set to an even smaller value is to prevent the latch-up of the parasitic BJT and the possibility of punch-through. The I_D-V_D curves of the device with channel length $L_{channel}$=0.2 μm are depicted in Figure 6.13. Comparing these results to the ones presented in Figure 6.12, it is observed that the curves shown in Figure 6.13 keep increasing with the increase of the drain voltage. Also, all three curves feature the same slope at high drain voltages. This phenomenon implies that the channel resistance is not dominating anymore. In this case, current is limited by the other resistance components.

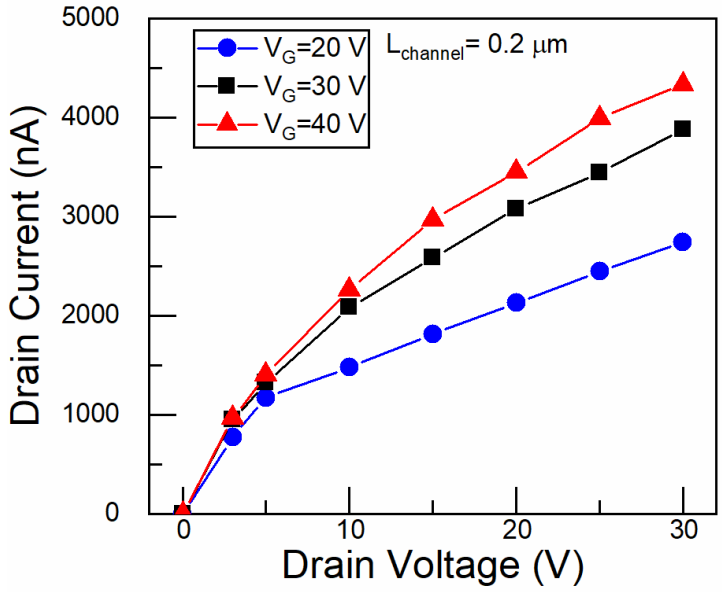

Figure 6.13 I_D-V_D output characteristics of example VDMOS.
The channel length is 0.2 μm.

6.6 Temperature Dependence

An obvious advantage of using 4H-SiC is the capability of working under high-temperature environment. Note that the intrinsic carrier density increases exponentially with temperature and is inversely exponentially dependent upon the bandgap. SiC, thanks to its wide bandgap, has intrinsic carrier density much lower when compared to Si or GaAs materials. It is so low that even at high temperature, the concentration of intrinsic carriers is still far lower than of the extrinsic carriers. On the other hand, the concentration of intrinsic carriers in Si or GaAs at high temperature is higher than that of the extrinsic carriers. This results in the malfunction of the device and could damage partially or entirely the system. That is why the temperature dependence is an important characteristic. Figure 6.14 shows the temperature dependence. As expected, the currents

drop when the temperature is raised to 350 K from nominal 300 K. The degradation of the current is not only attributed to the temperature-related term in the Poisson's equation, but also to the degradation of the mobility resulted from the phonon scattering mechanisms. The same structure is also simulated in Silvaco Atlas. Since it is hard to match our surface-roughness scattering model with the one used in Silvaco, in Figure 6.15 we display the Silvaco simulation results without considering surface roughness scattering. Although the current values are higher when compared to our simulation results, the I_D-V_D profiles are very similar, which validates the in-house FBEMC simulator.

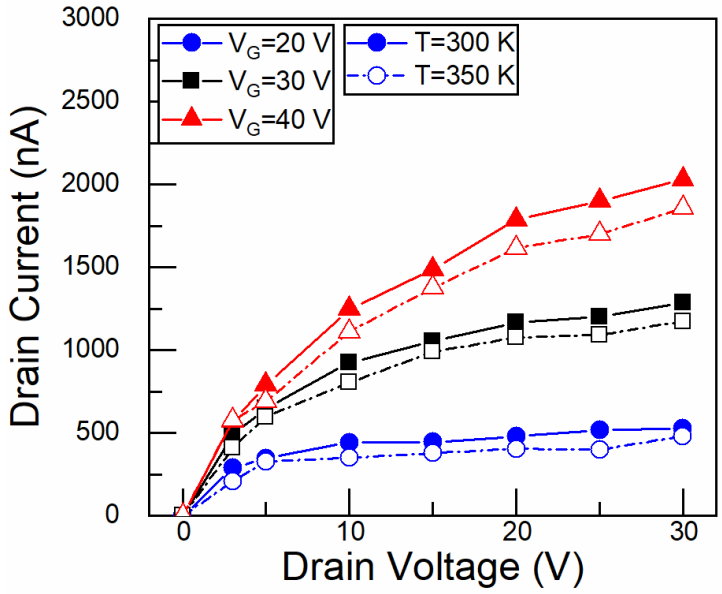

Figure 6.14 I_D-V_D output characteristics of the example VDMOS. The channel length is 0.5 μm. Temperature is 300K and 350K.

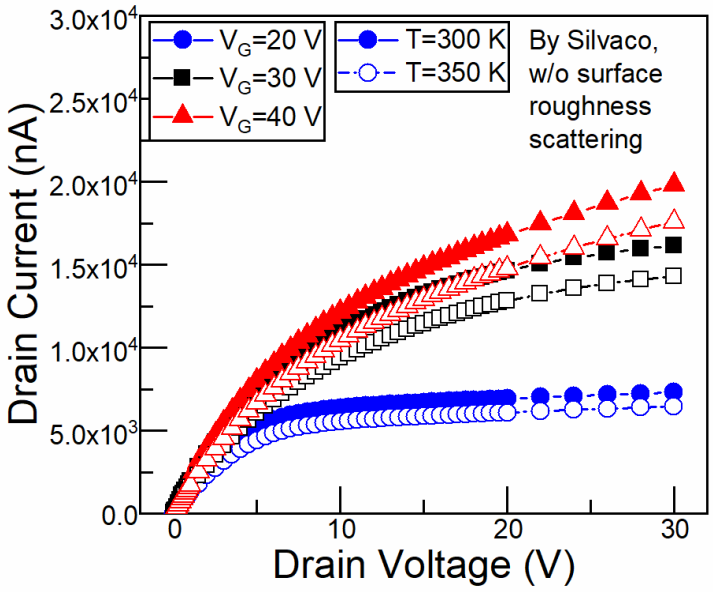

Figure 6.15 I_D-V_D output characteristics of example VDMOS simulated with Silvaco without considering surface-roughness scattering.

6.7 Transient Behavior

The FBEMC device simulator is also capable of simulating transient response. Because of the built-in nature, once the system reaches steady-state all the changes that follow the change in the biasing conditions depict real physical behavior. For example, one can let the VDMOS to be turned on at the beginning of the simulation. After reaching the steady-state, the gate is switched off. Then, the electrons accumulated at the inversion layer must be ejected to reach the off-state condition. The ejected electrons are detected at the electrodes as shown in Figure 6.16. In this simulation the channel length of the VDMOS is decreased to 0.2 μm from 0.5 μm, and the thickness of the n^- drift layer is decreased to 1.6 μm from 1.4 μm to have noticeable change in the results. The blue and red lines are the cumulative charge number exiting drain and source, respectively. The

green line depicts the applied gate voltage. Here, the gate is switched from 40 V to 0 V and from 0 V to 40 V using three different dV_g/dt values: $dV_g/dt = 10\ V/ps$, $dV_g/dt = 100\ V/ps$ and $dV_g/dt = 1000\ V/ps$.

Since the derivative of the change of charge is the current, by using the Savitzky-Golay filter, one can get the transient responses shown in Figure 6.17, Figure 6.18 and Figure 6.19. In these figures, both V_D= 10 V and V_D= 20 V are simulated. The blue and red lines are the drain and source currents, respectively. The green line is the applied gate voltage. Because the currents at on-state (time < 4 ps) are strongly affected by the smoothness of the cumulative charge number, two auxiliary grey values derived from fitting are annotated in these figures as well. The drain currents I_D for V_D=10 V in the three figures are about 2200 nA and they increase to 3150 nA for V_D=20 V. There are some noteworthy features that can be observed from the results presented in these three figures: (1) No matter whether V_D=10 V or V_D=20 V, the turn-off time for both drain (I_D) current values is about 12 ps. For the source current (I_S) we observe that for both cases the turn-off time is about 7 ps, even for the case of V_D=20 V that leads to larger I_D. This trend is also independent upon the value of dV_g/dt. (2) Though the turn-off time for V_D=10 V or V_D=20 V are almost the same, the peak value of I_D and I_S depend on the dV_g/dt. The larger the dV_g/dt is, the higher the peak value is. Note however that the peak values of the source and drain currents for $dV_g/dt = 100\ V/ps$ and $dV_g/dt = 1000\ V/ps$ are almost the same. (3) According to (1), despite the fact that the switching time of the gate is just 0.04~4 ps, both I_D and I_S need longer time to get stable. This delay

also needs to be taken into consideration while operating a high-frequency switching. (4). The I_D and I_S skyrocket dramatically compared to their DC on-state current values during the switching operations. The source current I_S is much larger than the drain current I_D because the source electrode is closer to the inversion layer where electrons need to be ejected. (5) The turn-on operation has a larger and narrower pulse than the turn-off operation. But the turn-on time has a longer tail after the pulse before reaching the new steady-state condition.

Apparently, the property of reverse recovery currents is very crucial for the users, since such large current may damage the system if it overwhelms the protection design. By the aid of the in-house FBEMC device simulator, one can obtain better understanding on the physical operation of the device during transients. This knowledge can be used for design of better and more durable VDMOS devices.

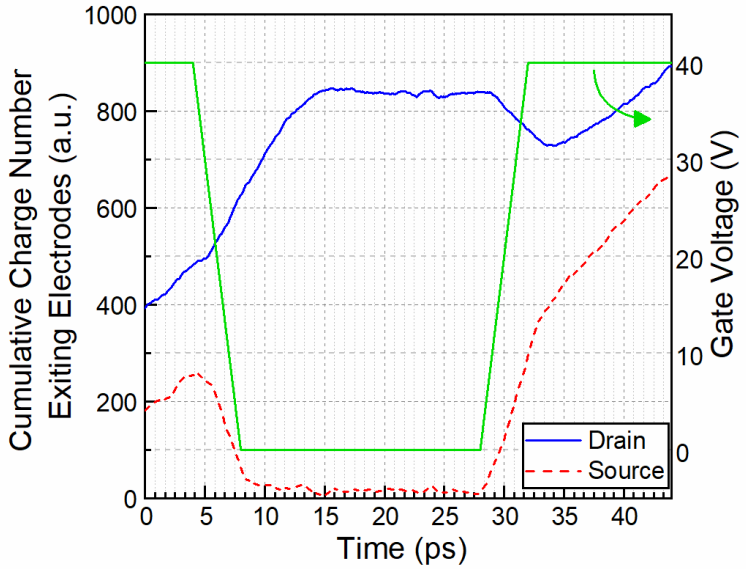

Figure 6.16 Cumulative charge number exiting electrodes along time. The gate voltage is switched from 40 V to 0 V and from 0 V to 40 V in 4 ps time interval. V_D=20 V in these simulations.

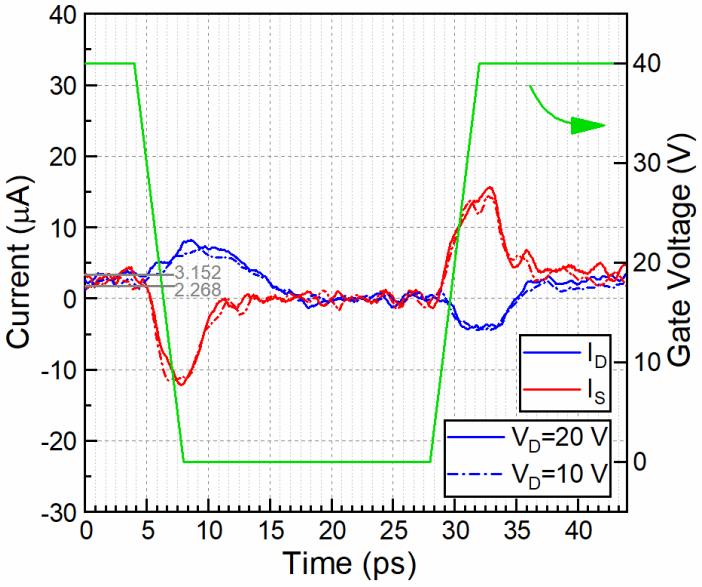

Figure 6.17 Switching transient response of the example VDMOS. The gate voltage is switched from 40 V to 0 V and from 0 V to 40 V in 4 ps time interval. Results for V_D=10 V and for V_D = 20V are simulated here.

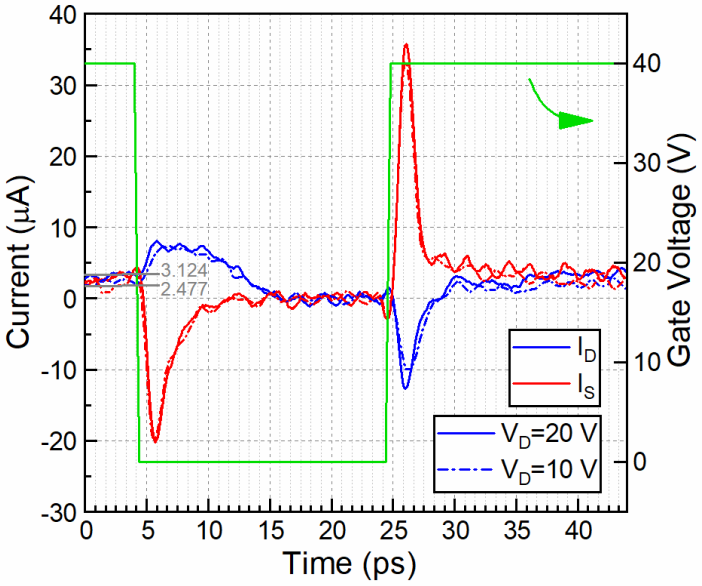

Figure 6.18 Switching transient response of the example VDMOS. The gate voltage is switched from 40 V to 0 V and from 0 V to 40 V in 0.4 ps time interval. V_D=10 V and V_D = 20V are used in these simulations.

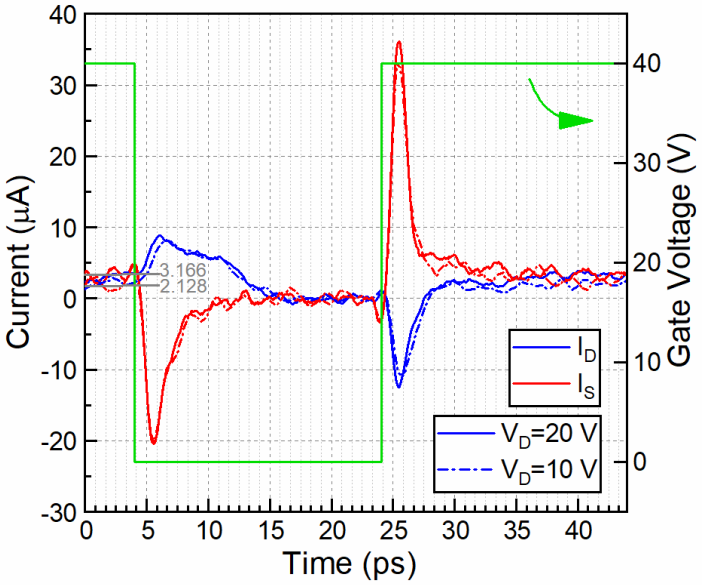

Figure 6.19 Switching transient response of the example VDMOS. The gate voltage is switched from 40 V to 0 V and from 0 V to 40 V in 0.04 ps time interval. V_D=10 V and V_D = 20V is used in these simulations.

CHAPTER 7

CONCLUSIONS AND FUTURE WORK

To model the properties of 4H-SiC material and the characteristics of the devices made of it accurately, a full-band Monte Carlo simulator is needed. The band structure of 4H-SiC was obtained by the empirical pseudopotential method (EPM) in this work. The indirect band gap calculated is 3.2568 eV which is quite close to the commonly known value of 3.26eV. The scattering mechanisms, including acoustic, non-polar optical and polar optical phonons, are calculated using the previously calculated band structure. Because the simulator is particle-based already, the Coulomb force can be coupled with the particle-particle-particle-mesh method (P^3M) easily. A 3D resistor made of 4H-SiC has been simulated successfully in the micrometer-level by using this in-house full-band Monte Carlo device simulator.

The electrical characteristics of the resistors with different doping concentration has been simulated through a 3D resistor. Four bias voltages are used to cover a range of electric fields. The impact of discrete dopants can be studied using this particle-based device simulator, and it is more prominent for lower doping concentration case. Also, an anisotropy of mobility along different crystal orientation is observed. The ratio between [0001] and $[11\bar{2}0]$ direction is found to be between 1.25-1.75 in this simulation work. More importantly, the distribution of electron velocity and mobility with varying electric field have been also calculated. The statistics of the distributions match the commonly

used models precisely if one also considers the incomplete ionization effect.

Next, a 3D VDMOS is simulated. The electrical profiles, including the electron distribution and potential, of a 3D VDMOS have been simulated. In addition, the I_D-V_G and the I_D-V_D curves are presented, proving that this device simulator is capable of producing reliable steady-state simulations. More importantly, this FBEMC device simulator also demonstrates its capability in simulating the transient response. Examples of switching-on and switching-off operation have been displayed. The reverse recovery currents during the switching are too large to ignore. Also, the switching frequency is limited by the switching time of I_D and I_S. All these aspects should be taken into consideration while designing the system.

With this simulator one can further explore transient behaviors of 4H-SiC which are crucial in modern applications. For example, CV simulations can be easily done. To do so, one just need to superimpose a signal, which is a small sinusoidal voltage, on the DC bias. By changing the electrode where the signal is applied, the capacitance between electrodes can be analyzed. Besides this, since either the donor or the acceptor activation energy of 4H-SiC are quite high compared to the most common one, Si, one must consider the response when applying a reverse bias pulse which is equal or smaller than the characteristic ionization time constant. As shown in Figure 7.1, it is expected that a dynamically enlarged extension of depletion region will be formed which may cause

response like dynamic punch-through resulting in unexpected damage during operation [49].

There are three major physics models that need to be integrated to have a more comprehensive simulation tool. The first one is the introduction of holes. Although only unipolar device operation is demonstrated in this work, minority carriers (which is hole here) are important for proper description of the impact ionization process. The impact ionization model is the second one to be introduced, because it relates to the breakdown characteristics of a device. With the aid of it, the simulator can do more precise breakdown analysis under high electric field. The last one is the implementation of band-crossing [44]–[46]. Note that some energies in different bands are very close. The carriers do have possibility to move to another band under high electric fields, so the electrons can move to even higher bands. Without this modification in the code, the electron energy is underestimated. Although this is not a serious issue at lower electric fields, it has to be addressed at higher electric fields near the breakdown point of operation of the device.

In summary, it is demonstrated in this work via comparison to experiments, that a successful, physically-based, full-band ensemble Monte Carlo device simulator for 4H-SiC was developed. The simulator provides one not only macro-scale properties, but also the micro-scale ones. The advantages of this tool lay the foundations for future simulation work on 4H-SiC high-power devices.

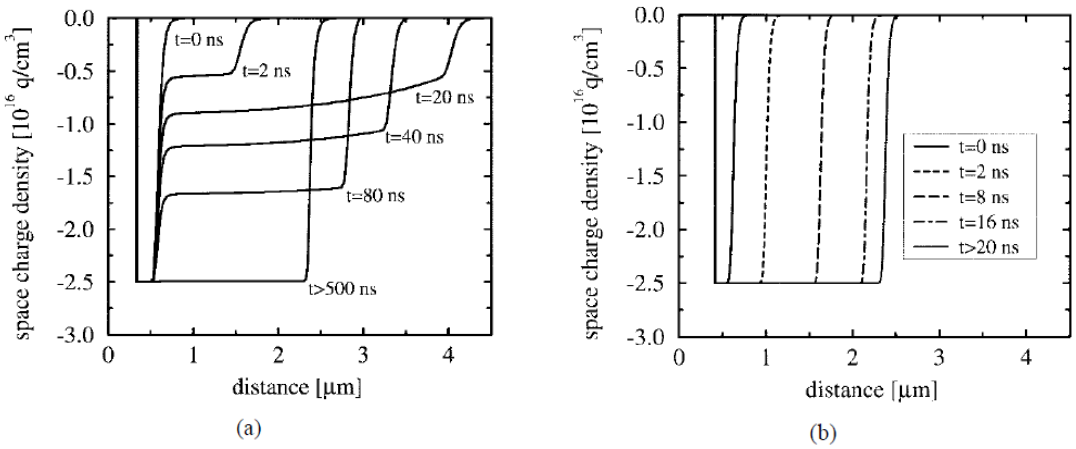

Figure 7.1 Transient evolution of the depletion region of a (a) lowly B-doped and (b) Al-doped region of a 6H–SiC pn-diode during a 100V/20ns ramp at 300 K [49].

REFERENCES

[1] H. Matsunami and T. Kimoto, “Step-controlled epitaxial growth of SiC: High quality homoepitaxy,” *Mater. Sci. Eng. R*, vol. 20, no. 3, pp. 125–166, 1997.

[2] M. Bhatnagar and B. J. Baliga, “Power Devices,” vol. 40, no. 3, 1993.

[3] R. Pérez, D. Tournier, A. Pérez-Tomas, P. Godignon, N. Mestres, and J. Millán, “Planar edge termination design and technology considerations for 1.7-kV 4H-SiC PiN diodes,” *IEEE Trans. Electron Devices*, vol. 52, no. 10, pp. 2309–2316, 2005.

[4] G. R. Fisher and P. Barnes, “Towards a unified view of polytypism in silicon carbide,” *Philos. Mag.*, vol. 61, no. 2, pp. 217–236, 1990.

[5] H. Lee, “High Power Bipolar Junction Transistors in Silicon Carbide,” Royal Institute of Technology, 2005.

[6] Fischetti and Laux, “Monte Carlo analysis of electron transport in small semiconductor devices including band-structure and space-charge effects,” *Phys. Rev. B. Condens. Matter*, vol. 38, no. 14, p. 9721.

[7] K. Tsukioka, D. Vasileska, and D. K. Ferry, “An ensemble Monte Carlo study of high-field transport in $β$-SiC,” *Phys. B Phys. Condens. Matter*, vol. 185, no. 1–4, pp. 466–470, 1993.

[8] E. Bellotti, H. E. Nilsson, K. F. Brennan, and P. P. Ruden, “Ensemble Monte Carlo calculation of hole transport in bulk 3C-SiC,” *J. Appl. Phys.*, vol. 85, no. 6, pp. 3211–3217, 1999.

[9] H. E. Nilsson, U. Englund, M. Hjelm, E. Bellotti, and K. Brennan, “Full band Monte Carlo study of high field transport in cubic phase silicon carbide,” *J. Appl. Phys.*, vol. 93, no. 6, pp. 3389–3394, 2003.

[10] H.-E. Nilsson, M. Hjelm, C. Fröjdh, C. Persson, U. Sannemo, and C. S. Petersson, “Full band Monte Carlo simulation of electron transport in 6H-SiC,” *J. Appl. Phys.*, vol. 86, no. 2, pp. 965–973, 1999.

[11] H. Iwata, K. M. Itoh, and G. Pensl, “Theory of the anisotropy of the electron Hall mobility in n -type 4H– and 6H–SiC,” *J. Appl. Phys.*, vol. 88, no. 4, pp. 1956–1961, 2000.

[12] R. P. Joshi, “Monte Carlo calculations of the temperature- and field-dependent electron transport parameters for 4H-SiC,” *J. Appl. Phys.*, vol. 78, no. 9, pp. 5518–5521, 1995.

[13] H. Nilsson, U. Sannemo, and C. S. Petersson, “Monte Carlo simulation of electron transport in 4H–SiC using a two-band model with multiple minima,” *J. Appl. Phys.*, vol. 80, no. 6, pp. 3365–3369, 1996.

[14] M. Hjelm, H. E. Nilsson, A. Martinez, K. F. Brennan, and E. Bellotti, “Monte Carlo study of high-field carrier transport in 4H-SiC including band-to-band tunneling,” *J. Appl. Phys.*, vol. 93, no. 2, pp. 1099–1107, 2003.

[15] B. K. Ridley, “Reconciliation of the Conwell-Weisskopf and Brooks-Herring formulae for charged-impurity scattering in semiconductors: Third-body interference,” *J. Phys. C Solid State Phys.*, vol. 10, no. 10, pp. 1589–1593, 1977.

[16] A. Kovalchuk, J. Wozny, Z. Lisik, J. Podgorski, and P. Bugalski, “Ensemble Monte Carlo Simulation of 4H-SiC for Electrons Mobility Calculation,” *2018 XIV-th Int. Conf. Perspect. Technol. Methods MEMS Des.*, pp. 119–123, 2018.

[17] A. Akturk, N. Goldsman, S. Potbhare, and A. Lelis, “High field density-functional-theory based Monte Carlo: 4H -SiC impact ionization and velocity saturation,” *J. Appl. Phys.*, vol. 105, no. 3.

[18] J. Woźny *et al.*, “Monte Carlo Electron Transport Simulation of 4H-SiC using DFT Calculated Density of States,” in *Conference: International Conference on Scientific Computing (CSC’18)*, 2018, no. August.

[19] M. V. Fischetti, “Effect of the electron-plasmon interaction on the electron mobility in silicon,” *Phys. Rev. B. Condens. Matter*, vol. 44, no. 11, p. 5527, 1991.

[20] M. V Fischetti and S. E. Laux, “Monte Carlo study of electron transport in silicon inversion layers.,” *Phys. Rev. B. Condens. Matter*, vol. 48, no. 4, pp. 2244–2274, 1993.

[21] W. J. Gross, D. Vasileska, and D. K. Ferry, “3D simulations of ultra-small MOSFETs with real-space treatment of the electron-electron and electron-ion interactions,” *VLSI Des.*, vol. 10, no. 4, pp. 437–452, 2000.

[22] Synopsys, “Synopsys Sentaurus.” p. https://www.synopsys.com/silicon/tcad.html, 2020.

[23] Silvaco, “Silvaco.” p. https://www.silvaco.com/, 2020.

[24] M. L. Cohen and T. K. Bergstresser, “Band structures and pseudopotential form factors for fourteen semiconductors of the diamond and zinc-blende structures,” *Phys. Rev.*, vol. 141, no. 2, pp. 789–796, 1966.

[25] J. R. Chelikowsky and M. L. Cohen, “Nonlocal pseudopotential calculations for the electronic structure of eleven diamond and zinc-blende semiconductors,” *Phys. Rev. B*, vol. 14, no. 2, pp. 556–582, 1976.

[26] M. Cardona and F. H. Pollak, “Energy-Band Structure of Germanium and Silicon: The k·p Method,” *Phys. Rev.*, vol. 142, no. 2, pp. 530–543, Feb. 1966.

[27] R. Beresford, “Full-zone k·p method of band structure calculation for wurtzite semiconductors,” *J. Appl. Phys.*, vol. 95, no. 11, pp. 6216–6224, 2004.

[28] D. J. Chadi and M. L. Cohen, “Tight-binding calculations of the valence bands of diamond and zincblende crystals,” *Phys. Status Solidi*, vol. 68, no. 1, pp. 405–419, 1975.

[29] J. Jancu, R. Scholz, F. Beltram, and F. Bassani, “Empirical spds* tight-binding calculation for cubic semiconductors: General method and material parameters,” *Phys. Rev. B*, vol. 57, no. 11, pp. 6493–6507, 1998.

[30] H. Junginger and W. van Haeringen, “Energy Band Structures of Four Polytypes of Silicon Carbide Calculated with the Empirical Pseudopotential Method,” *Phys. status solidi*, vol. 37, no. 2, pp. 709–719, 1970.

[31] G. Pennington and N. Goldsman, “Empirical pseudopotential band structure of 3C, 4H, and 6H SiC using transferable semiempirical Si and C model potentials,” *Phys. Rev. B - Condens. Matter Mater. Phys.*, vol. 64, no. 4, pp. 1–10, 2001.

[32] S. M. Zubkova, L. N. Rusina, and E. V Smelyanskaya, “Temperature Dependence of the Band Structure of 3 C , 2 H , 4 H , and 6 H SiC Polytypes,” *Semiconductors*, vol. 37, no. 3, pp. 239–248, 2003.

[33] G. Ng, D. Vasileska, and D. K. Schroder, “Empirical pseudopotential band structure parameters of 4H-SiC using a genetic algorithm fitting routine,” *Superlattices Microstruct.*, vol. 49, no. 1, pp. 109–115, 2011.

[34] W. Setyawan and S. Curtarolo, “High-throughput electronic band structure calculations: Challenges and tools,” *Comput. Mater. Sci.*, vol. 49, no. 2, pp. 299–312, 2010.

[35] M. Lundstrom, *Fundamentals of carrier transport*, 2nd ed.. Cambridge, U.K. ; New York: Cambridge University Press, 2000.

[36] C. J. Wordelman and U. Ravaioli, “Integration of a particle-particle-particle-mesh algorithm with the ensemble Monte Carlo method for the simulation of ultra-small semiconductor devices,” *IEEE Trans. Electron Devices*, vol. 47, no. 2, pp. 410–416, 2000.

[37] R. W. Hockney and J. W. Eastwood, *Computer simulation using particles*. New York: McGraw-Hill International Book Co., 1981.

[38] W. J. Gross, D. Vasileska, and D. K. Ferry, "Ultrasmall MOSFETs: the importance of the full Coulomb interaction on device characteristics," *IEEE Trans. Electron Devices*, vol. 47, no. 10, pp. 1831–1837, 2000.

[39] D. Vasileska and S. M. Goodnick, "Computational electronics," *Synth. Lect. Comput. Electromagn.*, 2006.

[40] W. J. Schaffer, G. H. Negley, K. G. Irvine, and J. W. Palmour, "Conductivity anisotropy in epitaxial 6H and 4H SiC," in *Materials Research Society Symposium - Proceedings*, 1994, pp. 595–600.

[41] I. A. Khan and J. A. Cooper, "Measurement of High-Field Electron Transport in Silicon Carbide," *IEEE Trans. Electron Devices*, vol. 47, no. 2, pp. 269–273, 2000.

[42] D. M. Caughey and R. E. Thomas, "Carrier mobilities in silicon empirically related to doping and field," *Proc. IEEE*, vol. 55, no. 12, pp. 2192–2193, 1967.

[43] M. Lades, "Modeling and Simulation of Wide Bandgap Semiconductor Devices : 4H / 6H-SiC," T. U. Munich, 2000.

[44] J. B. Krieger and G. J. Iafrate, "Time evolution of Bloch electrons in a homogeneous electric field," *Phys. Rev. B*, vol. 33, no. 8, pp. 5494–5500, Apr. 1986.

[45] H. E. Nilsson, A. Martinez, and U. Sannemo, "Numerical study of Bloch electron dynamics in wide band-gap semiconductors," *Appl. Surf. Sci.*, vol. 184, no. 1–4, pp. 199–203, 2001.

[46] R. Hathwar, M. Saraniti, and S. M. Goodnick, "Modeling of multi-band drift in nanowires using a full band Monte Carlo simulation," *J. Appl. Phys.*, vol. 120, no. 4, p. 44307, 2016.

[47] A. Savitzky and M. J. E. Golay, "Smoothing and Differentiation of Data by Simplified Least Squares Procedures," *Anal. Chem.*, vol. 36, no. 8, pp. 1627–1639, 1964.

[48] A. K. Sharma, S. H. Zaidi, S. Lucero, S. R. J. Brueck, and N. E. Islam, "Mobility and transverse electric field effects in channel conduction of wrap-around-gate nanowire MOSFETs," *IEE Proc. Circuits, Devices Syst.*, vol. 151, no. 5, pp. 422–430, 2004.

[49] M. Lades, W. Kaindl, N. Kaminski, E. Niemann, and G. Wachutka, “Dynamics of incomplete ionized dopants and their impact on 4H/6H-SiC devices,” *IEEE Trans. Electron Devices*, vol. 46, no. 3, pp. 598–604, 1999.

PUBLICATION

Conference Papers

1. Chi-Yin Cheng, Dragica Vasileska, “Transport Analysis of 4H-SiC Power Devices Using Full-Band Ensemble Monte Carlo Method,” MRS, Spring 2019.

2. Chi-Yin Cheng, Dragica Vasileska, “Transport Modeling of 4H-SiC for Power Device Applications Using Full-Band Ensemble Monte Carlo Method,” International Workshop on Computational Nanotechnology, 2019.

Journal Papers

1. Chi-Yin Cheng, Dragica Vasileska, " Static and Transient Simulation of 4H-SiC VDMOS Using Full-Band Monte Carlo Simulation that Includes Real-Space Treatment of the Coulomb Interactions ", IEEE Transactions on Electron Devices, April 2020. (Submitted)

2. Chi-Yin Cheng, Dragica Vasileska, "Electron transport analysis of 4H-SiC with full-band Monte Carlo simulation including real-space Coulomb interactions", Journal of Applied Physics, vol. 127, pp. 155702, Apr. 2020.

3. Houqiang Fu, Kai Fu, Shanthan R Alugubelli, Chi-Yin Cheng, Xuanqi Huang, Hong Chen, Tsung-Han Yang, Chen Yang, Jingan Zhou, Jossue Montes, Xuguang Deng, Xin Qi, Stephen M Goodnick, Fernando A Ponce, Yuji Zhao, "High Voltage Vertical GaN p-n Diodes With Hydrogen-Plasma Based Guard Rings," IEEE Electron Device Letters, vol. 41, no. 1, pp. 127-130, Jan. 2020.

4. Kai Fu, Houqiang Fu, Xuanqi Huang, Tsung-Han Yang, Chi-Yin Cheng, Prudhvi Ram Peri, Hong Chen, Jossue Montes, Chen Yang, Jingan Zhou, Xuguang Deng, Xin Qi, David J Smith, Stephen M Goodnick, Yuji Zhao, "Reverse Leakage Analysis for As-Grown and Regrown Vertical GaN-on-GaN Schottky Barrier Diodes," IEEE Journal of the Electron Devices Society, vol. 8, pp. 74-83, 2020.